Exploring future multi-messenger galactic astronomy

Korol, V.

Exploring future multi-messenger Galactic Astronomy

Valeriya Korol

Exploring future multi-messenger Galactic Astronomy

Proefschrift

ter verkrijging van
de graad van Doctor aan de Universiteit Leiden,
op gezag van Rector Magnificus prof. mr. C.J.J.M. Stolker,
volgens besluit van het College voor Promoties
te verdedigen op woensdag 19 juni 2019 klokke 13.45 uur

door

Valeriya Korol

geboren te Sumy, Oekraïne
in 1988

Promotores:
Dr. E.M. Rossi
Prof. dr. P.J. Groot (Radboud University)
Prof. dr. A.G.G.M. Tielens

Overige leden:
Prof. dr. N. Cornish (Montana State University)
Prof. dr. S. Larson (Northwestern University)
Dr. S.E. de Mink (University of Amsterdam)
Dr. M. Kilic (University of Oklahoma)
Prof. dr. K.H. Kuijken
Prof. dr. H.J.A. Röttgering

Cover design by Luke T. Maud, Alla and Valeriya Korol
Original image adapted from numerical simulations of S. Ossokine, A. Buonanno (MPI for Gravitational Physics) and W. Benger (Airborne Hydro Mapping GmbH)
Translation into Ukrainian by Artur Korol

ISBN 978-94-6380-389-2

Printed by ProefschriftMaken www.proefschriftmaken.nl
An electronic version of this thesis can be found at openaccess.leidenuniv.nl

To my grandpas

Gigantic multiplied by colossal multiplied by staggeringly huge
is the sort of potential we reach when exploring
the possibilities of multi-messenger studies!
(adopted from D. Adams)

Contents

Chapter 1

Introduction

The Universe is comprised of structures called galaxies such as our Milky Way. Stars are the fundamental building blocks of galaxies. Thus, by studying how stars are distributed and how their properties change across a galaxy and over time, we can understand how galaxies form and evolve. Our understanding of stellar evolution and of the stellar initial mass function imply that over 98% of all stars in the Milky Way will (eventually) end their lives as white dwarfs (WDs). WDs are the evolutionary end stage of low- and intermediate-mass stars after they have consumed all of their fuel, shed their outer layers and the remnant cores just glow from the residual heat. Consequently, the oldest WDs are also the coldest and the faintest ones. The quest to find the faintest WD in our Galaxy resulted in the first estimates of the age of the Milky Way (and in general of the Universe) (e.g., Hansen et al., 2002; Oswalt et al., 1996). By using the WD age-luminosity relationship one can construct the WD luminosity function, which is one of the best tools to reconstruct the star formation history (SFH) and to date different Galactic populations (e.g., Kilic et al., 2017; Tremblay et al., 2014). Furthermore, WDs are thought to be at the root of a phenomenon called "supernova type Ia" (SNIa) explosions. These very luminous events have been used to trace the expansion of the Universe, leading to the Nobel Prize discovery that such an expansion is accelerating and thus contains a driving force, called dark energy (Perlmutter et al., 1999; Riess et al., 1998). Therefore, it is widely recognised that the study of WD stars is important for understanding the evolution of galaxies and the Universe. This thesis proposes to use a different property of these extremely common compact objects to study our Galaxy and its neighbourhood; their gravitational wave (GW) emission.

Stars often form binary systems, in which they are gravitationally bound to each other and orbit about their common centre of mass. It is believed that about 50% of stars reside in binary systems, although the precise percentage depends on the type of the star. Between 5% - 10% of all WDs are in double WD (DWD) binaries (Maoz et al., 2018; Toonen et al., 2017). Given this and the fact that the initial stellar mass function (IMF) prefers the formation of low-mass stars, numerical simulation predict over 10^8 DWD systems currently present in our Galaxy (Maxted & Marsh, 1999; Nelemans et al., 2001; Ruiter et al., 2010). In particular, the most compact DWD binaries emit strong GW radiation in the frequency band of the future European Space Agency (ESA) mission, LISA (Laser Interferometer Space Antenna, Amaro-Seoane et al., 2017, see Fig. 1.1). Tens of thousands are expected to be discovered by LISA, making DWDs

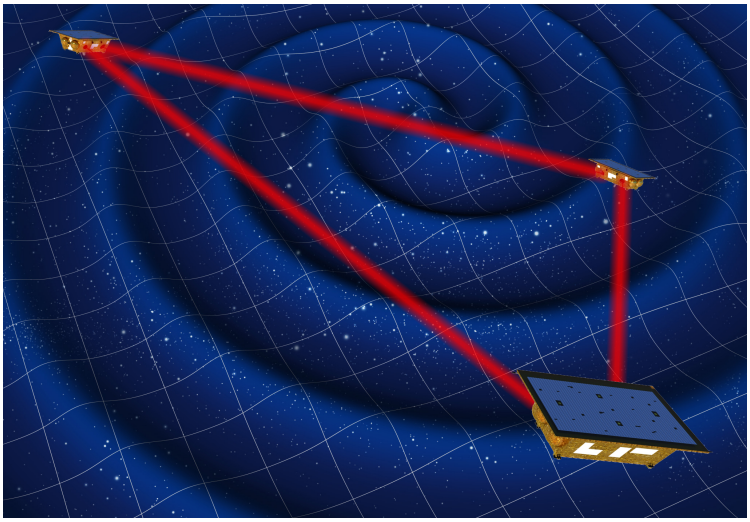

Figure 1.1: Artist impression of the LISA mission, an ESA mission designed to measure gravitational radiation over a broad band at low GW frequencies, from about 0.1 mHz to 0.1 Hz. Immage credits: ESA

the most numerous GW source in our Galaxy (Nelemans et al., 2001; Nissanke et al., 2012; Ruiter et al., 2010). GWs provide very different information compared to what can be deduced from electromagnetic (EM) observations, which for DWD are mainly limited to optical wavelengths. LISA's capability to determine distances (difficult to derive from optical observations for such faint sources) for large number of Galactic GW sources as well as the fact that GWs are unaffected by stellar dust will open a new window for Galactic astronomy enabling a muti-messenger (EM+GW) study of the Galaxy. Numerous resolved GW signals (but also unresolved populations) will provide a tomographic picture of the Galaxy. The full picture emerges jointly with optical kinematic properties of DWD systems complementing the positional information from GWs, to unveil the shape and total dynamical mass of the Galaxy.

1.1 How to form a double white dwarf binary

The formation of a typical DWD begins with intermediate-mass ($2-5\,\mathrm{M}_{\odot}$) binary components with a primary mass m_1, a secondary mass m_2 (with $m_2 < m_1$), a semi-major axis a and an eccentricity e. The majority of binaries are born at wide separations (corresponding to $P_{\mathrm{orb}} > 100\,\mathrm{yr}$, Abt, 1983). These binaries will never undergo an interacting phase and the system will evolve as though it is made up of two single stars, each completely uninfluenced by its companion. To form a close binary, the progenitor system typically has to undergo a few phases of mass transfer (see Fig. 1.1). Mass transfer can occur when one of the two binary components grows to a size such that its envelope is no longer gravitationally bound to the star (i.e., the star fills its Roche lobe[1]). In such a case it is possible for the companion star to accrete some or all of the envelope from the primary. If the mass transfer phase proceeds in a stable

[1]Roche lobe is the surface defining the region of gravitational influence of a star in a binary system.

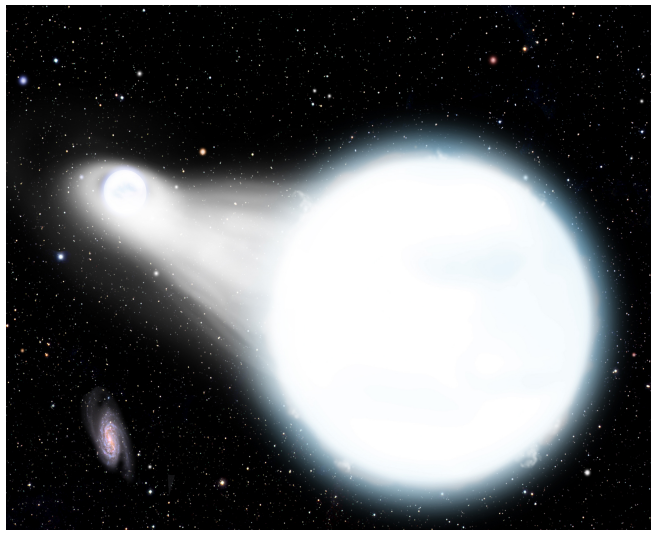

Figure 1.2: Artist impression of the mass transfer process, one of the fundamental processes in the binary evolution. Image credits: D. Aguilar (CfA).

manner, the donor star can readjust its structure to retain hydrostatic and thermal equilibrium, and the envelope will stay approximately within the Roche lobe. The orbit of the system is affected by the re-arrangement (and possible loss) of mass and angular momentum, and in general widens. When mass transfer becomes unstable, the donor star will significantly overflow its Roche lobe upon mass loss. Subsequently the mass transfer rate increases even more leading to a runaway situation in which a common envelope (CE) develops around both stars. Figure 1.1 illustrates a situation of stable mass transfer.

To form a DWD the progenitor system needs to undergo at least two phases of mass transfer: the first occurs when the primary evolves off the main sequence and the second, when the same happens to the secondary. It is believed that at least one of the two mass transfer episodes is necessarily unstable which leads to CE formation (Paczynski, 1976; Webbink, 1984). The reason for this requirement comes from the fact that the CE is thought to be the most efficient way to tighten a binary system. It is often used to explain a large number and wide diversity of compact binary stars that includes, besides DWDs, cataclysmic variables, Type Ia supernovae progentors, X-ray binaries and binary black holes recently detected by the LIGO and Virgo collaboration (Abbott et al., 2016, 2017).

The CE is a short-lived phase of binary evolution during which both stars orbit inside a single, shared envelope. This may occur when one of the stars significantly expands to a size much larger than the binary orbital separation, basically engulfing the companion star. The companion star spirals inward through the envelope, losing orbital energy and angular momentum due to dynamical friction, and heats the envelope. This phase continues until either the two stars eventually coalesce or the envelope is ejected from the system leaving behind the core of the primary. The end result for intermediate- and low-mass stars after the ejection of the envelope is either a hot sub-dwarf star, which then rapidly cools down to become a WD, or a helium star, which will later evolve into a WD, if the primary was on the red giant branch

with a mass $> 2\,\mathrm{M}_\odot$ This general idea of CE evolution is well accepted, however the details are still not understood (e.g., Ivanova et al., 2013). Simulations of CE evolution are extremely challenging for both computational and analytical treatments as, from beginning to end, the problem involves a complex mix of physical processes operating over a huge range of scales. The earlier treatments of the CE problem are based on very general considerations of energy and angular momentum conservation, and are still widely employed in binary modelling. The two most common ones are the α- and γ- formalisms.

In the α-formalism, the energy budget for the binary is fixed at the onset of mass transfer. The post-CE system is therefore constrained to have an orbital energy which is negative enough to ensure envelope ejection. An efficiency parameter, α, was introduced to characterise the fraction of dissipated orbital energy actually used to eject the envelope (Livio & Soker, 1988). So that the energy budget can be written as

$$E_{\mathrm{bind,i}} = \alpha(E_{\mathrm{orb,f}} - E_{\mathrm{orb,i}}), \tag{1.1}$$

where $E_{\mathrm{bind,i}} = -Gm_1m_{\mathrm{env},1}/\lambda R_1$ is the initial binding energy of the envelope with $m_{\mathrm{env},1}$ being the mass of the primary's envelope and λ being a parameter that depends on the primary's structure, $E_{\mathrm{orb,f}}$ and $E_{\mathrm{orb,i}}$ are respectively the final and the initial total binary orbital energies.

The alternative γ-prescription was originally proposed to explain the formation of some known DWD binaries by Nelemans et al. (2000). In the analysed sample, the older WD of the two in a binary system has a smaller mass instead of being more massive as one would expect from the standard stellar evolution scenario. This can happen if the orbital separation at the onset of the second mass transfer stage is wider than at the onset of the first one. The α-formalism would not naturally describe a CE phase which widens the binary orbit, because this would require an additional energy source present during CE evolution (i.e. $\alpha > 1$). The proposed governing equation to explain this is angular momentum conservation:

$$\frac{J_\mathrm{i} - J_\mathrm{f}}{J_\mathrm{i}} = \gamma\frac{m_{\mathrm{ejec}}}{m_1 + m_2}, \tag{1.2}$$

where J_i and J_f are the initial and the final binary orbital angular momenta, and m_{ejec} is the mass of the ejected envelope and γ is the efficiency parameter which can be inferred from observations (Nelemans et al., 2000). All of the observed DWD systems can be explained by very similar values of γ, meaning that only one representative value of γ is required when modelling DWD evolution (Nelemans & Tout, 2005).

Figure 1.3 illustrates an example of a typical evolution path, leading to a close DWD binary (Toonen et al., 2012). In this example, two zero-age main-sequence stars of $6\,\mathrm{M}_\odot$ and $4\,\mathrm{M}_\odot$ are initially on a 125 day orbit. The first CE occurs when the primary ascends the red giant branch and fills its Roche lobe. During this phase the primary loses its hydrogen envelope and becomes a helium star. When all the helium is exhausted, the primary becomes a WD of about $1\,\mathrm{M}_\odot$. Continuing with the evolution of the system, the secondary star later evolves off the main sequence, and a second CE occurs. In this CE phase, the orbit shrinks further, decreasing from 30 days to 4 hours. The secondary evolves into a helium star without a hydrogen envelope until it also turns into a WD, thus creating a DWD binary. Once the CE evolution is over, the only process driving subsequent DWD evolution is the loss of energy through GW radiation that slowly brings the stars closer together (see Section 1.4).

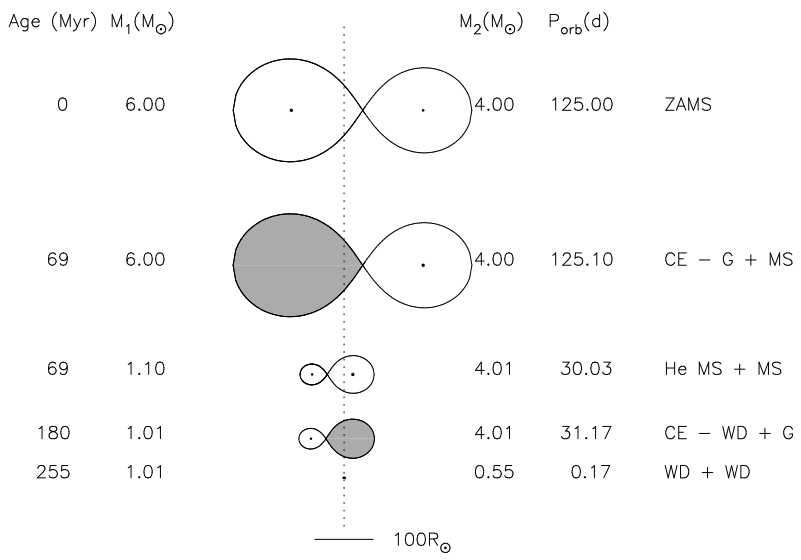

Figure 1.3: A typical evolution path to form a compact DWD. In this case the first phase of mass transfer is dynamically unstable which results in a CE. ZAMS stands for zero age main sequence. G is a giant star, MS a main-sequence star, He MS a helium MS and WD a white dwarf. The figure is adapted from Toonen et al. (2012).

1.2 How to assemble a mock population of double white dwarf binaries

Binary population synthesis (BPS) is a technique used to model the evolution of an entire population of binaries under a common set of assumptions (e.g., de Kool, 1990; Dewey & Cordes, 1987; Kolb et al., 2000; Lipunov & Postnov, 1987; Politano, 1988; Portegies Zwart & Spreeuw, 1996). This method offers a fast way of computing the overall properties of a population and allows comparisons with observed samples. Unlike in detailed stellar evolution codes (such as MESA, Paxton et al., 2011), BPS codes do not resolve the stellar structure. Although the additional information of a computationally resolved stellar structure is a significant advantage when modelling binary interactions, it is computationally too expensive for a large number of systems. The basic goal in population synthesis calculations is to follow the evolution of an ensemble of primordial binaries through all possible phases until the formation of the systems of interest (for example, DWDs in this thesis) by adopting adequate analytic prescriptions. Typically evolutionary phases include: wind mass loss, stable or unstable mass and angular momentum transfer, formation of compact objects, circularisation, angular momentum loss through gravitational radiation and magnetic braking.

This thesis makes extensive use of the BPS code SeBa, originally developed by Portegies Zwart & Verbunt (1996), calibrated for DWD by Nelemans et al. (2001) and more recently updated and tested against observations by Toonen et al. (2012, 2017). The logic behind SeBa is not to define the evolution of the binary a priori, but rather to determine it at time intervals depending on the parameters of the system. It has

been used to study a large range of stellar populations: high mass binaries (Portegies Zwart & Verbunt, 1996), double neutron stars (Portegies Zwart & Yungelson, 1998), gravitational wave sources (Nelemans et al., 2001; Nissanke et al., 2012; Portegies Zwart & Spreeuw, 1996), double white dwarfs (Nelemans et al., 2001), AM CVn systems (Nelemans et al., 2001, 2004), supernovae Type Ia progenitors (Toonen et al., 2012) and ultra-compact X-ray binaries (van Haaften et al., 2013). SeBa has also been used to simulate the evolution of dense stellar systems as part of the software package Starlab (Portegies Zwart et al., 2001, 2004) and recently has been implemented in AMUSE[2] (Astrophysics Multipurpose Software Environment, Portegies Zwart et al., 2009). For the case of DWDs, SeBa predictions were compared with other BPS codes such as binary_c (Hurley et al., 2000, 2002) and StarTrack (Belczynski et al., 2008) by Toonen et al. (2014). The considered codes identify similar evolutionary channels leading to DWD formation and have a rough agreement on WD masses, however differences in the mass transfer phase result in a different distribution of binary orbital separations.

Starting from initial distributions of binary properties such as the distribution of binary orbital parameters and component masses motivated by observations, SeBa is left to run until both stars in the binary turn into WDs. Although the γ-CE prescription was designed and calibrated for DWD systems, to facilitate the comparison with other works, this thesis employs both α- and γ-prescriptions described in Sect. 1.1. The main differences in the results are the total number of DWD binaries and their mass ratio distribution. More specifically, using the γ-CE recipe, one obtains twice as many binaries that cover a wider range of mass ratios compared to the α recipe. In contrast, the population obtained using the α-prescription typically peaks at a mass ratio of 0.5 (see Toonen et al., 2012). This is due to the fact that, in the α-prescription, the orbit always shrinks. When using the γ-prescription the CE outcome depends on the binary mass ratio (see, e.g., Equation (A.16) Nelemans et al., 2001): for a roughly equal mass binary the orbit does not change much, however, for a binary with very different mass components the orbit shrinks significantly.

The next step consists of assigning the spatial and age distributions for the synthetic binaries, using a representative density profile and a star formation history (SFH) for the Galaxy. For example, in Chapters 3 and 5 an exponential disc and spherical bulge density distributions are used, normalised according to the SFH from Boissier & Prantzos (1999) used to model the DWD population in the Milky Way. Figure 1.4 illustrates the resulting distribution in Galactic coordinates. An alternative way of assigning a realistic spatial distribution for binaries is by using a cosmological simulation. In this way one needs to relate the properties such as mass, metallicity and age of each simulated particle with the outcome of a BPS code (e.g., Lamberts et al., 2018). Finally, now knowing the spatial distribution of DWDs in the mock Galaxy one can compute their observed properties.

[2]This is a component library with a homogeneous interface structure, and can be downloaded for free at amusecode.org

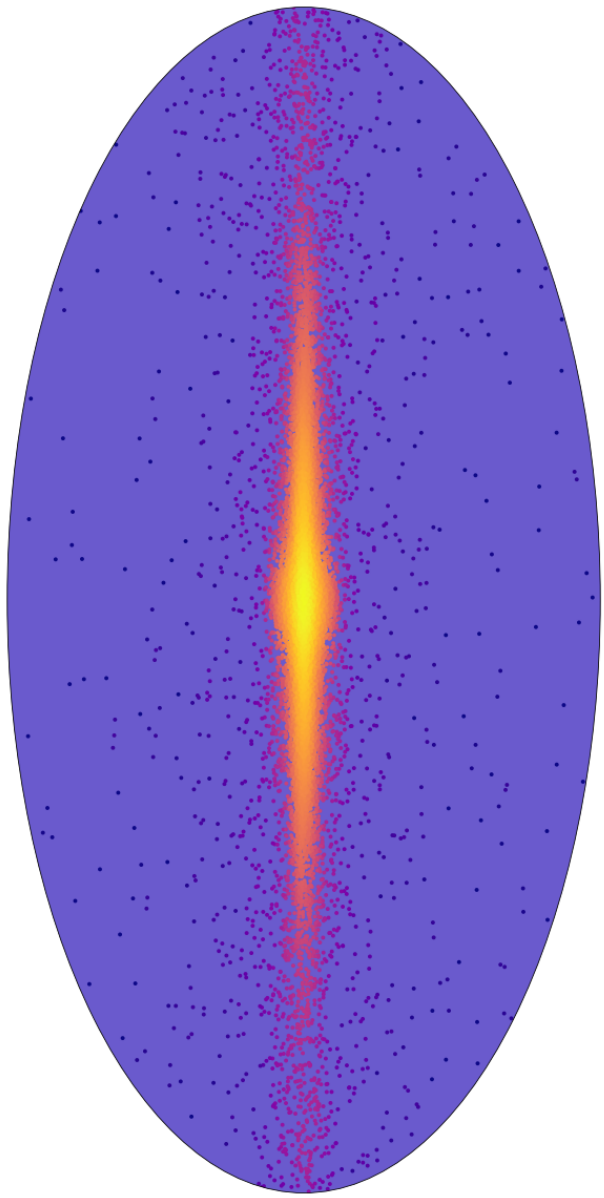

Figure 1.4: Distribution of DWDs that can be detected by LISA in Galactic coordinates from Korol et al. (2018). The colour represents the density of the potential LISA detections: yellow being the most dense.

1.3 How to detect a double white dwarf binary in electromagnetic radiation

There are several astronomical techniques that one can use to spot a binary amongst single stars: photometry (by monitoring changes in brightness caused for example by an eclipse); spectroscopy (by searching for periodic changes in spectral lines); and astrometry (by measuring a deviation in a star's position caused by an unseen companion). In general, the first two are efficient techniques when searching for binaries with orbital periods less than a few days. However, finding close DWDs is extremely challenging. Firstly, because WD are intrinsically faint stars, and secondly, because DWD spectra are virtually identical to those of single WDs. In addition, because WDs are compact, their eclipse times are very short.

The current census of DWDs amounts to around a 100 systems (considering those with orbital periods $< 100\,\mathrm{h}$). The first DWD was observed in the late 1980s by Saffer et al. (1988) and a handful more were discovered in the 1990s (e.g., Marsh, 1995; Maxted & Marsh, 1999). The first substantial progress came with targeted spectroscopic and variability surveys such as the SPY (ESO SN Ia Progenitor, Napiwotzki et al., 2003) and the ELM (Extremely Low Mass WDs) surveys (Brown et al., 2010). The SPY project is a spectroscopic study of about > 1000 apparently single WDs to search for radial velocity variations indicative of binarity. A substantial fraction (16%) WDs of the sample indeed showed evidence for a close WD companion, among which also a promising SNIa progenitor was found. The ELM is a very fruitful survey and has resulted in the detection of several tens of short period binaries (see the period distribution in Fig. 3.6). These extreme low-mass WDs ($M < 0.3\,\mathrm{M}_{\odot}$) were discovered as a part of a colour selected sample of hyper velocity candidates from the Sloan Digital Sky Survey (SDSS) by Brown et al. (2010). Although the applied colour selection were originally designed to target late-B type stars, it turned out to be optimal also for identifying low-mass WDs. Given that the Universe is simply not old enough to produce such low-mass WDs by single star evolution, to explain the ELM's findings, binary companions are required. One of the ELM's WDs, SDSS J065133.34+284423.4 (hereafter J0651), is a 12 min orbital period binary (Brown et al., 2011). This system is a GW source stronger than the Hulse-Taylor Nobel prize binary pulsar and will merge in ~ 1 million years (Hulse & Taylor, 1975). The rapid change of the orbital period due to GW emission in systems like J0651 provide indirect test of general relativity. Figure 1.5 shows the secular change in the orbital period of J0651 by constructing an (O-C) diagram, where the observed mid-eclipse times (O) and the expected mid-eclipse times computed from the assumption of a fixed orbital period (C) for future epochs are compared (Hermes et al., 2012).

The number of observed DWDs will substantially increase with the upcoming future all-sky and wide optical surveys like *Gaia* (Gaia Collaboration et al., 2016), the Large Synoptic Survey Telescope (LSST; LSST Science Collaboration et al., 2009) and fast transient surveys like the Zwicky Transient Facility (ZTF; Bellm et al., 2019) and BlackGEM (Bloemen et al., 2015). The newly discovered DWD, ZTF J153932.16+502738.8, with the orbital period of only 6.91 minutes is an excellent example of the capabilities of the aforementioned surveys (Burdge et al. 2019, accepted for publication in Nature Astronomy). Future prospects for the detection of close WD pairs at optical wavelengths are extensively investigated in Chapter 3.

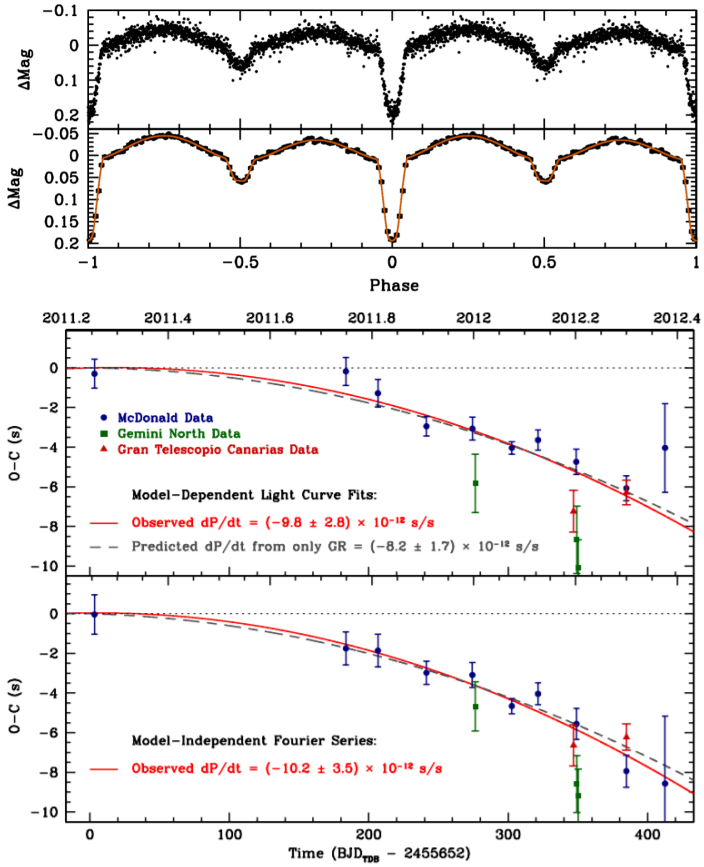

Figure 1.5: Top panels show high-speed photometry of J0651 folded at the orbital period. Bottom panels show (O-C) diagrams of the orbital evolution in J0651. The top panel shows the change in mid-eclipse times as determined by light curve modelling, and the best-fit parabola yields an estimate for the observed rate of orbital period change. The bottom panel shows the results from a model-independent, linear least-squares fit using the orbital period and higher harmonics. The dotted line at (O-C) = 0 shows the line of zero orbital decay, while the grey dashed line shows the predicted orbital decay expected solely from gravitational wave radiation. Both figures are adopted from Hermes et al. (2012).

1.4 How to detect a double white dwarf binary in gravitational waves

A paramount breakthrough in astronomy occurred recently with the detection of GW generated by merging binary BH, and binary NS systems (Abbott et al., 2016, 2017). With these revolutionary detections a new window in observations of the Universe was opened, providing a unique way to study merging ultra-compact binaries composed of compact stellar remnants.

GWs are produced by the motion of large masses at relativistic speeds. More precisely, GWs are ripples in the Riemannian curvature of space-time, the fundamental dynamical entity in General Relativity. They propagate almost without alteration and have the potential to carry information throughout the Universe, in principle, all the way from the Big Bang. The practically unhindered propagation is due to the weakness of the gravitational interaction as compared to other forces, and due to the fact, that GWs cannot be screened by any type of matter field. Indeed, the charge associated with the gravitational interaction is the mass, and therefore is always positive.

The first analytic computation of GWs is the Einstein's quadrupole formula, valid at the dominant zero order in a post Newtonian (PN) expansion (Einstein, 1916, 1918). Originally derived for matter sources with negligible self gravity (hence the source's oscillations producing GWs have a non gravitational origin), the formula was later shown to be still valid for weakly self-gravitating sources, such as a Newtonian binary system (Landau & Lifshitz, 1971). The GW amplitude is characterised by two tensorial polarisation modes, traditionally denoted h_+ and $h_\times$, that are transverse to the direction of propagation $\mathbf{n} = (n^i)$ with $i = 1, 2, 3$ and $\mathbf{n}^2 = 1$, pointing from the GW source towards a faraway detector. Thus, a GW detector is sensitive to a certain linear combination of the two polarisations:

$$h = h_+ F_+ + h_\times F_\times, \tag{1.3}$$

where F_+ and $F_\times$ describe the sensitivity of the detector to the polarisation and depend upon the relative orientation of the source and the detector. The polarisations are defined as the projection of the waveform along two polarisation vectors $\mathbf{p}$ and $\mathbf{q}$ in the plane orthogonal to $\mathbf{n}$, and forming with it an orthonormal right-handed triad $(\hat{\mathbf{n}}, \hat{\mathbf{p}}, \hat{\mathbf{q}})$. The quadrupole formula gives the polarisations at a large distance d from the source (and at retarded time $t - d/c$) as

$$\begin{pmatrix} h_+ \\ h_\times \end{pmatrix} = \frac{2G}{c^4 d} \begin{pmatrix} \frac{p^i p^j - q^i q^j}{2} \\ \frac{p^i q^j + p^j q^i}{2} \end{pmatrix} \left\{ \frac{d^2 Q_{ij}}{dt^2}(t - d/c) + \mathcal{O}(\epsilon_{\rm PN}) \right\}, \tag{1.4}$$

where Q_{ij} is the mass quadrupole moment

$$Q_{ij} = \int \rho \left(x^i x^j - \frac{1}{3}\mathbf{x}^2 \right) d^3\mathbf{x}. \tag{1.5}$$

The rate at which energy is carried away by GWs is given by

$$\frac{dE_{\rm GW}}{dt} = -\frac{G}{5c^5} \left\{ \frac{d^3 Q_{ij}}{dt^3} \frac{d^3 Q_{ij}}{dt^3} + \mathcal{O}(\epsilon_{\rm PN}^2) \right\}. \tag{1.6}$$

Similarly, the angular momentum loss can be found as

$$\frac{dJ_{\mathrm{GW}i}}{dt} = -\frac{G}{5c^5}\epsilon_{ijk}\left\{\frac{d^2Q_{jl}}{dt^2}\frac{d^3Q_{kl}}{dt^3} + \mathcal{O}(\epsilon^2_{\mathrm{PN}})\right\} \tag{1.7}$$

Equations (1.6) and (1.7) govern the evolution of the binary orbital parameters under GW emission. For a circular binary composed of two point masses m_1 and m_2 orbiting around their common barycentre separated by a the quadrupole moment is given by

$$Q_{ij}(t) = \frac{\mu a^2}{2} I_{ij}, \tag{1.8}$$

where $\mu = m_1 m_2/(m_1 + m_2)$ is the reduced mass and non-null components of I_{ij} are $I_{xx} = \cos(2\omega t) + 1/3, I_{yy} = 1/3 - \cos(2\omega t), I_{xy} = I_{yx} + \sin(2\omega t)$ and $I_{zz} = -2/3$. By plugin equation (1.8) into equation (1.4), one finds that for a binary source the GW polarisations become

$$\begin{pmatrix} h_+ \\ h_\times \end{pmatrix} = \frac{2G^2\mu M}{c^4 d\, a}\begin{pmatrix} (1+\cos^2 i)\ \cos(2\phi) \\ 2\cos i\ \ \sin(2\phi) \end{pmatrix}, \tag{1.9}$$

where $M = m_1 + m_2$ is the total mass of the binary, i is the inclination angle of the binary's orbital plane with respect to the plane of the sky. In the quadrupole formalism the phase of the signal is $\phi_{\mathrm{GW}} = 2\phi$ with $\phi = \int \omega dt$ the orbital phase and ω the angular frequency; while the signal frequency is $f_{\mathrm{GW}} = \omega/\pi = 2f$.

The energy radiated in GWs can be found by combining equations (1.6) and (1.8) as

$$\frac{dE_{\mathrm{GW}}}{dt} = \frac{32}{5}\frac{G}{c^5}\mu^2 a^4 \omega^6. \tag{1.10}$$

This is the energy loss that drains the binary orbital energy $E_{\mathrm{orb}} = -2GM\mu/2a$. Thus, $dE_{\mathrm{orb}}/dt = GM\mu\dot{a}/2a^2 = -dE_{\mathrm{GW}}/dt$. Using Kepler's third law $a^3 = GM/\omega^2$ and its derivative $\dot{a} = -2a\dot{\omega}/3\omega$ one can eliminate a in favour of ω and write

$$\dot{\omega}^3 = \left(\frac{96}{5}\right)^3 \frac{\omega^{11}}{c^{15}} G^5 \mu^3 M^2 = \left(\frac{96}{5}\right)^3 \frac{\omega^{11}}{c^{15}} \left(G\mathcal{M}\right)^5, \tag{1.11}$$

having defined the chirp mass $\mathcal{M} = \left(\mu^3 M^2\right)^{1/5}$, which determines how fast the binary sweeps, or chirps, through a frequency band. Equation (1.11) describes the evolution of the system as an inspiral: orbital frequency goes up (chips), while by Kepler's Law the orbital separation shrinks. One can express equation (1.11) in therms of GW frequency as

$$\dot{f}_{\mathrm{GW}} = \frac{96}{5}\pi^{8/3}\left(\frac{G\mathcal{M}}{c^3}\right)^{5/3} f_{\mathrm{GW}}^{11/3}. \tag{1.12}$$

Note, that when $\dot{f}_{\mathrm{GW}}$ is measurable, the value of the chirp mass can be determined directly from GW observational data, using the frequency and frequency derivative of GWs. By integrating equation (1.12) from a time t to the time of coalescence τ and solving for τ, one can estimate how long it takes for a binary to merge due to GW emission:

$$\tau = \frac{5}{256}\frac{c^5 a^4}{G^3 M^2 \mu}. \tag{1.13}$$

For example, the 12 min DWD system J0651 (Brown et al., 2011) with binary component masses of $0.55\,\mathrm{M}_\odot$ and $0.25\,\mathrm{M}_\odot$ will coalesce in

$$\tau \simeq 1\,\mathrm{Myr}\,\left(\frac{P}{12\,\mathrm{min}}\right)^{8/3}\left(\frac{\mathcal{M}}{0.3\,\mathrm{M}_\odot}\right)^{-5/3}. \tag{1.14}$$

As the frequency of the binary changes, the amplitude of GW polarisations defined in equation (1.9) changes as well. Note, that since G is small and c is large (unless $\mathcal{M}$ is large, the system is changing fast, and d is small) typically h is minuscule. For J0651 at the distance of $\sim 1\,\mathrm{kpc}$

$$h \simeq 1.62\times10^{-22}\left(\frac{P}{12\,\mathrm{min}}\right)^{-2/3}\left(\frac{\mathcal{M}}{0.3\,\mathrm{M}_\odot}\right)^{5/3}\left(\frac{d}{1\mathrm{kpc}}\right)^{-1}. \tag{1.15}$$

Note also, that the GW amplitudes (equation 1.9) fall with increasing distance as $1/d$, while for EM observations the strength of the observed signal falls as $1/d^2$. This is an important difference between GW and EM astronomy that makes it possible to detect GW sources very early in the evolution of the Universe. By measuring f_{GW}, rate of change of frequency $\dot{f}_{\mathrm{GW}}$ and amplitude of the signal h, one can use equations (1.12) and (1.9) to eliminate all the unknowns and solve for the distance d to the GW source (e.g., Schutz, 1986). Therefore, GW sources constitute an analogue of the standard candles of EM-based astronomy (like Cepheid variables and SNIa), and can rightly be called "standard sirens". Thus, it is possible to measure the Hubble cosmological parameter H_0 with GWs if also the redshift to the source is known from EM measurements (e.g., Abbott et al., 2017; Nissanke et al., 2013; Tamanini et al., 2016). Note also, that GWs are stretched by the expansion of the Universe as they travel across it. This increases the wavelength and decreases the frequency of the waves observed at the detector compared to their values when emitted. The same effect accounts for the redshifting of photons from distant objects. The impact of this on GW measurement corresponds to a scaling of the masses as measured at the detector; equation (1.12) shows that the source frame masses are smaller by $(1+z)$ relative to the detector frame, where z is the redshift. For Galactic binaries considered here, this effect is negligible.

Given the long timescales on which DWDs evolve (equation 1.13) compared to the observation time T_{obs} (a few years for the LISA mission), they can be, initally, treated as quasi-monochromatic GW sources. In this case the signal-to-noise can be estimated as (see Maggiore, 2008, and Appendix A for a detailed derivation):

$$\left(\frac{S}{N}\right)^2 = |F_+h_+ + F_\times h_\times e^{i\alpha}|^2\frac{T_{\mathrm{obs}}}{S_{\mathrm{n}}(f_{\mathrm{GW}})}, \tag{1.16}$$

where $e^{i\alpha}$ is the relative phase between two polarisations and S_n is the instrument noise spectral density of the detector expressed in Hz^{-1} (green solid line in Figure 1.7).

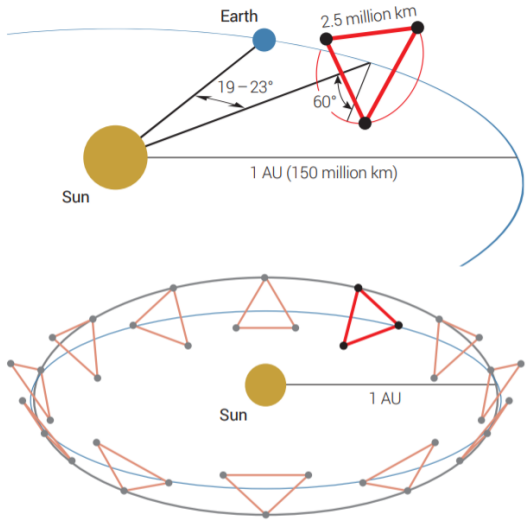

Figure 1.6: LISA's orbit. The Figure is adopted from Amaro-Seoane et al. (2017).

1.4.1 Laser Interferometer Space Antenna

The LISA mission is a large ESA mission and one of the most ambitious scientific observatory missions ever contemplated. LISA is designed to detect GW sources in the low-frequency GW band (0.1 mHz - 1 Hz) by measuring pico-meter scale changes in the distances between test particles. Practically, such accuracy can be realised by constructing a giant laser interferometer in space. The first ideas for detecting GWs in space date back to the 1980s. Since then various mission concepts have been formulated and studied, including the original LISA mission proposed in 1993 (Danzmann et al. 1993). Over the last few decades the likelihood of making LISA a reality was uncertain mostly due to its high costs and the necessity of developing new technologies. Finally, after a number of modifications and a reduced budget it was adopted by ESA in 2017 with a potential launch date in the early 2030s (Amaro-Seoane et al., 2017).

In principle, LISA can be thought of as a combination of Michelson interferometers, all of which measure changes in the proper distance between reference points: test masses that form the end mirrors of the interferometer arms. The experimental approach is however closer to that of spacecraft Doppler tracking, in which the observed quantity is the frequency change in the signal from a distant spacecraft realised with infrared laser light instead of radio waves (Estabrook & Wahlquist, 1975). The current accepted LISA design consists of three spacecrafts in an equilateral triangle configuration of 2.5 million km per side (Figure 1.6, Amaro-Seoane et al., 2017). Each pair of spacecrafts will be connected by two counter propagating laser "links" representing an actual laser interferometer. The laser light going out from one spacecraft to the other corners of the LISA triangle is not reflected back directly. This is because diffraction losses over such long distances would be too great to perform the measurement. Instead, the laser on the distant spacecraft is phase-locked to the incoming light and transmitted back at full intensity. When the transponded laser light arrives

back at the original spacecraft, it is superposed with a portion of the original laser beam, which serves as the local oscillator in a standard heterodyne detection scheme. The relative phase between the local reference laser and the incoming laser light gives information about the length of the interferometer arm. When passing, GWs alter the distance in different proportions for the individual arms depending on the wave's polarisation and orientation with respect to the detector. Measuring differences in phase between a pair of LISA's arms gives information about the relative changes in the two arms - the GW signal. The heart of each spacecraft is a vacuum enclosure containing a free flying polished platinum-gold cube - the "proof mass", that serves as an inertial reference for the local optical assembly. The spacecraft surrounding each pair of optical assemblies serves primarily to shield the proof masses from the adverse effects of solar radiation pressure fluctuations; the spacecraft positions do not enter directly into the measurements.

The mission concept has already been successfully tested by the LISA Pathfinder mission, the ESA precursor mission to LISA (Armano et al., 2016). LISA Pathfinder has demonstrated that the sophisticated space-time measurements that are the core metrology for a space GW observatory are indeed feasible, at and beyond the precision required by LISA (Armano et al., 2018). As a consequence of these results, exceeding the mission requirements, ESA has given a final green light to the development of LISA.

The centre of the LISA triangle will trace an orbit in the ecliptic plane, 1 AU from the Sun and 20° behind Earth, and the plane of the triangle is inclined at 60° to the ecliptic (see Figure 1.6). The natural free-fall orbits of the three spacecraft around the Sun maintain the triangular formation throughout the year, with the triangle appearing to rotate about its centre once per year. The proposed nominal mission duration is 4 years in science mode. However, the mission is designed with consumables and orbital stability to facilitate a total mission up to 10 years (Amaro-Seoane et al., 2017).

LISA's design allows the measurement of gravitational radiation over a broad frequency band in which the Universe is richly populated by strong GW emitters. LISA will be sensitive to a variety of astrophysical sources (see also Figure 1.7), such as merging massive black hole binaries ($\sim 10^4\,\mathrm{M}_\odot - 10^7\,\mathrm{M}_\odot$) out to $z \sim 15 - 20$ (e.g. Klein et al., 2016), extreme mass ratio inspirals (EMRI, e.g. Babak et al., 2017) and Galactic binaries (Breivik et al., 2018; Korol et al., 2017; Kremer et al., 2017; Lamberts et al., 2018). The Galactic binaries are comprised primarily of WDs, neutron stars and stellar-origin black holes in various combinations, among which DWDs are the most numerous. At frequencies below a few mHz Galactic binaries are so common in the Milky Way that only a small fraction will be resolved individually (blue points in Fig. 1.7). For these systems LISA will provide distances and detailed orbital and mass parameters for hundreds of the most compact binaries, a rich trove of information allowing the detailed mapping and reconstruction of the history of stars in our Galaxy. Therefore, LISA will be the only gravitational experiment capable of exploring the Milky Way. In addition, LISA measurements will be a source of information for studying the tidal and non-gravitational influences on orbits associated with the internal physics of the compact stellar remnants themselves. The signals from unresolved Galactic GW sources will sum up to form a foreground (grey shaded area in Fig. 1.7) for the LISA mission (e.g., Farmer & Phinney, 2003; Lipunov et al., 1995; Robson & Cornish, 2017). It is important to characterise this foreground signal to correctly

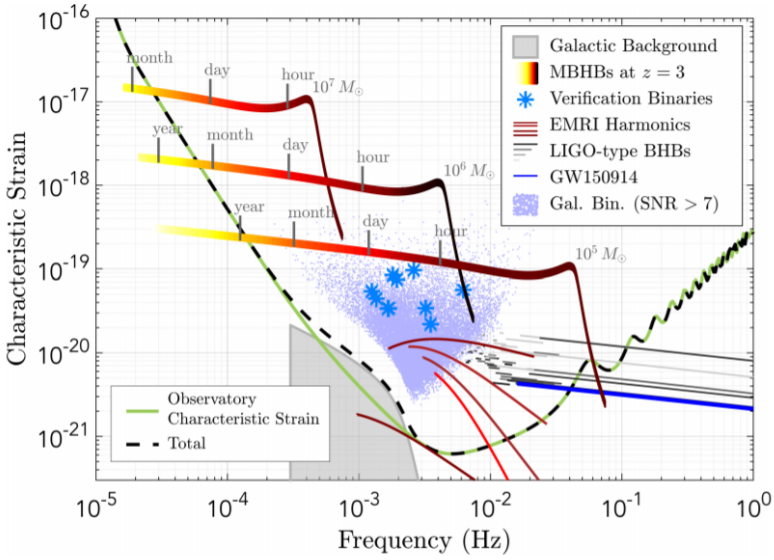

Figure 1.7: Characteristic strain amplitude of GW sources in the frequency band of LISA. LISA sensitivity curve is represented in green. The tracks of three equal mass black hole binaries at $z = 3$ with total intrinsic masses of $10^7, 10^6$ and $10^5\,\mathrm{M}_\odot$ are represented by coloured lines. The 5 simultaneously evolving harmonics of an EMRI at $z = 1.2$ are in red, and the tracks of a number of stellar origin black hole binaries are in black (GW150914 is in blue). Several thousand galactic binaries are represented by blue points, and those that are already known by blue stars. Millions of other binaries result in a "confusion signal", with a detected amplitude that is modulated by the motion of the constellation over the year; the average level is represented as the grey shaded area. The Figure is adopted from Amaro-Seoane et al. (2017).

identify and characterise extragalactic GW signals such as massive black hole mergers. However, the Galactic foreground also contains astrophysical information on the overall population of DWDs in the Milky Way and can be also used to derive the Milky Way's parameters such as the disc scale height (Benacquista & Holley-Bockelmann, 2006).

A major objective of LISA is to determine how and when massive black holes, present in most galactic nuclei today, have formed and grown over cosmic time (e.g., Dayal et al., 2018; Klein et al., 2016; Volonteri, 2010). It will explore almost all the mass-redshift parameter space relevant for reconstructing their evolution. The GW signal from coalescing black holes reveals their spin and redshifted mass, and the distribution of masses and spins will be studied to differentiate between different formation scenarios.

By observing highly relativistic black hole - black hole mergers, LISA will provide exceptionally strong tests of the predictions of General Relativity. The signal of merging binary black holes, interacting strongly with each other, where maximally warped vacuum spacetimes propagate at near the speed of light, allow the study of the full nonlinear dynamics of the theory of gravity (e.g., Barausse et al., 2016; Berti et al., 2016; Brito et al., 2017). By observing the signal of stellar black holes skimming the horizon of a large massive black hole at the centre of a galaxy, LISA will measure the mass, spin and quadrupole moment of the central object testing its level of "Kerrness"; thus testing the black hole hypothesis, and the no-hair conjecture (e.g., Barack & Cutler, 2007). LISA's contribution will be complementary to recent discoveries from direct imaging of black hole's shadow by the Event Horizon Telescope (EHT, Event Horizon Telescope Collaboration et al., 2019).

Finally, a space-based gravitational wave detector will probe new physics and cosmology, and will search for unforeseen sources of gravitational waves. The LISA frequency band in the relativistic early Universe corresponds to horizon scales where phase transitions of new forces of nature or extra dimensions of space may have caused catastrophic, explosive bubble growth and gravitational wave production.

1.5 Thesis outline

This thesis focuses on the study of Galactic ultra-compact detached DWD binaries as electromagnetic and gravitational wave sources. The main goal of this work is to broaden the scientific potential of GW sources detectable by LISA for Galactic studies and near-field cosmology. More importantly, this thesis aims to bridge GW and observational astronomy exploring the synergies between LISA and currently available, and future EM facilities. The results of this thesis represent an essential asset to forecast and design observational strategies for both EM and GW detectors in order to address a wealth of outstanding questions such as: *How do ultra-compact binaries form? What is their final fate? How are they distributed in the Galaxy; and what does that tell us about the formation and evolution of the Milky Way?* To address this overall goal, this thesis focuses on the following independent but complementary questions:

- What is the current census of potential multi-messenger GW+EM Galactic binaries?
- What are the future prospects for Galactic multi-messenger astronomy?

- How far beyond our Galaxy can LISA detect DWDs; and what are the properties of extra-galactic DWDs?

- What can we learn about the Milky Way by combining GW and EM observations?

Chapter 2 re-analyses the sample of the so-called verification binaries, i.e. known DWDs (from optical or X-ray observations) with expected GW signals above the LISA detection threshold. Predicting their GW signals depends on the masses of the binary components, their orbital separation, inclination and the distance. Prior to the *Gaia* mission, distances have been the most uncertain of these parameters. In this Chapter using state-of-the-art parallax measurements from the *Gaia* Data Release 2, the distances to the verification binaries are derived. This study shows that for the systems under investigation *Gaia* provides accurate distances for binaries which are at most a few hundred parsec away. These new measurements lead to the identification of 13 verification binaries: 9 AM CVn stars, 3 detached DWDs and 1 hot subdwarf. In particular, this study for the first time confirms a hot subdwarf (CD–30°11223) to be a guaranteed LISA source. Distances derived from *Gaia* parallaxes for CD–30°11223 and AM CVn also allow the GW amplitudes to be constrained to better than 5% and 10% respectively. For the remaining verification binaries the uncertainty of the GW amplitudes are now dominated by the uncertainties on the components' mass.

Chapter 3 outlines prospects for detection of new Galactic ultra-compact detached DWD in the next two decades with *Gaia*, LSST and LISA. Using a mock population of DWD, the expected number of eclipsing detached DWD is computed for *Gaia* and LSST. In addition, the efficiency of detecting eclipsing systems with *Gaia* and LSST is analysed as a function of binary orbital period. This chapter outlines an analytic recipe for the signal-to-noise ratio calculation of monochromatic GW sources. Using this analytic calculation 25 thousand GW signals are foreseen to be individually resolved by LISA. Finally, this chapter shows that several tens of combined EM and GW detections will be available when all three instruments will be operational, enabling future joint EM and GW (multi-messenger) studies. This chapter also describes the physical properties of these samples and compares them to the current data.

So far only detection prospects for the Milky Way have been predicted. **Chapter 4** shows that LISA has the potential to (individually) detect DWD systems also in the neighbouring galaxies, almost reaching the edge of the Local Group. It demonstrates that in the LMC and SMC, LISA can detect DWDs with $P < 20\,\mathrm{min}$ and $\mathcal{M} > 0.1\,\mathrm{M}_\odot$, while in M31 LISA will be sensitive to those with $P < 10\,\mathrm{min}$ and $\mathcal{M} > 0.6\,\mathrm{M}_\odot$. It is important to highlight that this parameter space defines double degenerate SNIa progenitor systems, that are virtually undetectable in external galaxies in the optical band. This means that LISA may be our best tool for validating the double degenerate SNIa formation channel. In this chapter quantitative estimates for detections in the Andromeda galaxy are provided. The expected number of detectable GW sources in Andromeda can be as high as a few, to several tens, all potential SNIa progenitors.

Chapter 5 proposes joint EM and GW observations of DWDs for constraining the shape of both Milky Way's stellar disc and bulge. It shows that GW signals from DWDs can be used for tracing the Galactic structure. In particular, it demonstrates that the distribution of individually resolved LISA detections will provide constraints on the Milky Way scale parameters, such as the scale radii and the scale height of the bulge and the disc. The power to constrain the overall properties of the Galactic

baryonic potential will be significantly enhanced by using GWs in combination with EM observations. The success of this synergy is due to LISA's ability to localise binaries through virtually the whole Galactic plane, thus mapping its shape, while optical observations yield the motion of stars, tracing the underlying total enclosed mass.

1.6 Future outlook

This thesis constitutes a first exploratory step towards the future Galactic multi-messenger (EM+GW) astronomy. By considering exclusively detached DWD binaries this work demonstrates that large samples of DWD can be discovered in EM and GW, with a significant overlap between the two, with the future facilities. Thus, a multi-messenger sample can be used for investigating not only evolution of close binary systems but also our Galaxy and the entire Local Group. Although other Galactic ultra-compact binaries such as AM CVn stars, hot subdwarfs and WD-NS binaries are not expected to be as numerous as detached DWD systems, they could have an advantage for multi-messenger synergies due to being brighter EM sources. Therefore, it is important to make similar assessments for these systems as has been done for DWDs.

Current BPS models of Galactic ultra-compact binaries are either designed to forecast EM observations, thus fine-tuned on nearby binaries neglecting the large scale structure of the Galaxy, or they are exclusively designed to model LISA data and are not calibrated on available observations. However, to forecast multi-messenger observations and assess synergies between EM facilities and the LISA mission the combination of both approaches is crucial. Hence, the next major step to broaden this work is to build one complete catalogue that includes all possible GW sources self-consistently generated by one BPS code. To build such a catalogue a detailed knowledge of the Galaxy, including the structure, dynamics, and dust distribution, which also account for the latest discoveries made using the *Gaia* data, is also required. Such a catalogue would represent an important tool for testing LISA science cases in the mission preparation phase.

It is of fundamental importance to continue testing BPS models against new observations because in the upcoming years, prior to the LISA launch, more and more ultra-compact binaries will be discovered with the advent of more powerful optical surveys. Some of the most prolific instruments in the optical wavebands will be *Gaia* (Gaia Collaboration et al., 2016), ZTF (Bellm et al., 2019), BlackGEM (Bloemen et al., 2015), LSST (LSST Science Collaboration et al., 2009), which will be complemented with surveys in other frequency bands (e.g. eROSITA and Athena in the X-rays and perhaps upcoming UV missions). The detailed follow-up for many sources will likely be completed with the next generation facilities such as the Extremely Large Telescope (ELT) or James Webb telescope and will allow precise EM studies of ultra-compact binaries. The future is "bright" for this research field ready for detailed EM+GW studies as soon as LISA starts observing.

Finally, one should not consider that all LISA science cases are fully explored, as these were assessed over the last decades by at least a few (scientific) generations. Instead, it is important to keep up with the latest astronomical discoveries to broaden the range of synergies with different topics. A good example, related to the topics investigated in this thesis, is the exploitation of the secondary effects in GW signals

for the identification of tertiary companions or circumbinary exoplanets (Robson et al., 2018; Steffen et al., 2018; Tamanini & Danielski, 2018). One should not forget that LISA is an exploratory mission, the first mission of its kind, and, as such, it allows us to work to the edge of our scientific imagination.

Chapter 2

LISA verification binaries with updated distances from Gaia Data Release 2

Kupfer, T., **Korol, V.**, Shah, S., et al. 2018, MNRAS, 480, 302

Ultra-compact binaries with orbital periods less than a few hours will dominate the gravitational wave signal in the mHz regime. Until recently, 10 of the known systems were predicted to have a predicted gravitational wave signal strong enough to be detectable by the Laser Interferometer Space Antenna (LISA), the so-called "verification binaries". System parameters, including distances, are needed to provide an accurate prediction of the expected gravitational wave strength to be measured by LISA. Using parallaxes from *Gaia* Data Release 2 we calculate signal-to-noise ratios (SNR) for $\approx$ 50 verification binary candidates. We find that 11 binaries reach a SNR$\geq$20, two further binaries reaching a SNR$\geq$5 and three more systems are expected to have a SNR$\approx$5 after four years integration with LISA. For these 16 systems we present predictions of the gravitational wave amplitude ($\mathcal{A}$) and parameter uncertainties from Fisher information matrix on the amplitude ($\mathcal{A}$) and inclination (i).

2.1 Introduction

The Laser Interferometer Space Antenna, (LISA) will be the first gravitational wave observatory in space (Amaro-Seoane et al., 2017). Operating in the low frequency part of the gravitational wave (GW) spectrum ($10^{-4} - 1$ Hz), *LISA* has been selected as ESA's third large mission of the Cosmic Vision Program. Amongst many other astrophysical sources, *LISA* will allow us to observe millions of ultra-compact (Galactic) binaries (UCBs) with orbital periods ($P_{\rm orb}$) shorter than a few hours (Amaro-Seoane et al. 2017) from which we will be able to individually resolve several thousands (e.g. Nelemans et al. 2004; Ruiter et al. 2009; Breivik et al. 2018; Kremer et al. 2017; Littenberg et al. 2013; Nissanke et al. 2012; Ruiter et al. 2010; Shah et al. 2012; Yu & Jeffery 2010). As indicated by their tight orbits, these systems are composed of degenerate stellar remnants, such as white dwarfs, neutron stars or stellar-mass black holes. Up to now several such sources have been detected in the electromagnetic (EM) bands. These include detached (Brown et al., 2016) and semi-detached double white dwarfs (the latter called AM CVn type binaries; Solheim 2010), and semi-detached white dwarf-neutron star binaries (so-called ultra-compact X-ray binaries; Nelemans & Jonker 2010) and double neutron stars (Lyne et al., 2004).

A subset of the known UCBs have orbital periods that lie in the LISA band and these will be individually detected due to their strong GW signals. These LISA-guaranteed sources are termed "verification binaries" with some being expected to be detected on a timescale of weeks or a few months (Stroeer & Vecchio, 2006). Therefore, they are crucial in facilitating the functional tests of the instrument and maximising the scientific output of *LISA*. So far we know of ten such systems, most of them being semi-detached AM CVn type: HM Cnc, V407 Vul, ES Cet, AM CVn, SDSS J190817.07+394036.4 (SDSS J1908), HP Lib, CR Boo, and V803 Cen (Espaillat et al., 2005; Green et al., 2018; Kupfer et al., 2015; Ramsay et al., 2005; Roelofs et al., 2006, 2007; Strohmayer, 2004). The remaining two are detached binary white dwarf systems: SDSS J065133.34+284423.4 (SDSS J0651) and SDSS J093506.92+441107.0 (SDSS J0935) (Brown et al., 2011; Kilic et al., 2014).

Predicting the gravitational wave strain depends on the masses of the binary components, which, together define the chirp mass (defined in Section 2.3.3), the orbital inclinations of the systems and their distance. Masses can be obtained, within limits, from optical spectroscopy and photometry, combined with the Roche-lobe geometry. In favourable situations, such as eclipsing systems, the orbital inclination can be determined from time-resolved spectroscopy and photometry (e.g. Brown et al. 2011), but it is generally rather poorly constrained. So far, distances remained the largest uncertainty. Only five of the known 52 semi-detached AM CVn type systems have HST-based parallaxes (Roelofs et al., 2007): AM CVn, HP Lib, CR Boo, V803 Cen and GP Com. Ground-based parallaxes were derived for AM CVn (C.Dahn, as quoted by Nelemans et al. 2004), GP Com (Thorstensen, 2003) and V396 Hya (Thorstensen et al., 2008). The remaining systems have distance estimates based on the comparison of model fluxes with the observations. These are considered highly uncertain as they require good knowledge of system parameters such as mass ratios, donor properties and accretion rates. Of the detached verification binary candidates, only one (WD 1242-105; Debes et al. 2015) has a parallax measurement. The remaining systems have indirect distance estimates based on the comparison of measured temperatures and surface gravities with stellar models (e.g. Althaus et al. 2013; Brown et al. 2016;

Table 2.1: Physical properties of the known verification binaries. Masses and inclination angles in brackets are assumed and based on evolutionary stage and mass ratio estimations

Source	$l_{\rm Gal}$ (deg)	$b_{\rm Gal}$ (deg)	Orbital period (sec)	m_1 ($M_\odot$)	m_2 ($M_\odot$)	i (deg)
AM CVn type						
HM Cnc[1,2]	206.9246	23.3952	321.529	0.55	0.27	≈38
V407 Vul[3]	57.7281	6.4006	569.395	[0.8±0.1]	[0.177±0.071]	[60]
ES Cet[4]	168.9684	–65.8632	620.21	[0.8±0.1]	[0.161±0.064]	[60]
SDSS J135154.46[5]	328.5021	53.1240	943.84	[0.8±0.1]	[0.100±0.040]	[60]
AM CVn[6,7]	140.2343	78.9382	1028.73	0.68±0.06	0.125±0.012	43±2
SDSS J190817.07[8,9]	70.6664	13.9349	1085.7	[0.8±0.1]	[0.085±0.034]	10 - 20
HP Lib[10,11]	352.0561	32.5467	1102.70	0.49-0.80	0.048-0.088	26-34
PTF1 J191905.19[12]	79.5945	15.5977	1347.35	[0.8±0.1]	[0.066±0.026]	[60]
CXOGBS J175107.6[13]	359.9849	–1.4108	1375.0	[0.8±0.1]	[0.064±0.026]	[60]
CR Boo[11,14]	340.9671	66.4884	1471.3	0.67-1.10	0.044-0.088	30
V803 Cen[11,15]	309.3671	20.7262	1596.4	0.78-1.17	0.059-0.109	12 - 15
Detached white dwarfs						
SDSS J065133.34[16,17]	186.9277	12.6886	765.5	0.247±0.015	0.49±0.02	$86.9^{+1.6}_{-1.0}$
SDSS J093506.92[18,19]	176.0796	47.3776	1188.0	0.312±0.019	0.75±0.24	[60]
SDSS J163030.58[18,20]	67.0760	43.3604	2389.8	0.298±0.019	0.76±0.24	[60]
SDSS J092345.59[18,21]	195.8199	44.7754	3883.7	0.275±0.015	0.76±0.23	[60]
Hot subdwarf binaries						
CD–30°11223[22]	322.4875	28.9379	4231.8	0.54±0.02	0.79±0.01	82.9±0.4

[1] Strohmayer (2005); [2] Roelofs et al. (2010); [3] Ramsay et al. (2002); [4] Espaillat et al. (2005); [5] Green et al. (2018); [6] Skillman et al. (1999); [7] Roelofs et al. (2006); [8] Fontaine et al. (2011); [9] Kupfer et al. (2015); [10] Patterson et al. (2002); [11] Roelofs et al. (2007); [12] Levitan et al. (2014); [13] Wevers et al. (2016); [14] Provencal et al. (1997); [15] Roelofs et al. (2007); [16] Brown et al. (2011); [17] Hermes et al. (2012); [18] Brown et al. (2016); [19] Kilic et al. (2014); [20] Kilic et al. (2011); [21] (Brown et al., 2010); [22] Geier et al. (2013);

Istrate et al. 2014).

In April 2018, the *Gaia* collaboration released sky positions, parallaxes, and proper motions for more than 1.3 billion sources, with a limiting magnitude of $G = 21$ mag (Gaia Collaboration et al., 2016, 2018). Here we present new results on the predicted gravitational wave signal detectable by LISA for known Galactic binaries using distances from *Gaia* Data Release 2 (DR2) and the current LISA baseline configuration. We calculate updated signal-to-noise (SNR) ratios. For the loudest known verification binaries with SNR> 5, we extract their GW parameter uncertainties using Fisher information matrix. For our analysis we define systems as verification binaries if the binary 1) is detected in the electromagnetic bands and 2) its SNR is ≥ 5 after 4 years of integration which is the nominal mission time for LISA.

2.2 The sample of verification binaries

Observationally, the known sample of 10 verification binaries is strongly biased and incomplete. This sample includes AM CVn, CR Boo, V803 Cen and ES Cet, which were all found as "outliers" in surveys for blue, high-Galactic latitude stars. The selection effects are difficult to accurately quantify and therefore not easy to model. HM Cnc

and V407 Vul are the most compact known systems and were discovered during the course of the *ROSAT* All-Sky Survey showing an on/off X-ray profile modulated on a period of 321 and 569 sec respectively (Israel et al., 1999; Motch et al., 1996). Their ultra-compact nature was later confirmed with optical observations (Israel et al., 2002; Ramsay et al., 2000, 2002; Roelofs et al., 2010). SDSSJ1908 was found as a short-period variable in the original Kepler field, where it was targeted as a potential subdwarf B-star pulsator (Fontaine et al. 2011; Kupfer et al. 2015).

Extremely low mass (ELM) white dwarf binaries such as SDSS J0651 and SDSS J0935 were discovered as part of a colour selected sample of B-type hypervelocity candidates from the Sloan Digital sky survey (SDSS; Brown et al. 2016 and references therein). ELM white dwarfs can be separated efficiently from the bulk of white dwarfs with a colour selection.

Studies of UCBs have been conducted almost exclusively at high Galactic latitudes and in the Northern hemisphere. It is therefore likely that more 'AM CVn'-like systems are awaiting discovery in the Southern hemisphere and at low Galactic latitudes. Binary population studies predict that LISA will detect several thousand detached and semi-detached double white dwarfs as well as a few tens of neutron star or black hole binaries with a population strongly peaking towards the Galactic Plane/Bulge (e.g. Nelemans et al. 2004). These studies suggest that about an equal fraction of semi-detached and detached systems are expected but the models over predict the number AM CVns observed in surveys like SDSS by at least a factor 10 (Carter et al., 2013; Roelofs et al., 2007), so the detached systems may well dominate. Most of the detached systems are predicted to consist of a carbon/oxygen + helium white dwarf binary system (Liu et al., 2010; Nelemans et al., 2001; Nelemans, 2013; Ruiter et al., 2010; Yu & Jeffery, 2010).

Although the currently known sample is still limited, upcoming and ongoing large scale high-cadence variability surveys which also cover low Galactic latitudes such as OmegaWhite (Macfarlane et al. 2015), ZTF (Bellm 2014), BlackGEM (Bloemen et al. 2015), GOTO (Steeghs 2017), *Gaia* and LSST (see Korol et al. 2017 for both) have the potential to discover an unbiased sample of LISA verification binaries. Indeed Korol et al. (2017) show that *Gaia*, LSST and LISA have the potential to detect respectively hundreds, thousands and tens of thousands of new ultra-compact double white dwarfs.

2.3 Methods

2.3.1 Mass assumption for systems without constraints

Mass estimation for AM CVn type systems are difficult because only the accretion disc and in some cases the accretor is visible in the spectra. So far the only AM CVn systems with direct measurements of the donor and the accretor mass are eclipsing systems. Copperwheat et al. (2010) found precise masses for SDSS J092638.71+362402.4 and more recently Green et al. (2018) derived precise masses for the first fully eclipsing AM CVn type system: Gaia 14aae. Both systems show a high accretor mass of 0.85 and 0.87 $M_\odot$ respectively. Additionally, both systems have donor stars which are inconsistent with a zero-temperature fully degenerate star. In both cases the donor is larger and more massive compared to what it is expected for a fully degenerate donor.

Table 2.2: Measured EM properties (parallax, distance) and derived GW parameters (f, $\mathcal{A}$, signal-to-noise ratio SNR) of the known verification binaries. The distance for HM Cnc is assumed. The strain amplitude ($\mathcal{A}$) is given in units of 10^{-23}. The SNR is calculated for four years integration with LISA.

Source	f (mHz)	ϖ (mas)	σ_ϖ (mas)	d (pc)	σ_d (pc)	$\mathcal{A}$	SNR
AM CVn type systems							
HM Cnc	6.22	-	-	[5000]	-	6.4	211.1±3.18
V407 Vul	3.51	0.095	0.327	1786	667	11.0±5.9	169.7±2.17
ES Cet	3.22	0.596	0.108	1584	291	10.7±4.6	154.3±2.09
SDSS J135154.46–064309.0	2.12	0.596	0.313	1317	531	6.2±3.5	21.8±0.24
AM CVn	1.94	3.351	0.045	299	4	28.3±3.2	101.2±0.96
SDSS J190817.07+394036.4	1.84	0.954	0.046	1044	51	6.1±2.4	20.3±0.13
HP Lib	1.81	3.622	0.052	276	4	17.5±3.9	43.7±0.28
PTF1 J191905.19+481506.2	1.48	0.550	0.327	1338	555	3.2±1.8	4.0±0.02
CXOGBS J175107.6–294037	1.45	1.016	0.146	971	156	4.2±1.8	4.5±0.02
CR Boo	1.36	-	-	337^a	$^{+44\,a}_{-35}$	13.4±4.2	21.9±0.13
V803 Cen	1.25	-	-	347^a	$^{+32\,a}_{-27}$	16.0±5.4	26.2±0.17
detached white dwarfs							
SDSS J065133.34+284423.4	2.61	1.000	0.476	933	493	16.2±8.6	90.1±1.13
SDSS J093506.92+441107.0	1.68	-	-	645^b	41^b	29.9±7.7	44.9±0.31
SDSS J163030.58+423305.7	0.84	0.937	0.270	1019	357	11.5±4.9	4.6±0.03
SDSS J092345.59+302805.0	0.51	3.340	0.173	299	10	26.4±6.5	5.6±0.06
hot subdwarf binaries							
CD–30°11223	0.47	2.963	0.080	337	9	41.5±1.8	4.9±0.04

[a]Roelofs et al. (2007), [b]Brown et al. (2016)

A large number of AM CVn systems have indirect constraints on the mass ratio (q) from the empirical relation of the superhump excess (Knigge, 2006).

$$q = (0.114 \pm 0.005) + (3.97 \pm 0.41) \times (\epsilon - 0.025) \tag{2.1}$$

where $\epsilon = \frac{P_{\rm sh} - P_{\rm orb}}{P_{\rm orb}}$ is the superhump excess. This is an empirical relation which gives similar results to that of Patterson et al. (2005) but with the inclusion of uncertainties on the fit parameters. The relation was derived for hydrogen-dominated cataclysmic variables but has not yet been well tested for AM CVn type systems. Green et al. (2018) applied the equation to 11 AM CVn systems with a measured superhump excess to derive the mass and radius for the donor under the assumption of an $0.7\pm0.1\,\mathrm{M}_\odot$, accretor. None of the tested systems are consistent with a fully degenerate donor but they are on average about 2.5 times the mass compared to a zero-temperature fully degenerate donor.

Based on this result and the measurements from the eclipsing systems we assume for systems without constraints on the component masses an accretor mass of $0.8\pm0.1\,\mathrm{M}_\odot$ and a donor mass 2.5 times the mass for a zero-temperature donor star. For the donor star we allow an error range of $1.5-3.5$ times the minimum mass. System properties for each system are given in Table 2.2.

2.3.2 Distance determination from *Gaia* DR2 parallaxes

Gaia DR2 provides parallaxes, not distances. In this Section we explain the procedure we adopt to convert parallaxes into distances.

To estimate distances from the measured parallaxes a probability-based inference approach is required (e.g. Astraatmadja & Bailer-Jones, 2016; Bailer-Jones, 2015; Bailer-Jones et al., 2018; Igoshev et al., 2016; Luri et al., 2018). Essentially, because any measured parallax (ϖ) follows a probability distribution, we can infer the distance in a probabilistic sense, if we make an assumption about the true distribution of observed sources in space (i.e. the prior distribution). Using Bayes' theorem the posterior probability density of the possible values for the distance can be expressed as

$$\begin{aligned} P(d|\varpi, \sigma_\varpi) &= \frac{1}{Z}\ P(\varpi|d, \sigma_\varpi)\ P(d); \\ Z &= \int_0^\infty P(\varpi|r, \sigma_\varpi)\ P(r)\, dr, \end{aligned} \tag{2.2}$$

where Z is the normalisation constant, $P(\varpi|d, \sigma_\varpi)$ is the likelihood function and $P(d)$ is the prior. The likelihood expresses the probability to measure the parallax ϖ for the source at the distance d with an uncertainty of the measurement σ_ϖ. For *Gaia* measurements we can assume a Gaussian noise model (Lindegren et al., 2018) and write the likelihood as

$$P(\varpi|\ d, \sigma_\varpi) = \frac{1}{\sqrt{2\pi}\ \sigma_\varpi} \exp\left[-\frac{1}{2\sigma_\varpi^2}\left(\varpi - \frac{1}{d}\right)^2\right]. \tag{2.3}$$

The prior $P(d)$ contains our assumption about the distance distribution of the sources. For measurements with fractional parallax errors σ_ϖ/ϖ less than about $0.1 - 0.2$, the distance estimates are mainly independent of the choice of prior. However, for larger fractional errors the quality of the distance estimates heavily depends on how well the prior reflects the true distribution of distances for the population of sources (e.g. Astraatmadja & Bailer-Jones, 2016; Bailer-Jones, 2015). For this work we adopt an exponentially decreasing volume density prior

$$P(d) = \begin{cases} \frac{d^2}{2L^3} \exp(-d/L) & \text{if } d > 0, \\ 0 & \text{otherwise,} \end{cases} \tag{2.4}$$

where $L > 0$ is the scale length. This prior performs well for a generic population, but fine-tuning is required to find the appropriate scale length L that describes *LISA* verification binaries (Astraatmadja & Bailer-Jones, 2016). We calibrate the value of L using the mock catalogue of detached double white dwarf binaries from Korol et al. (2017). The catalogue was obtained using the binary population synthesis model of Nelemans et al. (2001); Toonen et al. (2017) and designed to test the detectability of these binaries by *Gaia*, LSST and LISA. We select binaries in the catalogue with *Gaia* G magnitude < 21 and where parallax fractional error[1] > 0.2. A straightforward way of fine-tuning the value of L is to fit the distribution of synthetic binaries with the distance. Another way consists of finding the value of L that minimises the bias on our estimates due to a particular choice for L itself (e.g. Marchetti et al., 2018). The

[1]The errors on parallax for the mock population are estimated using pyGaia python tool kit.

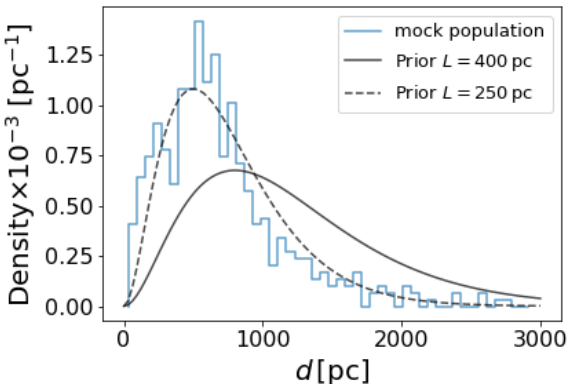

Figure 2.1: Distribution of synthetic detached double white dwarf binaries with distance from Korol et al. (2017) (blue line) and two exponentially decreasing volume density priors: $L = 250$ pc (dashed black line) and $L = 400$ pc (solid black line).

latter implies the following calculations. For each binary we determine the mode of the posterior distribution $P(d|\varpi, \sigma_\varpi)$. The mode is an unbiased estimator and provides meaningful estimates when the posterior is highly asymmetric. To determine the mode of $P(d|\varpi, \sigma_\varpi)$ given our choice of the prior, we set the derivative of the posterior to be equal to zero and solve the equation (Bailer-Jones, 2015):

$$\frac{d^3}{L} - 2d^2 + \frac{\varpi d}{\sigma_\varpi^2} - \frac{1}{\sigma_\varpi^2} = 0. \tag{2.5}$$

We repeat this calculation using a range of values for L for each binary in the mock catalogue. We define the best value of L as the one that minimises the difference between the mode, obtained by solving equation (2.5), and the true distance of the binary in the catalogue. We obtain $L = 400$ pc.

In Figure 2.1 we show the distribution of synthetic binaries with the distance (blue line) and two exponentially decreasing volume density priors: one with $L = 250$ pc (dashed black line), that represents the best fit to the distribution of mock binaries, and another one with $L = 400$ pc (solid black line), obtained by minimising the bias. The figure shows that the curve with $L = 400$ pc decreases slower and is more representative of binaries at large distances, where fractional errors on parallax are large. Thus, for this work we adopt the scale length of 400 pc such that we avoid underestimating distances for the furthest binaries.

Finally, following Bailer-Jones (2015) we associate the most probable value of d with the mode of the posterior distribution, and we compute the errors as

$$\sigma_d = \frac{d_{95} - d_5}{2s}, \tag{2.6}$$

where d_{95} and d_5 are the boundaries of the 90% credible interval of the $P(d|\varpi, \sigma_\varpi)$ distribution that are calculated symmetrically about the median and $s = 1.645$, which is the ratio of the 90% to 68.3% credible interval for a Gaussian distribution. HM Cnc, CR Boo, V803 Cen and SDSS J093506.92+441107.0 have no measured parallax from

Gaia DR2. For HM Cnc we assumed 5 kpc and discuss the uncertainty on the distance in detail in Section 2.5. For the other three systems the previously published distant estimates were used. The results are listed in Table 2.2.

2.3.3 Strain and SNR calculations

To compute the expected characteristic strain we first calculate the dimensionless gravitational wave amplitude ($\mathcal{A}$) using equation 3 from Shah et al. (2012):

$$\mathcal{A} = \frac{2(G\mathcal{M})^{5/3}}{c^4 d}(\pi f)^{2/3} \tag{2.7}$$

where $\mathcal{M}$ is the chirp mass, $\mathcal{M} \equiv (m_1 m_2)^{3/5}/(m_1 + m_2)^{1/5}$, m_1 and m_2 the masses of the two components, where we assume $m_1 > m_2$, d is the distance to the source as defined in Section 2.3.2 and f the gravitational wave frequency with $f = 2/P_{\rm orb}$. The characteristic strain (h_c) for individual verification binaries was calculated following the approach described in Section 2.2 in Moore et al. (2015):

$$h_c = \sqrt{N_{\rm cycle}}\mathcal{A} \tag{2.8}$$

where $N_{\rm cycle} = fT_{\rm obs}$. For the calculations we assume that LISA will observe for four years. The masses and gravitational wave frequency for each system are given in Tables 2.2 and 2.3.

Most of the *LISA* verification binaries can be characterised as monochromatic GW signals with a set of seven parameters, $\mathcal{A}$, f, polarisation angle (ψ), initial GW phase (ϕ_0), orbital inclination (i), ecliptic latitude ($\sin\beta$), and ecliptic longitude (λ). An additional eighth parameter, the period derivative or chirp ($\dot{f}$) is used for HM Cnc, V407 Vul and SDSS J0651 which have measured orbital decay rates from their EM data, $\dot{P}_{\rm orb}$: $3.75 \times 10^{-11} ss^{-1}$ (Roelofs et al. 2010), $3.17 \times 10^{-12} ss^{-1}$ (Ramsay et al. 2005), $9.8 \pm 2.8 \times 10^{-12} ss^{-1}$ (Hermes et al. 2012) respectively. They are related to the GW decay rate, $\dot{f}$ by $-\dot{P}_{\rm orb}/P^2_{\rm orb}$ used in simulating their GW signals. We compute Fisher matrices (e.g Cutler 1998) to extract the GW parameter uncertainties and correlations. The method and application of Fisher information matrix (FIM) for the *LISA* compact binaries together with their signal modelling and the noise from the detector and the Galactic foreground have been described in detail in Shah et al. (2012).

Here we use the current configuration for the LISA detector (Amaro-Seoane et al. 2017) with arm length of 2.5×10^6 km and six laser links exchanged along the three arms of the detector, from which we can generate two sets of the optimal data streams from two channels yielding two independent time-series whose noises are uncorrelated maximising the SNR[2]. Detailed discussions of the possible data streams using various sets of laser links can be found in e.g Vallisneri (2005). The unresolved foreground is obtained by using the recently updated catalogue for detached double white dwarf binaries whose simulation and binary evolution is described in Toonen et al. (2017).

We obtain the SNR from the GW signal over 15 instrumental noise realisations for the bright verification binaries using the nominal EM measurements to estimate the GW parameters in the GW signal model. For details we refer to Section 3 in Shah et al. (2012). Given the GW signal of the binary and a Gaussian noise we

[2]We use the Time Delay Interferometry (TDI) A and E observables

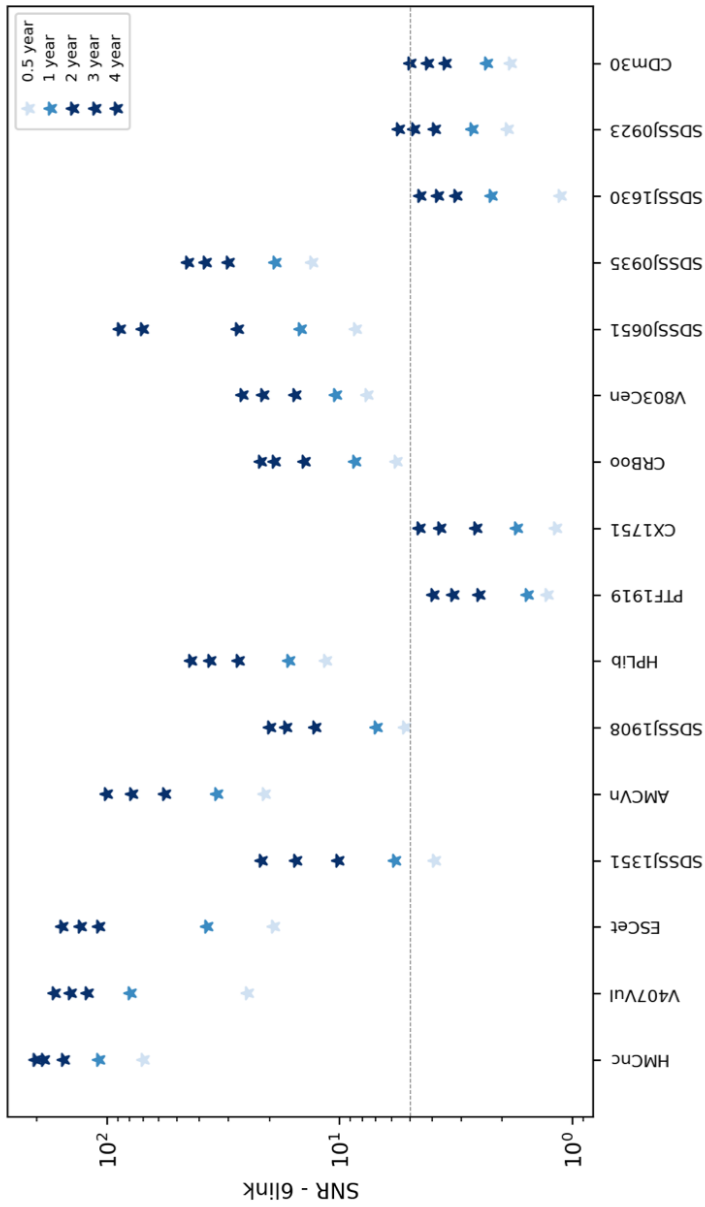

Figure 2.2: SNR evolution with time for the LISA verification binaries. The black dashed line corresponds to SNR= 5.

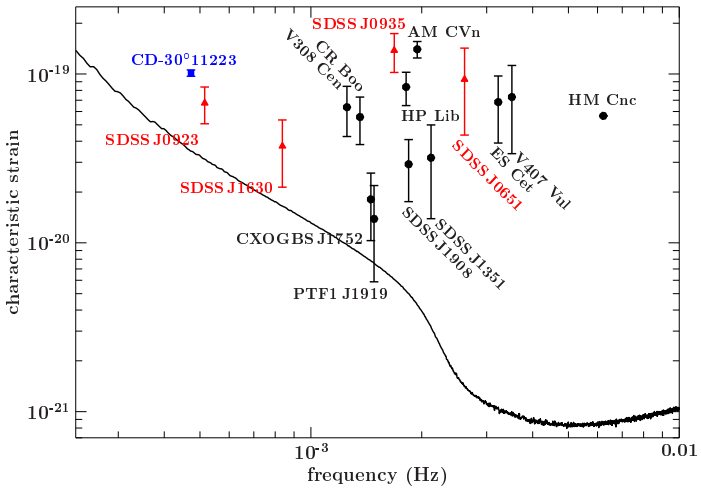

Figure 2.3: Sensitivity plot for *LISA* adopted assuming 4 years integration from Amaro-Seoane et al. (2017) showing the verification binaries which reach a SNR$\geq$ 5 or are on the border to a SNR$\approx$5 after 4 years integration. Black circles are AM CVn systems, red triangles correspond to detached white dwarfs and the blue square is the hot subdwarf binary. Note that the gravitational frequency shown here is twice the orbital frequency of the binaries. We assume a distance of 5 kpc for HM Cnc.

can use FIM to estimate the parameter uncertainties. The inverse of the FIM is the variance-covariance matrix whose diagonal elements are the GW uncertainties and the off-diagonal elements are the correlations between the two parameters. We do the GW analysis of the above mentioned verification binaries for LISA observations of four years. We note that the Fisher-based method is a quick way of computing parameter uncertainties and their correlations in which these uncertainties are estimated locally at the true parameter values and therefore by definition the method cannot be used to sample the entire posterior distribution of the parameters. Additionally Fisher-based results hold in the limit of strong signals with a Gaussian noise (see the Appendix in Shah & Nelemans 2014)[3].

2.4 Results

We calculate the distance and expected SNR following the description outlined in Section 2.3 for $\approx$50 semi-detached and detached candidate verification binaries with the strongest expected gravitational wave signals. Table 2.2 presents the predicted gravitational wave amplitude ($\mathcal{A}$) as well as the expected SNR after 4 years integration with *LISA* for all systems with SNR$\geq$5 and systems which are on the border to a SNR $\approx$ 5.

We find that 13 systems reach a SNR $\geq$5 after four years observing with LISA and therefore are confirmed verification binaries based on the definition adopted in Section 2.1. The population consists of 9 AM CVn binaries: HM Cnc, V407 Vul, ES Cet,

[3]The code used to perform the simulation is available at https://doi.org/10.17617/1.68

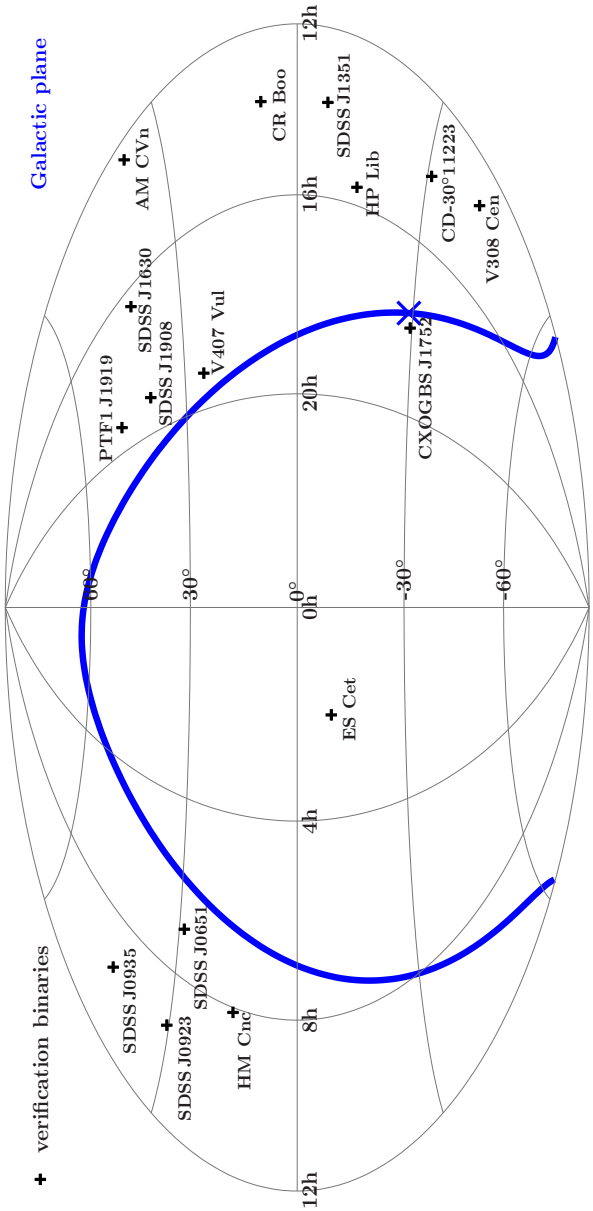

Figure 2.4: Sky position of the verification binaries. The sky positions show a clear bias towards the Northern hemisphere and to higher Galactic latitudes. The blue line indicates the Galactic Plane, with the Galactic Centre located at the blue cross.

Table 2.3: GW parameter uncertainties for the bright verification binaries from Fisher Information Matrix after four years of LISA integration

Source	SNR	$\sigma_{\mathcal{A}/\mathcal{A}}$	$\sigma_i[^\circ]$	$c_{\mathcal{A}\,i}$
HM Cnc	211.1±3.18	0.07±0.001	5.82±0.08	0.991±0.029
V407 Vul	169.7±2.17	0.028±0.000	1.34±0.02	0.907±0.023
ES Cet	154.3±2.09	0.032±0.000	1.44±0.02	0.911±0.024
SDSS J135154.46–064309.0	21.8±0.24	0.218±0.002	10.22±0.11	0.911±0.020
AM CVn	101.2±0.96	0.113±0.001	8.03±0.08	0.985±0.018
SDSS J190817.07+394036.4	20.3±0.13	5.622±0.036	–[a]	1.000±0.013
HP Lib	43.7±0.28	0.599±0.004	63.82±0.41	0.997±0.013
PTF1 J191905.19+481506.2	4.0±0.02	1.218±0.008	57.54±0.33	0.909±0.011
CXOGBS J175107.6–294037	4.5±0.02	1.057±0.005	49.65±0.33	0.909±0.009
CR Boo	21.9±0.13	1.173±0.007	126.05±0.72	0.997±0.011
V803 Cen	26.2±0.17	4.647±0.029	–[a]	1.000±0.013
SDSS J065133.34+284423.4	90.1±1.13	0.022±0.000	0.65±0.01	0.159±0.004
SDSS J092345.59+302805.0	44.9±0.31	0.106±0.001	4.99±0.03	0.909±0.013
SDSS J163030.58+423305.7	4.6±0.03	1.064±0.008	49.29±0.39	0.909±0.014
SDSS J092345.59+302805.0	5.6±0.06	0.834±0.009	39.51±0.44	0.908±0.020
CD–30°11223	4.9±0.04	0.425±0.004	12.52±0.13	0.359±0.007

[a]The FIM uncertainty exceeds the physically allowed range by i and thus cannot be determined from GW data analysis Shah & Nelemans (2014)

SDSS J1351, AM CVn, SDSS J1908, HP Lib, CR Boo and V803 Cen, 3 double white dwarfs: SDSS J0651, SDSS J0935 and SDSS J0923 as well as CD–30°11223 the first verification binary consisting of a hot subdwarf star with a massive white dwarf companion. Additionally, we find three more systems (PTF1 J1919, CXOGBS J1751 and SDSS J1630) with a SNR of ≈ 5 or just below 5, making them good candidates for being verification binaries.

Figure 2.2 shows the evolution of the SNR after 0.5, 1, 2, 3 and 4 years. The loudest source is HM Cnc which reaches a SNR=211 after four years of integration and already SNR=69 after 0.5 years, but whose distance is, even after *Gaia* DR2, still poorly constrained. PTF1 J1919, CXOGBS J1751, SDSS J1630, SDSS J0923 and CD–30°11223 need four years of integration to reach a SNR$\approx$5. Figure 2.3 shows the LISA sensitivity curve and the characteristic strain of the verification binaries after four years observing with LISA.

Table 2.3 shows the parameter uncertainties extracted from the FIM. Of the seven GW parameters characterising a binary, the astrophysically interesting ones are the amplitude ($\mathcal{A}$) and the inclination (i). Shown are the relative $1-\sigma$ error in $\mathcal{A}$, absolute $1-\sigma$ error in i and the normalised correlation between the two parameters $c_{\mathcal{A}\,i}$. The SNR influences the parameter uncertainties. Then the correlation $c_{\mathcal{A}\,i}$ has a strong influence on their uncertainties (Shah et al. 2012). As a result the systems with lower inclinations (or face-on orientations) with $i = [0^\circ - 45^\circ]$ have a strong correlation due to the GW signals being indistinguishable by making changes in $\mathcal{A}$ or ia. This explains the large errors in $\mathcal{A}$ and undetermined i (since the GW uncertainties are greater than the physical values i can take: $0^\circ - 360^\circ$) for systems such as SDSS

J190817.07+394036.4, CR Boo and V803 Cen despite that their SNRs are greater than 20. Whereas CD–30°11223 has a better constrained inclination even though its SNR is lower at ≈ 5.

2.5 Discussion

The only remaining system without a distance measurement is HM Cnc: distance is therefore the largest uncertainty when predicting its $\mathcal{A}$ and SNR for LISA. Given its known properties we argue that 10 kpc is the most conservative estimation for the distance. Although $\mathcal{A}$ and SNR remain uncertain, we find that even at a distance of 10 kpc, HM Cnc will have a SNR$\approx$100 after four years observing with LISA Hence it remains a bright verification binary even if the distance is significantly greater than the assumed 5 kpc.

Although there is a *Gaia* parallax measurement for V407 Vul (0.095 ± 0.327), the optical counterpart is dominated by a component that matches a G-type star, with a blue variable component in phase with the binary making up only 10-40% of the flux (Steeghs et al. 2006). The probability that this is an unrelated chance alignment of a foreground object is small, but the specific association of this G-star component with the ultra-compact binary is unclear. Given that this star dominates the *Gaia* passband, we assume here that the parallax measurement for V407 Vul is essentially that of the G-star component, and adopt this also for the ultra-compact binary component given the close on-sky alignment.

With the current LISA configuration and four years of observation, $> 25 \times 10^3$ binaries[4] are expected to be individually detected by LISA. However, only a small fraction will be bright enough to be detectable in the optical. Nelemans et al. (2004) predict that 143 short period semi-detached LISA verification systems (3 in the direct-impact phase) with $P_{\rm orb} < 1500$ s and brighter than 20 mag should be detectable in the optical wavebands. More recent work by Korol et al. (2017) predict several tens, up to one hundred, detached double white dwarfs will be detectable in the optical bands by *Gaia* and LSST as eclipsing sources, those with high SNR from their gravitational waves and brighter than 24 mag. The eclipsing systems only represent a small fraction of the full sample and we expect that there are about 100 detached double white dwarfs with orbital periods below 10 min and brighter than 24 mag and therefore potentially detectable with LSST.

Since verification binaries are a Galactic population their surface density is expected to strongly peak near the Galactic Plane. Most of the known systems are located in the Northern hemisphere and only a few systems were found at low Galactic latitudes. This shows that the current sample is likely very incomplete and biased. Figure 2.4 shows the sky position of the 16 systems. Upcoming and ongoing large scale optical surveys such as OmegaWhite (Macfarlane et al. 2015), ZTF (Bellm 2014), BlackGEM (Bloemen et al. 2015), GOTO (Steeghs 2017), *Gaia* and LSST (see Korol et al. 2017 for both) are expected to discover a more unbiased sample across both hemispheres and at low Galactic latitudes before LISA gets launched.

[4]Estimate from the foreground simulation using Korol et al. (2017) catalogue

2.6 Summary and Conclusions

In this work we derived distances from *Gaia* DR2 parallaxes for ≈50 verification binary candidates. Using these distances, we calculated the expected SNR after four years integration with LISA with a configuration of 6 laser links and 2.5 Gm arm lengths. Given the definition of a verification binary as SNR≥5 after four years integration, we find a total of 13 verification binaries. Eleven systems reach a SNR≥20 and two additional systems reach a SNR≥5 after four years. Additionally we find three more systems which are expected to have a SNR≈5 after four years integration with LISA and are good candidates for being verification binaries. Our study confirmed the first hot subdwarf binary as a LISA verification binary.

So far, distances have been the most uncertain parameter when predicting the gravitational wave strengths of the bright verification binaries. This is in particular true for the systems with the most accurate constraints on system parameters such as masses, inclinations and orbital periods. We find that *Gaia* provides accurate distances in particular for systems which are at most a few hundred parsec away. This allows us to predict the gravitational wave amplitude ($\mathcal{A}$) with an accuracy better than 5 % in the case of CD–30°11223 and around 10 % for AM CVn itself, making these systems ideal for the performance validation of LISA. For the remaining systems with distances of a few hundred parsec (e.g. HP Lib and SDSS J0923), the uncertainty of the gravitational wave amplitude is now dominated by the uncertainty on the component masses. For these systems and future discoveries precise mass measurements are required to provide estimations on the gravitational wave strength with a precision of a few percent.

Chapter 3

Prospects for detection of detached double white dwarf binaries with Gaia, LSST and LISA

Korol, V., Rossi, E. M., Groot, P. J., et al. 2017, MNRAS, 470, 1894

Double white dwarf (DWD) binaries are expected to be very common in the Milky Way, but their intrinsic faintness challenges the detection of these systems. Currently, only a few tens of *detached* DWDs are known. Such systems offer the best chance of extracting the physical properties that would allow us to address a wealth of outstanding questions ranging from the nature of white dwarfs, over stellar and binary evolution to mapping the Galaxy. In this paper we explore the prospects for detections of ultra-compact (with binary separations of a few solar radii or less) detached DWDs in: 1) optical radiation with *Gaia* and the LSST and 2) gravitational wave radiation with LISA. We show that *Gaia*, LSST and LISA have the potential to detect respectively around a few hundreds, a thousand, and 25 thousand DWD systems. Moreover, *Gaia* and LSST data will extend by respectively a factor of two and seven the guaranteed sample of binaries detected in electromagnetic and gravitational wave radiation, opening the era of multi-messenger astronomy for these sources.

3.1 Introduction

On the basis of our theoretical understanding of stellar and binary evolution, systems of two white dwarfs in a close binary were predicted since 1980s (thereafter double white dwarf (DWD) binaries) (Han, 1998; Iben & Tutukov, 1984; Iben et al., 1997; Nelemans et al., 2000, 2001; Toonen et al., 2012; Tutukov & Yungelson, 1981, 1988; Webbink, 1984). However, due to their intrinsic faintness the first detection came only a decade later in 1988 (Saffer et al., 1988). The current census counts a few tens of DWDs discovered by spectroscopic and variability surveys such as the SPY (ESO SN Ia Progenitor) survey (e.g. Napiwotzki et al., 2003), the ELM (Extremely Low Mass WDs) survey (e.g. Brown et al., 2010), and studies by Marsh (1995); Marsh et al. (1995); Maxted & Marsh (1999) and Badenes et al. (2009). Still, these represent only a tiny fraction of DWD binaries predicted in numerical simulations (Toonen et al., 2017).

Substantial progress in the detection of these sources is expected with optical wide surveys such as *Gaia* (Gaia Collaboration et al., 2016) and the Large Synoptic Survey Telescope (LSST) (LSST Science Collaboration et al., 2009), and in gravitational waves with the Laser Interferometer Space Antenna (LISA) mission (e.g. Amaro-Seoane et al., 2017). All three instruments will be sensitive to short period ($P <$ a few days) binaries (e.g., Carrasco et al., 2014; Eyer et al., 2012; Nelemans, 2013; Prša et al., 2011) and will provide a large sample of new ultra-compact DWDs that are interesting for several reasons. First, compact DWDs are systems that experienced at least two phases of mass transfer, and thus provide a good test for binary evolution models, and, in particular, for our understanding of mass transfer and the common envelope (CE) phase. Second, DWDs are the plausible progenitors to a wide range of interesting systems: type Ia supernovae (Iben & Tutukov, 1984; Webbink, 1984), that are used as cosmological distance indicators (e.g. Perlmutter et al., 1999; Riess et al., 1998), AM CVn systems (e.g. Marsh et al., 2004; Nelemans et al., 2001; Solheim, 2010; Steeghs et al., 2006) and "fast optical transient" including .Ia supernovae, Ca-rich transients and fast/bright transients (Bildsten et al., 2007; García-Berro et al., 2017; Perets et al., 2010).

In addition, it is believed that the merger of two WDs can produce rare stars such as massive WDs (or even an isolated neutron star), subdwarf-O and R Corona Borealis stars (Webbink, 1984). Third, DWDs represent guaranteed sources for the LISA mission, and will dominate the low frequency gravitational wave band from mHz to a few Hz (e.g. Evans et al., 1987; Hils et al., 1990; Lipunov & Postnov, 1987; Marsh, 2011; Nelemans et al., 2004). Finally, detached DWD binaries with orbital periods in the range from one hour to a few minutes are particularly suitable for studying the physics of tides, a phenomenon directly related to the WD internal properties. The study of the reaction of the stellar internal structure to tidal forces may give us important information, for example, on WD viscosity and its origin, that will complete our knowledge on WD interior matter (Dall'Osso & Rossi, 2014; Fuller & Lai, 2012; McKernan & Ford, 2016; Piro, 2011).

In this paper we compute the size of a sample of Galactic ultra-compact detached DWD binaries that could be obtained with future facilities in the next two decades. In particular, we predict the size (likewise Cooray et al., 2004; Littenberg et al., 2013; Shah et al., 2013) and properties of the sample that will be observed in both electromagnetic (EM) and gravitational wave (GW) radiation by *Gaia*, LSST and LISA:

Table 3.1: Distribution of the initial binary parameters.

Parameter	Distribution	Range of definition
Mass of stars	Kroupa IMF[a]	$0.95 < M\ \mathrm{M}_\odot < 10$
Binary mass ratio	uniform in q[b]	$0 < q \leq 1$
Orbital separation	uniform in $\log a$[c]	$0 \leq \log \frac{a}{\mathrm{R}_\odot} \leq 6$
Eccentricity	thermal[d]	$0 \leq e \leq 1$
Inclination	uniform in $\cos i$	$0 \leq \cos i \leq 1$

[a] Kroupa et al. (1993); [b] Duchêne & Kraus (2013);
[c] Abt (1983); [d] Heggie (1975);

despite the widespread expectation that those instruments will represent major step forwards, quantitative predictions have never been published. We characterise the physical properties of these samples and compare them to current data.

The paper is organised as follows. In Section 3.2 we will describe the method we use to simulate the Galactic population of DWDs. In Section 3.3 we will estimate how many binaries can be detected with *Gaia* and LSST as eclipsing sources. In Section 3.4 we will focus on the GW emission from these sources and we assess the prospects for detections by the upcoming LISA mission. In Section 3.5 we will present and characterise the sample of DWDs detectable trough EM and GW radiation. Finally, we will discuss our results and possible synergies between GW and EM data.

3.2 Simulated DWD population

To obtain a model sample of the Galactic DWD population we use the binary population synthesis code SeBa, developed by Portegies Zwart & Verbunt (1996, for updates see Nelemans et al. 2001, Toonen et al. 2012). The initial stellar population is obtained from a Monte Carlo based approach, assuming a binary fraction of 50% and distributions of the the initial binary parameters in Table 1. In particular, we draw the mass of single stars from the Kroupa Initial mass function (IMF, Kroupa et al., 1993). The mass of the secondary star is drawn from a flat mass ratio distribution. This is a poorly constrained relationship that, in general, depends on the stellar population. A typical progenitor of a DWD component is an A type star (De Rosa et al., 2014). For this stellar type a flat mass ratio distribution is a good first order approximation when comparing to observations (Duchêne & Kraus, 2013). The orbit eccentricity is drawn from a thermal distribution expected from an energy equipartition argument and often recovered from observations (Heggie, 1975; Raghavan et al., 2010). Besides, DWDs lose the memory of the initial orbital eccentricity because they circularise at quite early stages of their evolution, thus the shape of the initial eccentricity distribution hardly influences our simulation. The most common assumptions for the binary orbital period (or semi-major axis) distribution are: logarithmically-flat and log-normal. For intermediate-mass and solar-mass stars both are consistent with observations (e.g., Duchêne & Kraus, 2013; Poveda et al., 2007; Raghavan et al., 2010; Tokovinin et al., 2014). The largest differences between the two are expected for both very short or for very long period systems, but such systems are not likely to be progenitors of a typical DWD. Moreover, Toonen et al. (2017, see Table 4 and 5) do not

find significantly different numbers of DWDs when performing simulations (analogous to ours) with both logarithmically-flat and log-normal distributions. Therefore in our simulation we adopt a logarithmically-flat distribution. Finally, for each binary we assign an inclination angle i, drawn from the uniform distribution in $\cos i$. We explore the sensitivity of these assumptions by performing simulations for different choice of the IMF and mass ratio relation. We discuss the impact of our assumptions in Sect. 6.

To take into account the star formation history of the Galaxy, we exploit a code originally developed by Nelemans et al. (2001, 2004) and updated by Toonen & Nelemans (2013). The code distributes binaries according to a Galactic model with two components: disc and bulge. The density of DWDs in the disc is given by

$$P(R,t,z) = \rho_{\rm BP}(R,t)\,\mathrm{sech}^2\left(\frac{z}{z_{\rm h}}\right)\ \mathrm{pc}^{-3}, \tag{3.1}$$

where $0 \leq R \leq 19$ kpc is the cylindrical radius from the Galactic centre, $\rho_{\rm BP}$ is the result of the integration in R and t of the plane-projected star formation rate (SFR) from Boissier & Prantzos (1999), z is height above the disc, $z_{\rm h} = 300$ pc is the disc scale hight, and the age of the Galaxy is assumed to be 13.5 Gyr (Binney & McMillan, 2011; Jurić et al., 2008). We neglect the dependence on the stellar age and mass when assigning z, and we assume that there is no radial migration of the stars in time. We model the Galactic bulge by doubling the SFR in the inner 3 kpc of the Galaxy and distributing sources spherically:

$$\rho_{\rm bulge}(r) \propto e^{(r/r_{\rm b})^2}\ \mathrm{pc}^{-3}, \tag{3.2}$$

where r is the spherical distance from the Galactic centre and $r_{\rm b} = 0.5$ kpc is the characteristic radius of the bulge (Binney & McMillan, 2011; Sofue et al., 2009). We normalize equation (5.2) such that the total mass of the bulge at $t = 13.5$ Gyr is 2.6×10^{10} $\mathrm{M}_\odot$. The resulting distribution of DWDs at different Galactic ages is represented in Fig. 3.1. To show the portion of the Galaxy that can be potentially observed by *Gaia* and LSST we colour in magenta and blue respectively stars with apparent magnitudes < 20 and < 24.

The absolute magnitudes for WDs are deduced from the WD cooling curves of pure hydrogen atmosphere models (Holberg & Bergeron, 2006; Kowalski & Saumon, 2006; Tremblay et al., 2011, and references therein[1]). To convert the absolute magnitudes to observed magnitudes (e.g. for the Sloan r band) we use the following expression:

$$r_{\rm obs} = r_{\rm abs} + 10 + 5\log d + 0.84A_{\rm V}, \tag{3.3}$$

where d is the distance to the source in kpc, $0.84A_{\rm V}$ is the extinction in the Sloan r band, obtained from the extinction in the V band, $A_{\rm V}$. To compute the value of $A_{\rm V}$ at the source position, defined by the Galactic coordinates (l, b) at the distance d, we use

$$A_{\rm V}(l,b,d) = A_{\rm V}(l,b)\tanh\left(\frac{d\sin b}{h_{\rm max}}\right), \tag{3.4}$$

where $A_{\rm V}(l,b)$ is the integrated extinction in the direction defined by (l,b) from Schlegel et al. (1998), $h_{\rm max} \equiv \min(h, 23.5 \times \sin b)$ and $h = 120$ pc is the Galactic

[1]See also http://www.astro.umontreal.ca/ bergeron/ CoolingModels.

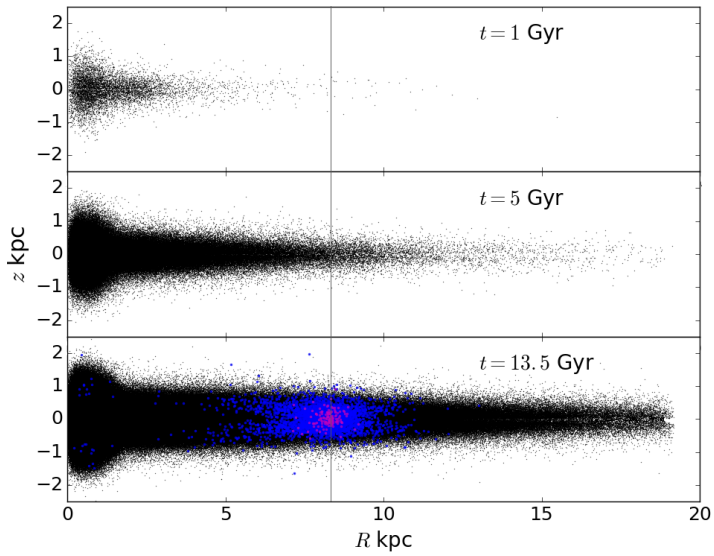

Figure 3.1: The distribution of DWDs in the Galaxy at $t = 1, 5$ and 13.5 Gyr. R is the cylindrical radius from the Galactic center and z is the height above the Galactic disc. The gray vertical line marks the position of the Sun. We represent in magenta and blue respectively DWDs potentially accessible to *Gaia* and to LSST.

scale height of the dust (Jonker et al., 2011). To convert r magnitudes into *Gaia* G magnitude we applied a colour-colour polynomial transformation with coefficients according to Carrasco et al. (2014, table 6). Finally, for our simulation we apply a magnitude limit of $r = 70$ and a period limit of $P = 20$ days. The magnitude limit is chosen to ensure that the simulated population can also be used for the GW detection simulations.

There are at least two phases of mass transfer in the standard picture of formation of a DWD system. To form a short-period DWD binary at least one mass transfer phase needs to be a CE (Paczynski, 1976; Webbink, 1984). In our simulation we adopt two evolutionary scenarios, with two different treatments of the CE phase: the $\alpha\alpha$ and the $\gamma\alpha$ scenarios. In the $\alpha\alpha$ scenario the CE phase is described by the so-called α-formalism (see Ivanova et al., 2013, for review). In this prescription, the CE outcome is determined by the conservation of the orbital energy (Webbink, 1984), where α represents the efficiency in the exchange of the orbital energy and the binding energy of the envelope, described by another free parameter of the model λ. The two parameters can be combined using equations (3.2) and (3.3) of Toonen & Nelemans (2013) to a single unknown $\alpha\lambda$. Based on Nelemans et al. (2000) we adopt to be $\alpha\lambda = 2$. In the second scenario, proposed in order to explain properties of observed DWDs, the CE is described by an alternative γ parametrization (Nelemans et al., 2000; Nelemans & Tout, 2005). In the γ-formalism the binary orbital evolution is driven by angular momentum loss, that is carried away through the mass loss process, and γ is the efficiency of this mechanism. In the $\gamma\alpha$ prescription the γ-formalism is applied whenever a binary does not contain a compact object or when the CE is not

Table 3.2: *Gaia* and the LSST technical characteristics. The quoted parameters are from Gaia Collaboration et al. (2016) and LSST Science Collaboration et al. (2009).

	Gaia	LSST
Sky coverage	whole sky	$\sim 1/2$ sky
Wavelength coverage	330-1050 nm	*ugrizy*
Bright limit	-	$r \simeq 16 - 17$
Depth per observation	$G \simeq 20.7$	$r \simeq 24$
Syst. photometric error (mag)	0.001	0.005
Integration time (sec)	40.5	15 + 15
Nominal mission lifetime	5 yr	10 yr
Average number of observations	70	10^3
Average cadence of observations	1 in 26 days	1 in 3 days

driven by a tidal instability, in which case the α prescription is used. Thus, in the $\gamma\alpha$ scenario, the first CE is typically described by the γ formalism and the second by the α formalism. For this scenario we assume the value of the $\alpha\lambda$ as in the $\alpha\alpha$ CE model and $\gamma = 1.75$ (Nelemans et al., 2000).

The main differences between the two populations obtained with these different prescriptions are: the total number of binaries and their mass ratio distribution. Using the $\gamma\alpha$ model one typically obtains twice as many binaries compared to the $\alpha\alpha$ scenario. Moreover, the mass ratio distribution in the $\gamma\alpha$ spans a wider range of values, which agrees better with the currently observed DWD population, while the majority of the population formed via $\alpha\alpha$ scenario will show mass ratios around 0.5 (see Toonen et al., 2012, figure 2). This is due to the fact that in the α prescription the orbit always shrinks significantly. When using the γ prescription the CE outcome heavily depends on the binary mass ratio (see, e.g., Equation (A.16) of Nelemans et al., 2001): for a roughly equal mass binary the orbit does not change much, however, for a binary with very different mass components the orbit shrinks strongly.

3.3 EM detection

In this section we focus our analysis on two instruments: *Gaia* and the LSST. Being photometric variability surveys, both are expected to mostly detect new DWDs through eclipses (Eyer et al., 2012), and thus selecting mainly short period ones. These DWDs are the most interesting for studying the final stages of binary evolution and represent potential gravitational wave sources.

Gaia is a space mission, launched on 19 December 2013, whose primary goal is to provide a detailed 3D distribution and space motion of a billion stars in our Galaxy (Gaia Collaboration et al., 2016). During 5 years of mission *Gaia* will deliver positions, parallaxes, and proper motions for all stars down to $G \simeq 20$ over the whole sky. According to the GUMS (*Gaia* Universe Model Snapshot) simulation *Gaia* will see between 250 000 and 500 000 WDs, and more than 60% of them will be in binaries (Carrasco et al., 2014). Astrometrical and multi-colour photometrical observations will be possible for the Galactic WD population. The majority of the Galactic WD population is too faint for the Radial Velocity Spectrometer (RVS) on board of the

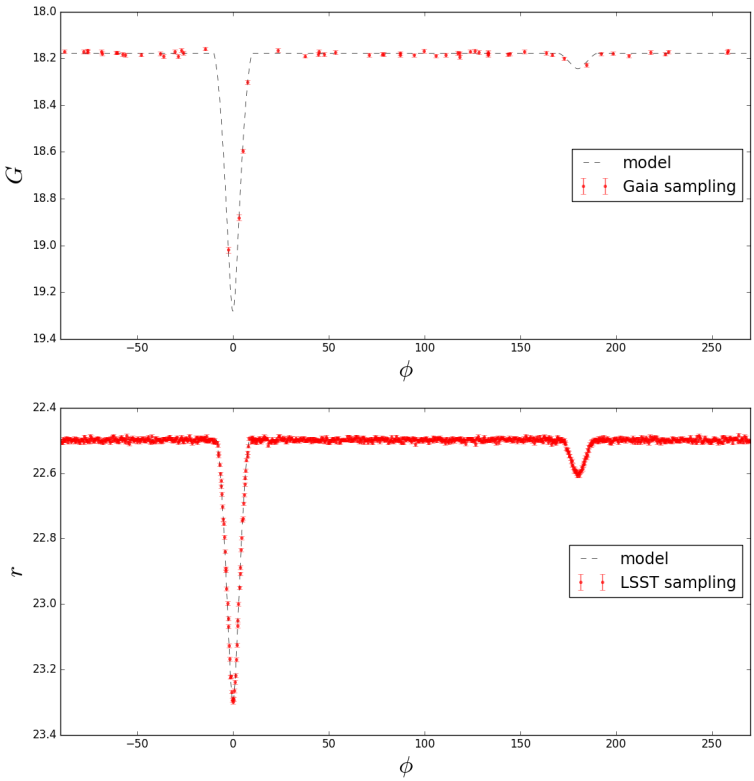

Figure 3.2: An example of phase folded light curves sampled with *Gaia* (top panel) and LSST (bottom panel) observations. The periods of the two sources are $P \simeq 21$ min and $P \simeq 24$ min respectively.

Gaia satellite, and even the brightest ones ($G < 15$) are typically featureless in RVS wavelength range. Thus no radial velocities will be available for these sources, so to fully characterise them ground-based spectroscopic follow-up will be necessary (Carrasco et al., 2014; Gaensicke et al., 2015).

The LSST is a ground-based telescope, currently under construction and expected to be fully operational in 2022 (LSST Science Collaboration et al., 2009). It will complement the *Gaia* study of the Milky Way stellar population down to magnitude $r \simeq 24$, with a possibility to extend this photometric limit down to $r \simeq 27$ with image stacking techniques. The LSST will detect about 10 billion stars up to distances of ~ 100 kpc over half of the sky. In particular, it will allow the discovery of several millions of WDs (LSST Science Collaboration et al., 2009, Chapter 6).

The technical characteristics of the two instruments used for our study (sky coverage, average cadence, limiting magnitude and visibility constraints of the survey, etc.) are summarised in Table 3.2.

3.3.1 Simulations of light curves

Next we simulate the light curves of the obtained DWD model population by using a purely geometrical model. We compute the flux of a binary for given binary param-

eters: a, R_1, R_2, r_1, r_2 and d, where a is the binary orbital separation, R_1 and R_2 are the respective radii of the two binary components, and r_1 and r_2 are their r-band magnitude. Note that in this work we adopt the definition of the primary as the brightest WD, and secondary as the dimmest WD of the pair.

In this simple treatment the limb darkening effect is neglected, so stars are considered spherically symmetric with a uniform surface brightness distribution. Gravitational distortion (ellipsoidal variation) and mutual heating are also not taken into account. Neglecting these effects implies looking for photometric variability caused by eclipses alone, that limits our search to systems with a very narrow range of inclination angles $i \sim 90°$. For DWDs the variation in the light curve induced by mutual heating is not expected to be significant, given the small size of WD stars and roughly equal size binary components. We estimate the maximum flux variation due to the mutual heating to be at most of the same order of magnitude as the average eclipse depth, if we assume the maximum efficiency for this process. To test whether including the ellipsoidal variation in our simulation could enlarge the sample of detectable sources, we estimate how many systems in our simulated population would show the maximum amplitude of the ellipsoidal variation greater than 1% using the theoretical prediction from Morris & Naftilan (1993):

$$\frac{L(\phi)}{L} = \frac{-3(15+u_1)(1+\tau_1)(R_1/a)^3(m_2/m_1)\sin^2 i}{20(3-u_1)}\cos(2\phi), \tag{3.5}$$

where L is the total luminosity of the system, $u_1 = 0.1 - 0.5$ and $\tau_1 = 1.0$ are the limb-darkening and gravity-darkening coefficients for the primary, and $\cos(2\phi) = 1$. We find ~ 20 systems with $G/r < 24$ (in both formation scenarios) with the maximum amplitude of ellipsoidal variation greater than 1% in our simulation. These are the closest and the lightest binaries in our synthetic population as expected from theoretical predictions (e.g. Iben et al., 1998). Thus including ellipsoidal variation in our simulation would increase the number of detected system by at most a couple of tens of systems.

To evaluate the relative photometric error per single *Gaia* observation we use:

$$\sigma_{\rm G} = 1.2 \times 10^{-3}(0.04895z^2 + 1.8633z + 0.00001985)^{1/2}, \tag{3.6}$$

where $z = \max[10^{0.4(12-15)}, 10^{0.4(G-15)}]$ (Gaia Collaboration et al., 2016, Section 8.2). To evaluate the expected photometric error per single observation with the LSST we use

$$\sigma_{\rm r} = (\sigma^2_{\rm sys} + \sigma^2_{\rm rand})^{1/2}, \tag{3.7}$$

where, according to LSST Science Collaboration et al. (2009, Section 3.5), $\sigma_{\rm sys} = 0.005$ is the systematic photometric error, $\sigma^2_{\rm rand} = (0.04 - \tilde{\gamma})x + \tilde{\gamma}x^2$, $x = 10^{(m-m_5)}$ is the random photometric error, m_5 and $\tilde{\gamma}$ are the 5σ limiting magnitude for a given filter and the sky brightness in a given band respectively. Finally, we add a Gaussian white noise to our synthetic light curves.

The motion of the *Gaia* satellite is quite complex and cannot be expressed by an analytical formula: it is given by a combination of rotation of the satellite on its own axis, precession of the spin axis itself, and the revolution around the Sun (Eyer & Mignard, 2005). Therefore, to get a realistic light curve sampling with *Gaia*, we used the *Gaia Observation Forecast Tool*[2], that provides a list of observing times (TCB)

[2]http://gaia.esac.esa.int/gost/

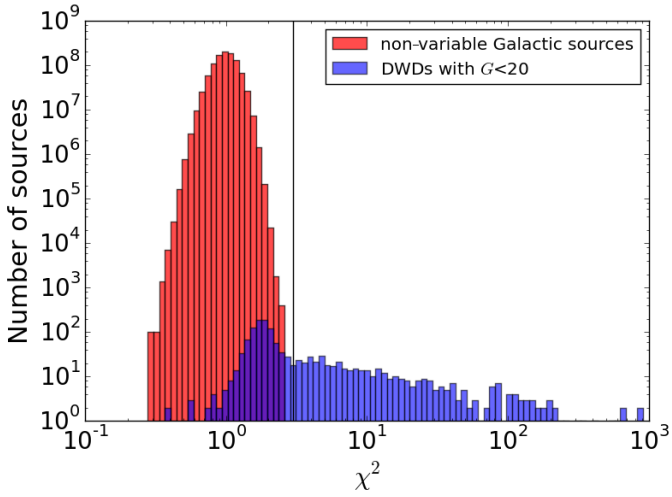

Figure 3.3: The χ^2 distribution of simulated non-variable Galactic objects (in red) obtained using the classic apparent magnitude (G) distribution expected from star-counts (Prob. $\propto 10^{\bar{\gamma}G}$, where $0.2 \leq \bar{\gamma} \leq 0.4$), and the χ^2 distribution of simulated DWDs in Gaia visibility range (in blue). The vertical line represents the threshold value $\chi^2 = 3$, above which we claim a detection.

per target for a given period of observation and target position on the sky. To get a set of *Gaia* pointings for each binary in our simulation we use the largest available time interval that spans from 2014-09-26T00:00:00 TCB to 2019-06-01T00:00:00 TCB ($\sim$ 5 yr mission lifetime). To simulate the light curve sampling with the LSST we use the anticipated regular cadence of 3 days over a nominal ten-year life span of the mission. In Fig. 3.2 we show a comparison of the light curve sampling by *Gaia* (top panel) and LSST (bottom panel) for two binaries with similar orbital periods (21 min and 24 min).

In order to count detections we applied the following criteria. First, we check if the source presents variability by evaluating the χ^2 value of the light curve with respect to the average source magnitude. To establish a χ^2 threshold value above which we consider a source as variable, we compute the χ^2 distribution of non-variable Galactic objects in the Gaia magnitude range. The result is represented in Fig. 3.3. This simple test allows us to distinguish between variability due to a binary nature of the source and variability induced by photometric fluctuations of observations of non-variable objects. In this simulation we do not take into account any other type of variable stars present in the Galaxy such as pulsating WDs (DAVs: ZZ Ceti), Delta Scuti and SX Phoenicis stars, or variability due to deformation or heating in these binaries (see for example Macfarlane et al., 2015; Toma et al., 2016). In real data these stars will exhibit a similar behavior to eclipsing DWDs and will contaminate the sample of candidate DWDs. Thus, in general additional analysis techniques will be required in order to confirm DWD candidates. For the *Gaia* data this analysis will be done by the *Gaia* Data Processing and Analysis Consortium (DPAC, Eyer et al., 2014).

It is evident from Fig. 3.3 that for $\chi^2 > 2$ there is little overlap between the population of non-variable sources (red histogram) and the population of eclipsing

binaries. To be conservative we adopt a threshold value of $\chi^2 = 3$. Finally, we require that a minimum number of data points, $N_{\rm samp}$, with flux at least 3σ below the out-of-eclipse level, falls within the eclipse phase: for Gaia we adopt $N_{\rm samp} \geq 3$ and for the LSST $N_{\rm samp} \geq 10$. This requirement introduces a constrain on the ratio between the duration of the eclipse phase $t_{\rm ecl}$ and the binary orbital period P, such that $t_{\rm ecl}/P = N_{\rm samp}/N_{\rm tot}$, where $N_{\rm tot}$ is the total number of observations per source (see Table 3.2). By using a geometrical argument $t_{\rm ecl}$ can be estimated as the time it takes the occulting star to move twice the distance from the first contact (the point when the apparent stellar disks are externally tangent) to mid-eclipse (when stellar centres are aligned), so $t_{\rm ecl}/P$ can be found as

$$\frac{t_{\rm ecl}}{P} = \frac{\delta}{2\pi a}, \tag{3.8}$$

where $\delta = 2\sqrt{(R_1 + R_2)^2 - a^2 \cos^2 i}$ and $2\pi a$ is the total length of the orbit. Note, that for an edge-on binary $\delta = 2(R_1 + R_2)$. From equation (3.8) we find that the typical $t_{\rm ecl}$ for a DWD binary in our simulated population is around 2 min. Thus, we expect that *Gaia* will detect systems with typical periods $P \lesssim (t_{\rm ecl} N_{\rm tot})/N_{\rm samp} \lesssim 45$ min. Following a similar reasoning one can anticipate that LSST will detect eclipsing binaries with $P \lesssim 3$ h.

3.3.2 Detection efficiency

To assess the detection efficiency of the two instruments we simulate the sampling of a test light curve by varying the magnitude and period of a binary system with $m_1 = 0.53\,{\rm M}_\odot, m_2 = 0.35\,{\rm M}_\odot, R_2 = 0.017\,{\rm R}_\odot, R_1 = 0.8R_2, d = 1\,{\rm kpc}$ and $i = \pi/2$. The chosen parameters for the test light curve represent the average values in our simulated population. For each period P in the range between 5 min and 10 h (with 10 min steps) and magnitude (r or G) between 15 and the photometric limit of the instrument (with 0.25 mag steps) we calculate 100 realisations of the test light curve sampling by randomly assigning the initial orbital phase. We determine whether the light curve was detected based on the criteria described in Sect. 3.3.1. Finally, we represent the detection probability per bin as the number of times the test light curve was detected over 100 realisations.

As discussed in Sect. 3.3.1 our detection test depends on the total number of observations per source $N_{\rm tot}$. For *Gaia* $N_{\rm tot}$ is uniform in ecliptic longitude λ and has a strong dependence on ecliptic latitude β[3]: $N_{\rm tot}$ is minimum at $\beta \sim 0°$, increases up to ~ 200 observations per source at $\beta \pm 45°$, and decreases down to ~ 70 at ecliptic poles $\beta \pm 90°$ (Eyer & Mignard, 2005). *Gaia* detection efficiency for $\beta = 0, +45, +60$ and $90°$ ecliptic latitudes is represented in Fig. 3.4, where the impact of the different number of observations is evident. Figure 3.4 shows that for any fixed period (when the distance to the source is also fixed) *Gaia* generally detects more efficiently brighter binaries, simply because of the photometric performance of the instrument. For example in the top left panel of Fig. 3.4, for periods between 2-3 h one can see that the efficiency drops from 0.4 - 0.3 to 0 for increasing magnitudes. However, for very short periods ($P \lesssim 20$ min) the efficiency remains approximately constant even at the faint end of the *Gaia* visibility range, independently of the number of observations. At a fixed

[3]https://www.cosmos.esa.int/web/gaia/table-2-with-ascii

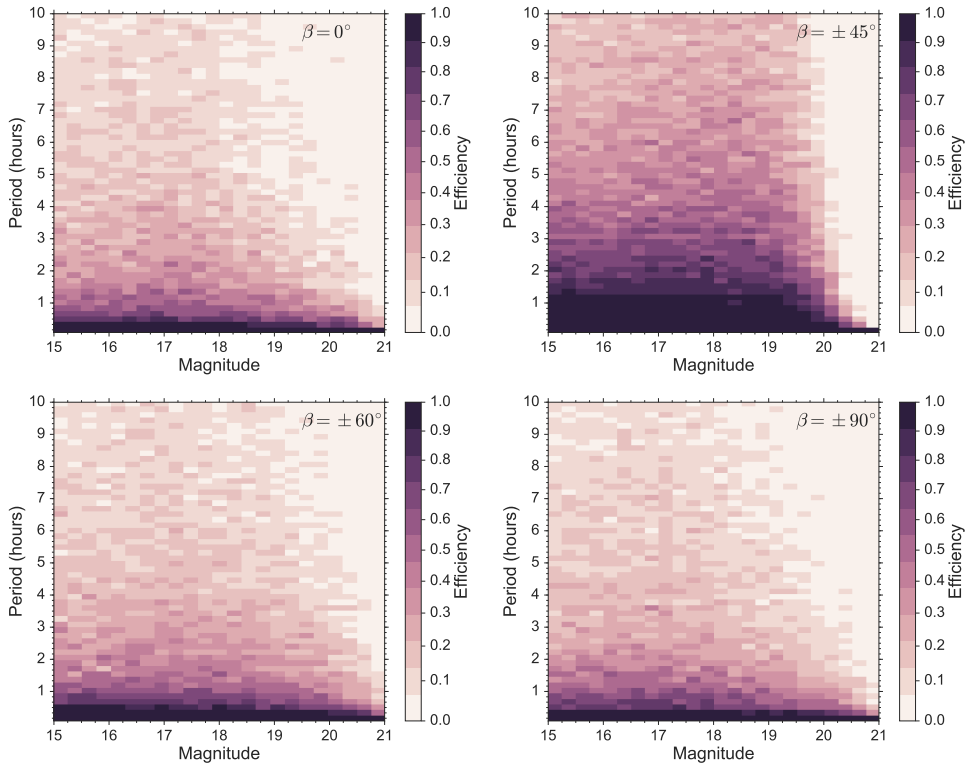

Figure 3.4: Detection efficiency of *Gaia* at $\beta = 0, +45, +60$ and $90°$ ecliptic latitudes, that corresponds to respectively to 60, 200, 80 and 70 observations, computed for test binary system with $m_1 = 0.53\,\mathrm{M}_\odot, m_2 = 0.35\,\mathrm{M}_\odot, R_2 = 0.017\,\mathrm{R}_\odot, R_1 = 0.8R_2, d = 1\,\mathrm{kpc}$ and $i = \pi/2$. The time step is 10 min and the magnitude step is 0.25. The colour indicates the instrument efficiency from 0 to 1.

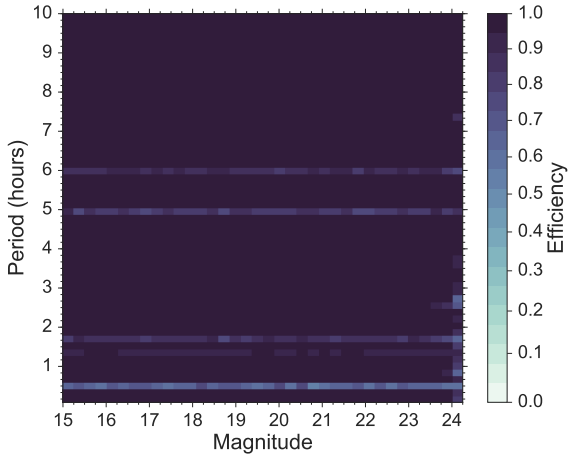

Figure 3.5: Detection efficiency of the LSST computed for test binary system with $m_1 = 0.53\,\mathrm{M}_\odot, m_2 = 0.35\,\mathrm{M}_\odot, R_2 = 0.017\,\mathrm{R}_\odot, R_1 = 0.8R_2, d = 1\,\mathrm{kpc}$ and $i = \pi/2$. The time step is 10 min and the magnitude step is 0.25. The colour indicates the instrument efficiency from 0 to 1.

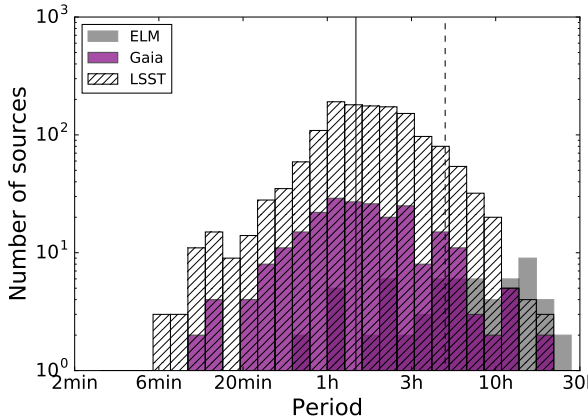

Figure 3.6: Number of detected sources as a function of the orbital period for the $\gamma\alpha$ formation scenario. The purple and hatched histograms represent respectively *Gaia* and LSST detections. The gray histogram shows binaries detected by the ELM survey taken from Gianninas et al. (2015). The black continuous line represents the median of the detected periods in our simulation and dashed line marks the limit of the LISA band.

magnitude *Gaia* cadence works better for detection of short period sources: for $G = 18$ the efficiency is > 0.4 for $P < 4$h and > 0.9 for $P < 30$ min (Fig. 4 top left panel). This is a consequence of the fact that the eclipse duration is set by the geometry of the system, so the time that the system spends in eclipse compared to the total orbital period is longer for systems with shorter periods (i.e., $t_{\rm ecl}/P$ decreases along the y-axis). Thus, it is more likely to catch the binary in eclipse phase when the period of the binary is shorter. By using this simple argument and assuming a regular cadence of 70 observations one can preliminarily estimate the average number of detections by counting the number of DWDs in our synthetic population that satisfy $t_{\rm ecl}/P \geq 3/70$. This gives around 250 DWD systems with $G < 20.7$.

The efficiency of the LSST is illustrated in Fig. 3.5. For the LSST we find that the average cadence of 1 observation in 3 days and the high number of data points make it very efficient at all magnitudes for all orbital periods $\lesssim 10$ h. Drops in efficiency visible in Fig. 3.5 (e.g. a horizontal stripe at 6 h) corresponds to periods that are sub-multiples of 72 h, the cadence of observations. As for *Gaia*, we estimate the number of binaries in our simulated population that can be positively detected with at least 10 observation per eclipse. We find around $\sim 1.9 \times 10^3$ binaries with $r < 24$.

3.3.3 Results

For each binary in our simulated population we compute 100 light curve realisations by randomising over the initial orbital phase. We define the probability of detection as the fraction of times the light curve was positively detected over the total number of light curve realisations. The following results pertain the fraction of the total Galactic DWD population that is: 1) above the photometric limit of the instrument, 2) for assigned orientation to the detector can be seen as eclipsing (i.e such that $\cos i \leq (R_1 + R_2)/a$), and 3) in a sky position covered by the survey. In the reminder we call this population "*Gaia*/LSST input population". Note, that the input population represents the maximum detectable sample for a given survey.

We find that 190 (250) binaries have a non-zero probability[4] to be detected by *Gaia* in the $\alpha\alpha$ ($\gamma\alpha$) scenario in 5 yr mission lifetime. This represents ∼50% of the *Gaia* input population in both formation scenarios. Such detection percentage is due to the sparse *Gaia* sampling, that spread over the 5 yr mission time makes it difficult to detect systems with very narrow eclipses (see Sect. 3.3.2). The average number of detected binaries weighed by the detection probability is 30 for the $\alpha\alpha$ and 50 for the $\gamma\alpha$ CE model respectively. Essentially, *Gaia* will be sensitive to eclipsing binaries with orbital periods less than a few hours (50% of these have periods < 1.6 h, see Fig. 3.6) up to the maximum of a few days. The most distant binary detected by *Gaia* is at $d = 3.5$ kpc. In addition, we find that a possible extension of the *Gaia* mission up to 10 years (Gaia Collaboration et al., 2016, Section 5.3.2) will double the average number of detections compared to the nominal 5 yr mission lifetime. Incidentally, when we use a random sampling of the orbital phase, instead of using detailed *Gaia* cadence, we obtain twice as many detections.

Compared to *Gaia*, the ability of the LSST to see much fainter sources gives an order of magnitude more eclipsing binaries: 1100 (1460) DWDs have a non zero probability of being detected. These detections represent ∼65% of the LSST input popula-

[4] A non-zero probability according to our definition means at least one detection out of 100 (i.e. ≥ 0.01).

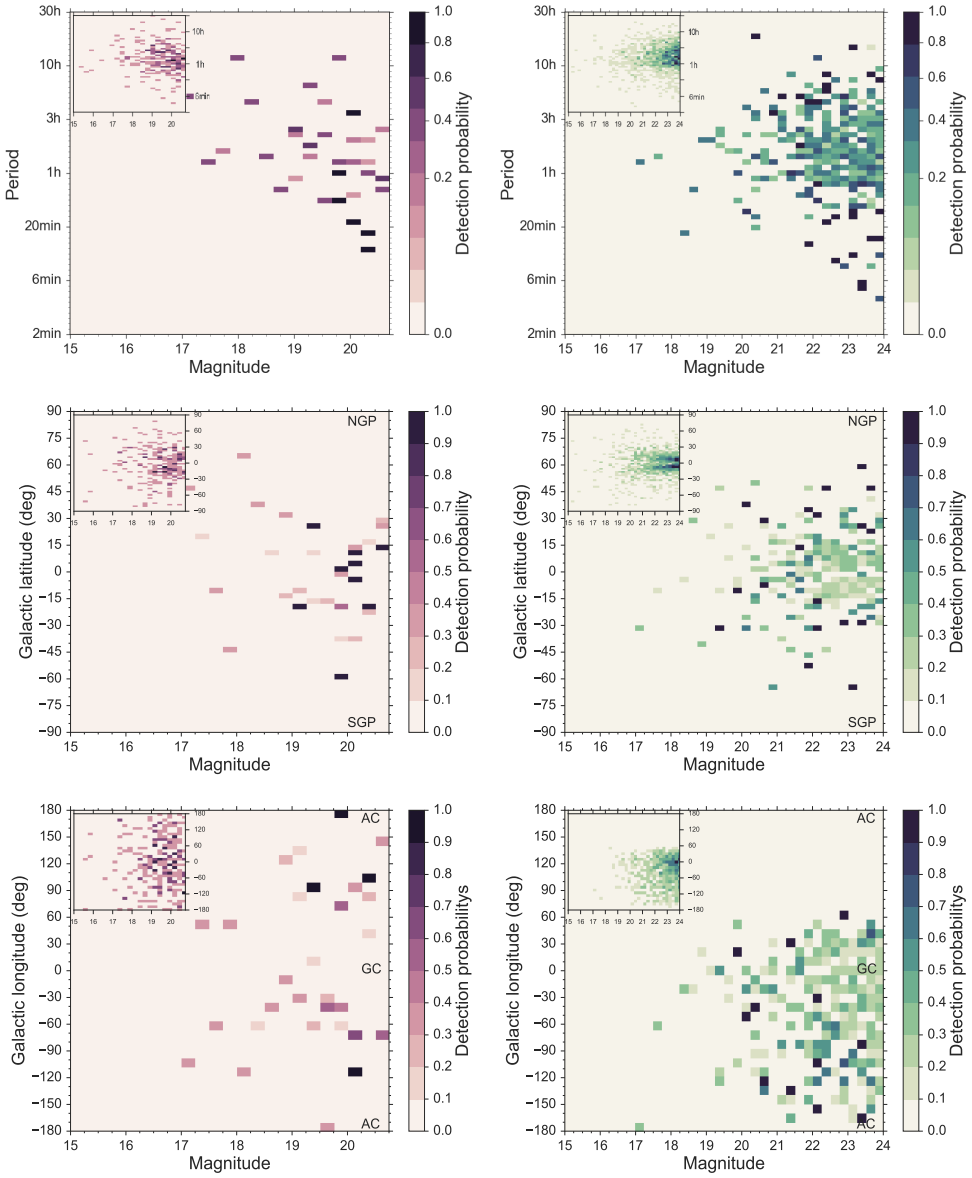

Figure 3.7: Probability diagrams for the number of detections in different 2D parameter spaces: left panels for *Gaia*, right panels for LSST. We show all the systems formed via the $\gamma\alpha$ scenario weighed by the probability of being detected. The respective inserts represent the distribution of all the systems with a non-zero detection probability. The colour indicates the detection probability: purple palette for *Gaia* and green palette for LSST. NGP ans SGP indicate the North and the South Galactic poles, GC and AC indicate Galactic centre and Galactic anti-centre.

tion (for both formation scenarios). The average number of detected binaries weighed by the probability for the LSST is 850 (1167) DWDs for the $\alpha\alpha$ ($\gamma\alpha$) scenario. The maximum distance in the LSST detected sample is $\sim$ 10 kpc.

Notably, half of the population detected by both instruments has periods shorter than 1.5 h as shown in Fig. 3.6 This substantial subsample has orbital frequencies, $f = 1/P$, larger than 0.1 mHz, and thus is potentially detectable through GW radiation in the LISA band (see Sect. 4). Both *Gaia* and LSST will enlarge the number of very short period binaries, as the mean period of *Gaia* and LSST detections peaks around 1.5 h, while the mean period of the ELM binaries is 7.4 h (Gianninas et al., 2015).

In Fig. 3.7 we show the distribution of DWDs weighed by the detection probability in different 2D parameter spaces: the magnitude-period distribution[5] (top panels), magnitude-Galactic latitude (middle panels) and longitude (bottom panels) distributions, where colours trace the detection probability. The inserts in Fig. 3.7 represent the respective distributions of all sources with non-zero probability of detection. Despite the fact that *Gaia* is more efficient at brighter magnitudes (Fig. 3.4), one can see that the majority of the detected population is faint ($G < 18$) and has periods less than a few hours ($P < 3$ h). The former result reflects the magnitude distribution of the input population that peaks around the faint end of the *Gaia* visibility range, the later is a consequence of our detection criterion as discussed in Sect. 3.3.1. Comparing the two upper panels in Fig. 3.7 it is evident that the LSST with its deeper photometric limit, has access to a much larger fraction of the total population. In particular, while *Gaia* operates in the same magnitude range of the ELM ground-based optical survey, the LSST will extend the sample of known DWDs to lower magnitudes. However, the follow-up spectroscopy of such a faint sources will be a challenge even for up-coming facilities.

In the middle and lower panels of Fig. 3.7, we represent the spatial distribution of *Gaia* and LSST detections. Because of its photometric limit, *Gaia* will see only the closest sources ($d_{\max} = 3.5$ kpc $\ll$ radius of Galactic disc), therefore the distribution in longitude is featureless. On the other hand, one can start to see the distribution of DWD around the Galactic plane (insert middle left panel), since 3.5 kpc is comparable with the vertical extension of the Galactic disc. The distribution of DWDs in the Galaxy will become potentially visible with the LSST. The concentration of detected binaries towards the Galactic plane represent the Bulge of the Galaxy with its characteristic gap around 0° Galactic latitude due to extinction in the disc (insert middle right panel). The location of the LSST in the southern hemisphere is reflected in the lack of sources for Galactic longitudes greater than 60° in Fig. 3.7 (bottom right panel).

In Fig. 3.8 we show the fractions of *Gaia* (purple histogram) and LSST (hatched histogram) detections formed via the $\gamma\alpha$ scenario as a function of orbital period, magnitude and binary mass fraction $q = m_1/m_2$. These fractions are defined as a number of detected sources over the number of binaries of the input population per bin. For both instruments the fraction of detections drops for increasing orbital periods (top panel). Note however, that the fraction of long period binaries ($P > 24$ h) is higher for *Gaia* (> 0.2), due to a non-uniform sampling of the light curves. The middle panel reflects the average detection fraction of the instruments, with no clear

[5]Note, that we show only a part of the magnitude-period parameter space, where the majority of the detected population is located, while the whole range of detected periods extends up to a few days for both instruments, where the detections are sparsely distributed.

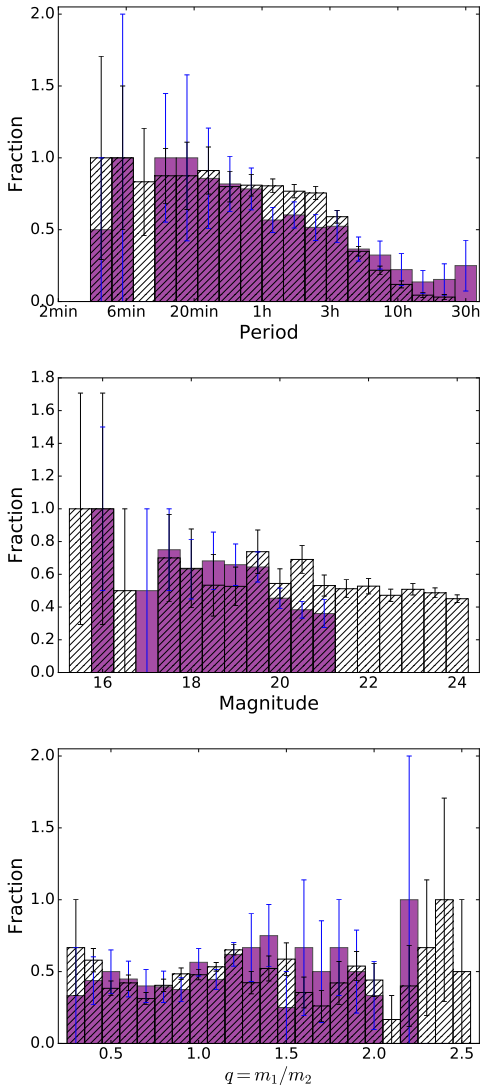

Figure 3.8: Fraction of detected sources over the total input binaries per bin for the $\gamma\alpha$ formation scenario. From top to bottom we show the detection fraction as a function of period, magnitude and mass fraction q. The purple histogram shows *Gaia* detections and hatched histogram represents LSST detections. The error bars (in blue for *Gaia* and in black for the LSST) represent Poissonian errors.

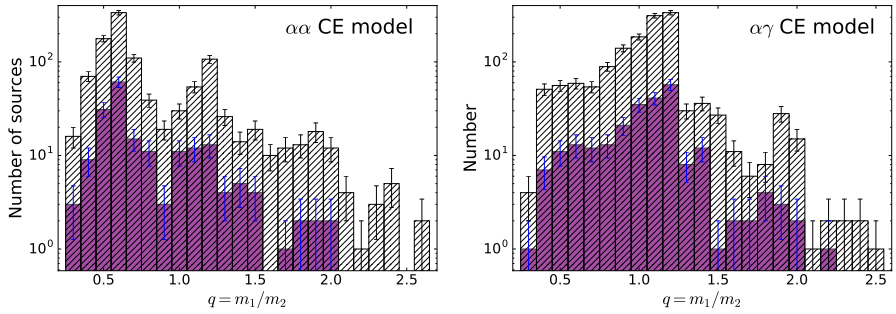

Figure 3.9: Number of detected sources as a function of binary mass ratio $q = m_1/m_2$ for the two different CE scenarios. The error bars represent Poissonian errors.The colour coding is the same as Fig. 3.8.

preference in magnitude. Both instruments detect high fraction of binaries with $q > 1$ (bottom panel), i.e. systems with more massive primaries. By definition the primary is the brightest WD (and consequently the biggest) of the pair, so a wider range of inclination angles is allowed for these systems in order to be detected as eclipsing sources, and thus they are more likely to be detected. In our simulation these systems are typically formed via stable mass transfer. However, taking into account the size of the error bars, the distribution looks consistent with a flat distribution.

Figure 3.9 illustrates the number of detected sources as a function of the mass ratio: left panel for the $\alpha\alpha$ and right panel for the $\gamma\alpha$ CE model. The two distributions are different: the population formed by the $\alpha\alpha$ model shows a prominent peak around $q \sim 0.5$, while the population formed with $\gamma\alpha$ peaks at $q \sim 1$. Despite the $\gamma\alpha$ CE prescription being designed to match the observed DWD binaries (Nelemans et al., 2000; Nelemans & Tout, 2005), the number of currently known sources is too low to prefer it with respect to the $\alpha\alpha$ CE model. Figure 3.9 shows that the *Gaia* sample has the potential to shed light on the nature of the CE phase and physical process that triggers it in DWD progenitor systems, as one can already see the difference between the two models by comparing the purple histograms.

In Fig. 3.10 we illustrate some of the properties of *Gaia* and LSST detections formed by the $\gamma\alpha$ scenario in different 2D parameter spaces where each source is weighed by the detection probability; the inserts represent the respective distributions of the sources with a non-zero probability of being detected. The detected population will consist of binaries with secondaries typically more massive than primaries. The majority of known DWDs were discovered by ELM survey, designed to search for extremely low mass primaries, thus new eclipsing binaries detected by *Gaia* and LSST will extend this parameter space to binaries with more massive primaries. Note, that LSST has potential to detect systems with $m_1 + m_2 >$ Chandrasekhar mass limit, providing some SN Ia progenitor candidates. Moreover, the detected population will have primaries hotter than secondaries, therefore it will be difficult to determine directly the properties of the secondaries. For completeness in the bottom panels of Fig. 3.10 we represent the distribution of the detected sources in period-temperature and temperature-magnitude space, useful for planning of the spectroscopic follow-up of these sources.

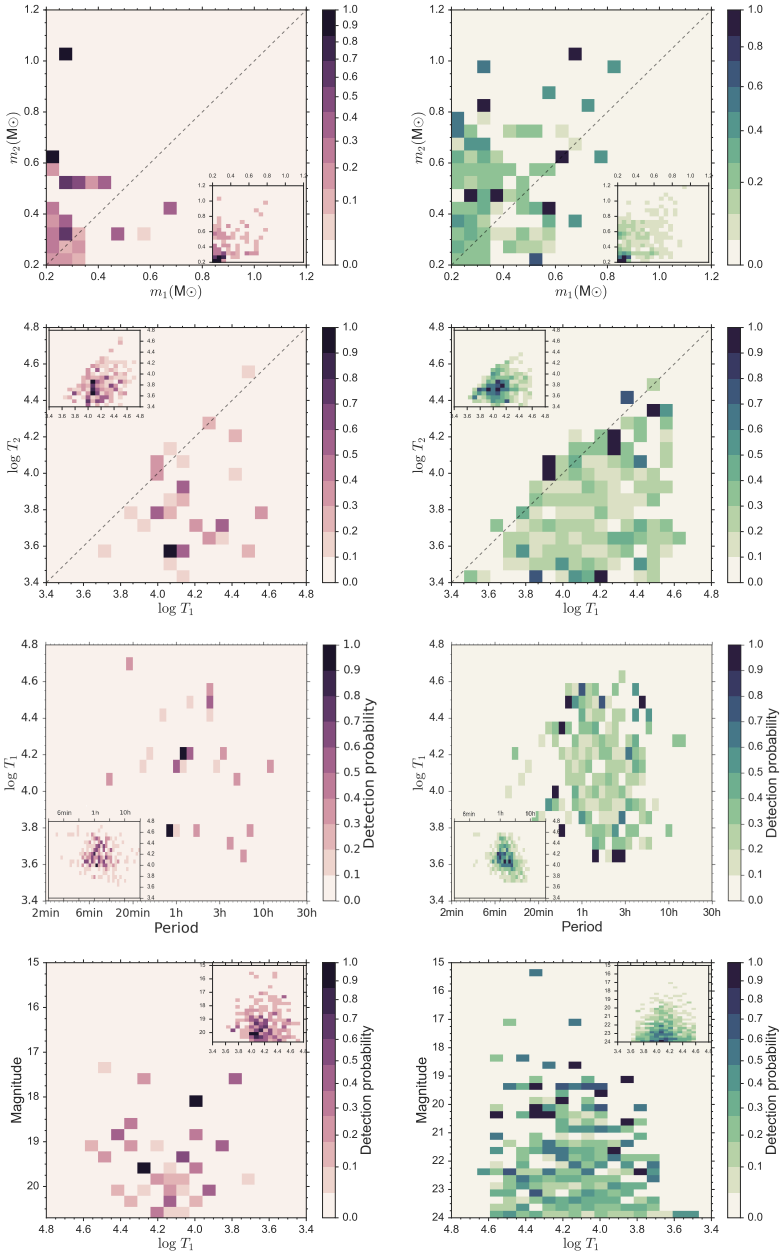

Figure 3.10: Probability diagrams for the number of *Gaia* and LSST detections as a function of binary parameters. We show all the systems formed via the $\gamma\alpha$ scenario weighed by the probability of being detected. The respective inserts represent the distribution of all the systems with a non-zero detection probability. The colour indicates the number of detected sources: purple palette for *Gaia* and green palette for the LSST. The black dashed lines in the upper panels represent the line of equal mass and equal temperature.

3.4 GW detection

In this section we focus our attention on DWDs as GW sources. First, we recall some basic formulae for the estimation of the GW signal. To simulate the LISA instrument response, in this paper we adopt the frequency based method of Cornish & Larson (2003, see also Cornish & Rubbo 2003; Cutler 1998). Then, we estimate the signal-to-noise ratio (SNR) of currently observed DWD binaries to verify our procedure. The following step is to calculate the SNR for all synthetic binaries to identify those with the highest SNR. Finally, we compare our result with previous works (Nelemans et al., 2004; Nissanke et al., 2012; Ruiter et al., 2010), based on a different Galactic model populations.

LISA is a space-based gravitational wave interferometer, conceived as a set of three spacecrafts in an equilateral triangle constellation of a few million km per side. Such spacecraft separation sets the sensitivity range of the instrument from about 0.1 to 100 mHz and will allow the detection of Galactic and extra-Galactic sources, among which thousands will be DWD binaries (Amaro-Seoane et al., 2017). The detector's centre-of-mass will follow a circular heliocentric trajectory, trailing 22° behind the Earth and maintaining a 60° inclination between the plane of the detector and the ecliptic plane. As the reference LISA configuration in this work we adopt the LISA Mission Concept recently submitted as a response to the ESA call for L3 missions (hereafter ESACall v1.1). The ESACall v1.1 is a three-arm configuration[6] with 2.5×10^6 km arm length instead of 5×10^6 km arm length as in the original LISA project (see, e.g., Prince et al., 2007). The sensitivity of the ESACall v1.1 configuration, is based on the latest results from the LISA Pathfinder mission (Armano et al., 2016), a precursor mission designed to test the technologies needed for the laser interferometry in space. It is represented in Fig. 3.11 (Amaro-Seoane et al., 2017).

As pointed out by several authors, at frequencies below a few mHz the expected number of Galactic binaries per frequency bin ($\Delta f = 1/T_{\rm obs}$, where $T_{\rm obs}$ is the total observation time) is so large that these binaries will form an unresolvable foreground signal in the detector (e.g., Amaro-Seoane et al., 2012; Prince et al., 2007; Ruiter et al., 2010). Figure 3.11 illustrates the foreground level from Galactic binaries and its evolution with time from 0.5 to 10 yr of observation computed by using our model population (Amaro-Seoane et al., 2017).

3.4.1 GW signal from DWDs

The great majority of Galactic DWD binaries can be well described using Newtonian dynamics of circular orbits, under the assumption that the binary can be represented by two point masses in orbit (e.g., van den Broek et al., 2012). The gravitational waves they produce can be computed using the quadrupole approximation (see, e.g., Landau & Lifshitz, 1971; Peters & Mathews, 1963). Considering that the timescale on which DWDs typically evolve ($>$ Myr) is much greater than the lifetime of the LISA mission ($\sim$ yr), they can be treated as monochromatic sources emitting at the frequency $f_{\rm s} = 2/P$. In this approximation the GW signal emitted by a binary is given

[6]Note that each arm corresponds to two laser links between spacecrafts, so that a three-arm detector consists of six links in total.

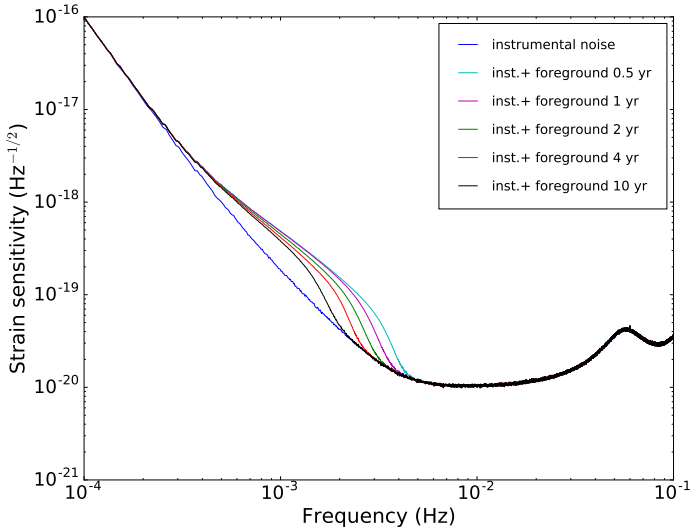

Figure 3.11: LISA ESACall v1.1 sky-averaged sensitivity due to the instrumental noise only and due to the instrumental noise plus Galactic foreground from DWD binaries after 6 mouths, 1, 2, 4 and 10 years of observations (Amaro-Seoane et al., 2017).

by a combination of the two polarisations:

$$h_+(t) = \frac{2(G\mathcal{M})^{5/3}(\pi f_\mathrm{s})^{2/3}}{c^4 d}(1+\cos^2 i)\cos 2\Phi(t), \tag{3.9}$$

$$h_\times(t) = -\frac{4(G\mathcal{M})^{5/3}(\pi f_\mathrm{s})^{2/3}}{c^4 d}\cos i \sin 2\Phi(t), \tag{3.10}$$

where $\mathcal{M} = (m_1 m_2)^{3/5}(m_1+m_2)^{-1/5}$ is the chirp mass of the system and $\Phi(t) = \Phi_0 + \pi f_\mathrm{s} t$ is the orbital phase. In the low frequency limit ($f_\mathrm{s} \ll c/2\pi L \sim 20$ mHz, where $L = 2.5$ Mkm is the detector's arm length) the GW signal as measured by the detector can be expressed as

$$h(t) = F_+ h_+(t) + F_\times h_\times(t), \tag{3.11}$$

where F_+ and $F_\times$ are the detector pattern functions, that encode the detector's response and depend on the source location in the sky and orientation with respect to the detector (see equations (9)-(11) of Cornish & Larson, 2003, for specific expression of these functions). For a monochromatic periodic source the signal-to-noise ratio (SNR) can be written as (Maggiore, 2008, Equation (7.129)):

$$\left(\frac{S}{N}\right)^2 = 4\int_0^\infty df \frac{|\tilde{h}(f)^2|}{S_\mathrm{n}(f)} = \frac{\mathcal{A}^2 T_\mathrm{obs}}{S_\mathrm{n}(f_\mathrm{s})}, \tag{3.12}$$

where $\tilde{h}(f)$ is the Fourier transform of $h(t)$, $S_n(f_\mathrm{s})$ is the noise spectral density of the instrument at f_s (Fig. 3.11) and

$$\mathcal{A} = \left[h_+^2 F_+^2(t) + h_\times^2 F_\times^2(t)\right]^{1/2}. \tag{3.13}$$

Note that in equation (12) we substitute the orbit averaged value of $\mathcal{A}$ computed following equations(42)-(44) of Cornish & Larson (2003).

Table 3.4.1 shows the sample of currently known DWD and AM CVn systems with expected SNR in GWs > 0.01, evaluated by using equation (3.12) for the LISA ESACall v1.1 configuration sensitivity and 1 yr observation time. To roughly estimate SNR values for $T_{\rm obs} = N$yr one can simply rescale the last column by $\sqrt{N}$.

3.4.2 Results

To test our method we consider the sample of the so-called verification binaries. These are well known ultra-compact binaries (mostly detached DWDs and AM CVns), that are expected to be bright in the LISA band. Consequently, they represent guaranteed sources for the mission. Some of these binaries will be detected in a short period after the beginning of the mission ($\sim$ few months), and thus can be used to verify the performance of the instrument (e.g. Stroeer & Vecchio, 2006). Binary parameters and SNR values for 1 yr mission lifetime of the LISA verification binaries are reported in Table 3.4.1. We find 8 of the 57 verification binaries with SNR > 7 within the first year of observation, and 10 within the nominal mission life time of 4 years. These results are in agreement with the full time domain LISA simulation (A. Petiteau private communication, see also Amaro-Seoane et al., 2017). Figure 3.12 illustrates how the SNR grows progressively with mission duration.

We compute the total number of resolved binaries in our model population. Parameters that are not provided directly by our population synthesis code (e.g. the polarisation angle and the initial orbital phase) are randomised assuming uniform distribution over the interval of their definition. The result for the two formation scenarios and different mission durations are reported in Table 3.4.2. The numbers of individually resolved DWDs for the LISA ESACallv1.1 configuration with SNR > 7 are $\sim 10 - 11 \times 10^3$ for 1 year and $24.5 - 25.8 \times 10^3$ for 4 year of mission. These results are compatible with those obtained by the Gravitational Observatory Advisory Team (GOAT)[7], Shah et al. (2012) and Nissanke et al. (2012), based on Galactic population from Nelemans et al. (2004), and with Ruiter et al. (2010), based on a different population synthesis code, when considering different mission lifetime, detector geometry and SNR threshold.

In Fig. 3.13 we show some of the properties of LISA detections predicted by the $\gamma\alpha$ CE model. From comparison between Fig. 3.7 and Fig. 3.13 it is evident that LISA will see binaries that are non accessible to EM detectors, virtually down to magnitude 70. LISA detections will have periods ranging between 2 min and 2h, and chirp masses up to 1 $M_\odot$. Remarkably, unaffected by extinction LISA will see binaries throughout the Galaxy up to distances comparable with the extension of the Galactic disc. Figure 13 shows that the most of the detections comes from Galactic bulge (i.e. at Galactocentric distance close to 0). (Fig. 3.13 bottom panels). In particular, LISA will detect DWDs even beyond the Galactic centre, that is impossible with optical facilities.

[7] http://sci.esa.int/jump.cfm?oid=57910

Table 3.3: A sample of known interacting (AM CVn stars) and non interacting (detached DWDs) LISA verification binaries. Amplitudes are given in units of 10^{-23}. To compute the SNR for each binary we set the initial orbital phase and polarisation angle to 0°, and the inclination to 60° for cases where it is unknown.

Name	l(deg)	b(deg)	P(s)	m_1(M⊙)	m_2(M⊙)	d(pc)	i(deg)	$f_{\rm GW}$(mHz)	$\mathcal{A}$	SNR
RX J0806[a]	206.93	23.4	321.52911	0.55	0.27	5000.0	37.0	6.22	6.43	108.82
V407 Vul [a]	57.73	6.44	569.395	0.6	0.07	2000.0	60.0	3.51	3.32	20.98
ES Cet[a]	168.97	-65.86	621.0	0.6	0.06	1000.0	60.0	3.22	5.4	23.72
AM CVn[a]	140.23	78.94	1028.73	0.71	0.13	600.0	43.0	1.94	15.22	17.03
SDSS J1908+3940[a]	70.66	13.93	1092.0	0.6	0.05	1000.0	60.0	1.83	3.11	2.34
HP Lib[a]	352.06	32.55	1103.0	0.57	0.06	200.0	30.0	1.81	17.77	19.7
PTF1J1919+4815[a]	79.59	15.59	1350.0	0.6	0.04	2000.0	60.0	1.48	1.08	0.56
CR Boo[a]	340.96	66.49	1471.0	0.79	0.06	340.0	30.0	1.36	10.82	7.47
KL Dra[a]	91.01	19.2	1500.0	0.6	0.02	1000.0	60.0	1.33	1.02	0.44
V803 Cen[a]	309.37	20.73	1596.0	0.84	0.08	350.0	14.0	1.25	13.75	9.08
SDSS J0926[a]	187.51	46.01	1699.0	0.85	0.04	460.0	83.0	1.18	5.13	1.03
CP Eri[a]	191.7	-52.91	1701.0	0.6	0.02	700.0	60.0	1.18	1.34	0.45
2003aw[a]	235.13	26.48	2028.0	0.6	0.02	700.0	60.0	0.99	1.19	0.3
2QZ 1427 -01[a]	345.67	37.17	2194.0	0.6	0.015	700.0	60.0	0.91	0.85	0.19
SDSS J1240[a]	297.57	60.77	2242.0	0.6	0.01	400.0	60.0	0.89	0.98	0.23
SDSS J0804 [a]	205.94	23.37	2670.0	0.6	0.01	400.0	60.0	0.75	0.87	0.15
SDSS J1411[a]	91.89	63.82	2760.0	0.6	0.01	400.0	60.0	0.72	0.85	0.14
GP Com[a]	323.55	80.3	2794.0	0.6	0.01	80.0	60.0	0.72	4.24	0.7
SDSS J0902[a]	184.42	41.32	2899.0	0.6	0.01	500.0	60.0	0.69	0.66	0.1
SDSS J1552[a]	51.31	50.53	3376.3	0.6	0.01	500.0	60.0	0.59	0.6	0.07
CE 315[a]	309.26	39.25	3906.0	0.6	0.006	77.0	60.0	0.51	2.12	0.19
J0651+2844[a]	186.93	12.69	765.4	0.55	0.25	1000.0	86.9	2.61	16.84	19.67
J0923+3028[a]	195.82	44.78	3884.0	0.279	0.37	228.0	60.0	0.51	20.13	1.73
WD 0957-666[a]	287.14	-9.46	5296.81	0.32	0.37	135.0	68.0	0.38	31.07	1.27
J0755+4906[a]	169.76	30.42	5445.0	0.176	0.81	2620.0	60.0	0.37	1.68	0.08
J0849+0445[a]	222.7	28.27	6800.0	0.176	0.65	1004.0	60.0	0.29	3.22	0.09
J0022-1014[a]	99.2997	-71.7538	6902.496	0.21	0.375	1151.0	60.0	0.29	2.15	0.06
J2119-0018[a]	51.58	-32.54	7497.0	0.74	0.158	2610.0	60.0	0.27	1.15	0.02
J1234-0228[a]	294.25	60.11	7900.0	0.09	0.23	716.0	60.0	0.25	1.01	0.02
WD 1101+364[a]	184.48	65.62	12503.0	0.36	0.31	97.0	25.0	0.16	23.22	0.19
WD 0931+444[b]	176.08	47.38	1200.0	0.32	0.14	660.0	70.0	1.67	7.41	3.58
WD 1242-105[c]	300.31	51.98	10260.0	0.56	0.39	39.0	45.1	0.19	114.75	1.41
J0056-0611[d]	126.6604	-69.0278	3748.0	0.174	0.46	585.0	60.0	0.53	6.28	0.63
J0106-1000[d]	135.7244	-72.4861	2345.76	0.191	0.39	2691.0	60.0	0.85	1.79	0.39
J0112+1835[d]	129.77	-44.0119	12699.072	0.62	0.16	662.0	60.0	0.16	2.84	0.01
J0345+1748[d]	171.051	-28.4018	20306.592	0.76	0.181	166.0	60.0	0.1	10.81	0.01
J0745+1949[d]	200.4746	20.4396	9711.36	0.1	0.156	270.0	60.0	0.21	1.9	0.02
J0751-0141[d]	221.4565	12.5761	6912.864	0.97	0.194	1859.0	60.0	0.29	2.52	0.07
J0825+1152[d]	212.5705	26.1227	5027.616	0.49	0.287	1769.0	60.0	0.4	2.8	0.14
J1053+5200[d]	156.4021	56.794	3677.184	0.26	0.213	1204.0	60.0	0.54	2.36	0.23
J1054-2121[d]	269.7458	33.8695	9019.296	0.39	0.168	751.0	60.0	0.22	2.33	0.03
J1056+6536[d]	140.067	47.5033	3759.264	0.34	0.338	1421.0	60.0	0.53	3.62	0.35
J1108+1512[d]	234.1026	63.2376	10635.84	0.42	0.167	698.0	60.0	0.19	2.36	0.02
J1112+1117[d]	242.321	61.8382	14902.272	0.14	0.169	257.0	60.0	0.13	2.14	0.01
J1130+3855[d]	172.9043	69.3762	13523.328	0.72	0.286	662.0	60.0	0.15	5.2	0.02
J1436+5010[d]	89.0112	59.4607	3957.12	0.46	0.233	830.0	60.0	0.51	5.55	0.48
J1443+1509[d]	14.0206	61.3102	16461.792	0.84	0.181	540.0	60.0	0.12	4.11	0.01
J1630+4233[d]	67.076	43.3603	2389.824	0.3	0.307	820.0	60.0	0.84	7.06	1.45
J1741+6526[d]	95.1544	31.7085	5279.904	1.11	0.17	936.0	60.0	0.38	5.82	0.28
J1840+6423[d]	94.3694	25.424	16528.32	0.65	0.177	676.0	60.0	0.12	2.66	0.01
J2338-2052[d]	49.5602	-72.1995	6604.416	0.15	0.263	1295.0	60.0	0.3	1.11	0.03
CSS 41177[e]	210.129	52.424	8208.0	0.36	0.31	473.0	88.9	0.24	6.3	0.06
J1152+0248[f]	270.23	61.86	8602.0	0.47	0.41	464.0	89.2	0.23	9.82	0.1

[a] http://www.astro.ru.nl/ nelemans/dokuwiki/doku.php?id=verification_binaries:intro, [b] Kilic et al. (2014);
[c] Debes et al. (2015); [d] Gianninas et al. (2015); [e] Bours et al. (2014); [f] Hallakoun et al. (2016).

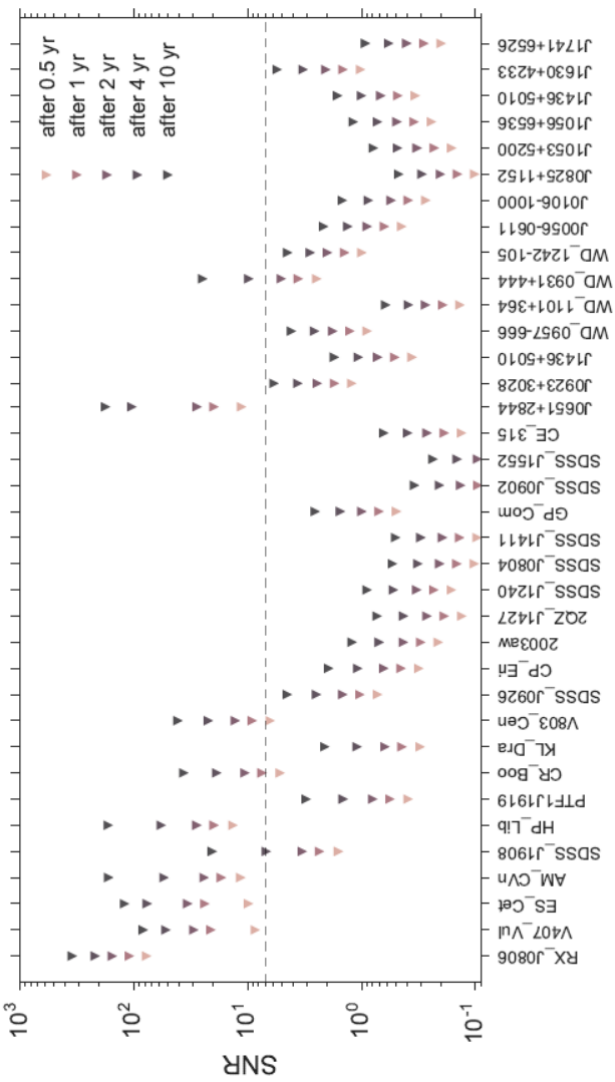

Figure 3.12: SNR evolution with time for a sample of LISA verification binaries. The dashed horizontal line corresponds to SNR = 7.

Table 3.4: Total number of individually resolved DWDs with SNR $>$ 7 for the LISA ESACallv1.1 mission configuration.

CE model	6 m	1 yr	2 yr	4 yr	10 yr
$\alpha\alpha$	6185	9808	16360	24482	44349
$\gamma\alpha$	7125	11385	18330	25754	52045

3.5 The combined EM & GW sample

In the two previous sections we showed that the expected number of DWD detections through EM and GW radiation within next two decades is significant. So far GW studies focused on currently known Galactic binaries or on the future EM follow up of these sources, ignoring the fact that revolutionary optical surveys such as *Gaia* and the LSST will be available between now and the LISA launch. In this section we want to estimate how many DWDs detected by Gaia and LSST will be bright enough in GWs to be detected by the LISA.

Starting from the *Gaia* and LSST samples (Sect. 3.1) we compute the SNR for the LISA ESACallv1.1 configuration and 4 yr mission lifetime, and we select those with SNR $>$ 7 (see Table 3.5). We find 13 and 25 combined *Gaia* and LISA detections respectively for the $\alpha\alpha$ and $\gamma\alpha$ CE models. Combined LSST and LISA samples are 3-4 times bigger: 50 in the $\alpha\alpha$ formation scenario and 73 for in $\gamma\alpha$ scenario. This result shows that before the LISA launch we will have at least twice as many guaranteed LISA detections with SNR$>$ 7. The period of the combined detections will range from a few minutes to 1 hour, and will be on average (as for currently known LISA verification binaries) around 15 min (see Fig. 3.14). As for the sample of known verification binaries (Table 3.4.1), the mass of the primary, secondary, and, consequently the chirp mass of these binaries is not expected to exceed 1 $M_{\odot}$. Verification binaries provided by *Gaia* are not expected to be found at distances larger than the already known ones, while the LSST will double the maximum distance because of its deeper photometric limit (Fig. 3.14).

Several authors have already pointed out that for those sources that could be detected in both EM and GW waves much more information can be gained compare to either EM or GW can provide alone (see, e.g., Marsh, 2011; Shah et al., 2012; Shah & Nelemans, 2014). Light curves allow the measurement of the orbital period, the inclination angle and the scaled radii of the binary components (R_1/a and R_2/a), that, in turn, can be used to determine the binary mass ratio from the mass-radius relationship. This information combined with the chirp mass determined from the GW data, in principle, permits the estimation of the individual binary component masses. For monochromatic sources, like the majority of DWD binaries, GW data will provide the measurement of the chirp mass in combination with distance (see the dependence on $\mathcal{M}$ and d in equations (3.9)-(3.10)). Thus, parallax measurements by *Gaia* and LSST will be crucial to determine the distances and to break this degeneracy. The measure of the binary frequency evolution ($\dot{f}$, that is not likely from GW data for all DWDs) can be equivalently determined from eclipse timing (Shah & Nelemans, 2014). Furthermore, EM observations can be also used to constrain GW observables and to improve their accuracy. In fact, there are several correlations between the GW and EM observable quantities, e.g. between GW amplitude and binary inclination, ecliptic

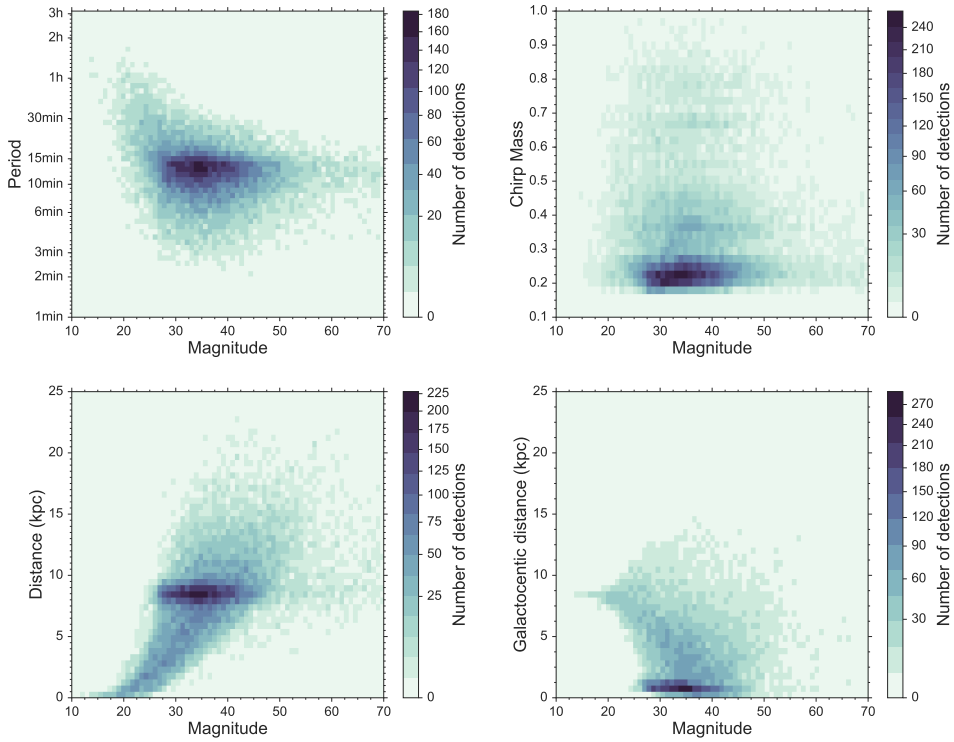

Figure 3.13: 2D histograms of the number of LISA detections with SNR > 7. The colour indicates the number of detected sources.

Table 3.5: Summary table for the number of detections with *Gaia*, LSST and LISA. We reported results for the nominal mission life time of 5 yr for *Gaia*, 10 yr for the LSST and 4 yr for LISA.

	Gaia	LSST	LISA
(a) $\alpha\alpha$ CE model			
Gaia	189	93	13
LSST	93	1100	50
LISA	13	50	24508
(b) $\gamma\alpha$ CE model			
Gaia	246	155	25
LSST	155	1457	73
LISA	25	73	25735

latitude and longitude. For example, an a priori knowledge of the source sky position and inclination can give an improvement on the measurement of GW amplitude up to a factor of 60 (Shah et al., 2013). Vice versa, Shah et al. (2012) showed that small inclination errors from GW data imply that system is eclipsing, consequently this fact can be used for the EM detection of new eclipsing sources.

3.6 Discussion and Conclusions

In this work we have computed the expected number of DWD detections by *Gaia* and the LSST as eclipsing sources, and by the future LISA mission as GW sources. As in earlier studies we relied on population synthesis modelling because of the small number of the known systems. To simulate the Galactic population of DWD binaries we considered two different prescriptions for the CE phase ($\alpha\alpha$ and $\gamma\alpha$) in order to investigate whether *Gaia*, LSST and LISA will elucidate on the nature of the CE phase. We find that *Gaia* can provide up to a few hundred of eclipsing detached DWDs, while LSST will extend this sample up to almost 2×10^3 sources. Then we investigated the number of individually resolvable GW sources considering the latest mission concept of the LISA detector submitted as a response to the ESA call for L3 missions in 2017. We find that the number of detectable detached DWDs is 25×10^3 for the nominal 4 years of mission life time. Finally, we used the obtained EM samples to estimate how many verification binaries *Gaia* and LSST will provide before the LISA launch. We find several tens of combined EM and GW detection. These detections will significantly increase the sample of know LISA verification binaries by at least factor of 2.

To investigate the sensitivity of our results to assumptions on the initial stellar population, we performed a set of simulations with two different IMFs and with a different mass ratio distribution. We find that the same star formation history but a different choice for the IMF, influences mostly the total number of generated DWDs and has a relatively moderate impact on the number of detections. For example, the Miller & Scalo (1979) and the Scalo (1986) IMF, that are steeper than the Kroupa IMF for $M > 1$ M$\odot$, produce respectively $\sim 10\%$ more DWD systems, that translates directly in 10% more detections by *Gaia*, LSST and LISA. On the other hand, the assumption on the mass ratio distribution proves to have a non-negligible impact on

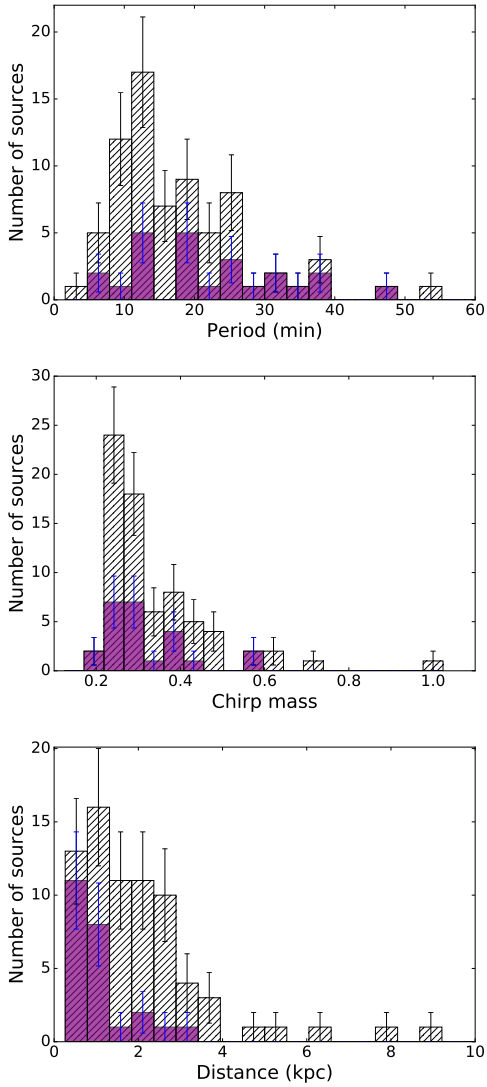

Figure 3.14: Number of combined EM and GW detections as a function of the chirp mass, binary orbital period and distance from the Sun. The purple histogram represents *Gaia* - LISA and hatched histogram represents LSST - LISA combined detections. The error bars represent Poissonian errors.

our results. In general, a power law $f(q) \propto q^b$ can be used to describe this distribution, where b depends on the stellar population. For intermediate mass stars the value of b ranges between 0 and -1 (Duchêne & Kraus, 2013). Thus, in addition to our previous simulation (in which we used $b = 0$), we performed a simulation with $b = -1$ to compare the two limiting cases. Such a power law favours unequal mass binaries, that need more than a Hubble time to form a DWD. Therefore we find 6 times less DWDs than in the original simulation, and, consequently, roughly 6 times less detections. To verify which of the two mass ratio distributions produce a population that is more compatible with observations, we compare the number of synthetic and observed binaries in the Solar neighbourhood (see unresolved DWD in Table 1 of Toonen et al., 2017). We find that the flat mass ratio distribution produces 7 ± 3 DWDs within 20 pc, while a power law with $b = -1$ predicts only 1^{+3}_{-1}. In the observed sample there is 1 confirmed isolated DWD and 5 DWD candidates. The candidates are stars with estimated masses that are too low ($\leq 0.5\,\mathrm{M}_\odot$) to have evolved as single stars, thus it is highly likely that these are binary stars with undetected companions (see Toonen et al., 2017, and references therein). Because of the large uncertainties in the number of DWDs from both sides: observations and simulations, we cannot place a strong constrain on our synthetic models. We can only conclude that our fiducial model, with the flat mass ratio distribution, is more consistent with the observed numbers within the uncertainties when including the DWD candidates.

The subset of *Gaia* and LSST binaries analysed in this work represent guaranteed detections for the LISA mission, and will provide a powerful tool for probing WD astrophysics and a unique opportunity of multi-messenger study for this class of objects. No other GW sources are expected to provide so large number of combined GW and EM detections. We defer to future work for the parameter estimation from EM and GW data for the sample of the combined EM and GW detections and the study of the applicability of these data to the study of the effects of tides in ultra-compact binaries and the kinematics of the Galaxy.

Chapter 4

Detectability of double white dwarfs in the Local Group with LISA

Korol, V., Koop, O., & Rossi, E. M. 2018, ApJL, 866, L20

Detached double white dwarf (DWD) binaries are one of the main science cases for the Laser Interferometer Space Antenna (LISA). As the most numerous LISA sources, they will provide important contributions towards understanding binary evolution, Supernovae Type Ia (SNIa) formation channels and the structure of the Milky Way. So far only detection prospects for the Milky Way have been predicted. In this letter we show that LISA has the potential to detect DWDs in neighbouring galaxies up to the border of the Local Group. In particular, we compute quantitative estimates for the number of detections in M31. We expect between a dozen to several tens of DWDs above the nominal detection threshold, for a mission duration between 4 and 10 yr. We show that detectable extra-galactic DWDs include those with the shortest orbital periods ($P < 10\,\mathrm{min}$) and with the highest chirp masses ($\mathcal{M} > 0.6\,\mathrm{M}_{\odot}$), that are candidates SNIa progenitor. These binaries are virtually undetectable at those distances in optical, implying that LISA could be the best instrument able to provide SNIa merger rates across the Local Group.

4.1 Introduction

Detached DWD binaries with orbital periods $< 1\,\mathrm{h}$ will be important Gravitational Wave (GW) sources for the LISA mission in many ways (Amaro-Seoane et al., 2017). Firstly, DWDs are guaranteed LISA sources. A number of short period DWDs have already been identified at optical wavelengths (e.g., Kupfer et al., 2018). Those with the strongest signals can be used as calibration sources as they will be detectable already after one week of observations; over time their signal will increase improving the accuracy with which these sources can be used to monitor data quality as new data are acquired (Littenberg, 2018). Secondly, DWDs will be the most numerous LISA sources. The total number of expected detections exceeds 10^5 (e.g., Korol et al., 2017; Marsh, 2011; Nelemans et al., 2001; Ruiter et al., 2010). Thus, for the first time LISA will provide a sizeable sample of short period DWD binaries to test binary formation theories and validate SNIa formation channels (e.g., Nelemans et al., 2001, 2004; Rebassa-Mansergas et al., 2018). Moreover, such a large number of individually resolved sources spread all over the Galaxy will allow us to map the Milky Way in GWs and precisely measure its structural parameters like scale radii of the bulge and the disc (Adams et al., 2012; Korol et al., 2018). When combining GW and optical measurements for DWDs with optical counterparts we will also be able to derive the mass of the bulge and the disc component of the Galaxy (Korol et al., 2018). DWDs are so common in the Milky Way that their unresolved signals will form a background for the LISA mission (e.g., Robson & Cornish, 2017). This background contains information on the overall stellar population in the Milky Way and can be also used to derive the Milky Way's parameters, like the disc scale height (Benacquista & Holley-Bockelmann, 2006). Finally, LISA will allow us to study the population of DWDs in the Milky Way's globular clusters, which is difficult to detect in optical because of the intrinsic faintness and crowdedness of DWDs in such dense environment (Benacquista et al., 2001; Kremer et al., 2018; Willems et al., 2007).

Previously the detectability of DWDs has been exclusively assessed in the Milky Way, while extra-galactic DWDs were only considered as contribution to the background noise (e.g., Farmer & Phinney, 2003; Kosenko & Postnov, 1998). In this letter we focus for the first time on the properties of extra-galactic DWDs that can be resolved by LISA in the Local Group, and especially in the Large and Small Magellanic clouds (LMC and SMC), and M31 (the Andromeda galaxy). We show that LISA will detect binaries with the shortest periods and highest total masses, and therefore double degenerate SNIa progenitors. As discussed in Rebassa-Mansergas et al. (2018), these are difficult to find with optical telescopes in the Milky Way. Essentially, they are too faint to be identified from Hα double-lined profiles in spectra and their eclipses are too short when considering the typical cadence of observations of optical sky surveys, like *Gaia*. Therefore LISA might be the best tool to allow statistical studies of these systems.

In this letter, we forecast the parameter space of DWDs accessible through GW observation located at the distance of SMC, LMC and M31 (Section 4.2). We use a synthetic population to quantify the number of detection for M31 (Section 4.3). In Section 4.4 we present our conclusions.

4.2 Maximal distance

In this section we consider an illustrative example of a monochromatic DWD binary, i.e. a binary whose orbital period decay due to GW emission is too small to be measured during the mission lifetime. A monochromatic assumption is justified when interested in the signal-to-noise ratio (SNR) only, as was already tested in Korol et al. (2017)[1]. Note, however, that the measurement of the orbital period decay is essential to recover the binary chirp mass and the distance from GW data. For a monochromatic source the SNR can be estimated as: (e.g., Maggiore, 2008)

$$\mathrm{SNR} = \mathcal{A}\ F(i,\theta,\phi,\psi)\ \sqrt{\frac{T_{\rm obs}}{S_{\rm n}(f)}}, \tag{4.1}$$

where $\mathcal{A}$ is the amplitude of the GW signal, $F(i,\theta,\phi,\psi)$ is a function that accounts for the instrument response to the binary inclination i, sky position (θ,ϕ) with respect to the detector and polarisation angle ψ averaged over one LISA orbit (Cornish & Larson, 2003, equation (42)), $T_{\rm obs}$ is the observation time and $S_{\rm n}(f)$ is the total noise spectral density (instrument + Galactic background) at the binary frequency $f = 2/P$, with P being the binary orbital period. The amplitude can be computed using the quadrupole approximation as:

$$\mathcal{A} = \frac{4(G\mathcal{M})^{5/3}(\pi f)^{2/3}}{c^4 d}, \tag{4.2}$$

where $\mathcal{M} = (m_1 m_2)^{3/5}/(m_1+m_2)^{1/5}$ is the chirp mass and d is the distance (e.g., Maggiore, 2008). We draw ψ randomly from a flat distribution between $[0,\pi]$. We adopt the sky- and inclination-averaged noise curve, $S_{\rm n}(f)$, corresponding to the LISA mission design accepted by ESA plus the Galactic background computed for the nominal (solid lines) and extended (dashed lines) mission duration of 4 yr and 10 yr respectively (Amaro-Seoane et al., 2017). Finally, we average the SNR over the inclination angle i and the position in the sky (θ,ϕ). Equation (4.2) shows that the strength of the signal mainly depends on three binary parameters: f(or P), $\mathcal{M}$ and d. Thus, we study binary detectability of DWDs with LISA as a function of these parameters.

In Figure 4.1 we plot in $P-\mathcal{M}$ space the sky- and inclination-averaged curves of SNR=7 at the distance of the LMC (yellow), SMC (cyan) and M31 (blue) for 4 yr (solid) and 10 yr (dashed) mission lifetimes. Thus, the areas above the curves delimit the parameter space detectable by LISA in these galaxies. At the distances of the LMC and SMC, LISA will be sensitive to DWDs with chirp masses $> 0.1\,\mathrm{M}_\odot$[2] Whereas at the distance of M31 LISA will be sensitive only to binaries with $\mathcal{M} > 0.5\,\mathrm{M}_\odot$ and $P < 10\,\mathrm{min}$. The white star shows a typical binary detectable at the distance of M31 (Figure 4.3) with $\mathcal{M} = 0.9\,\mathrm{M}_\odot$ and $P = 5\,\mathrm{min}$ (hereafter our test binary). Although the binary population synthesis model by Korol et al. (2017) predicts only a few of such binaries in the Milky Way, they would certainly be detected by LISA with precise measurement of their chirp mass and distance (e.g., Rebassa-Mansergas et al., 2018). The colour contour in Figure 4.1 shows the binary merger time:

$$\tau \simeq 1\,\mathrm{Myr}\ \left(\frac{P}{12\,\mathrm{min}}\right)^{8/3}\left(\frac{\mathcal{M}}{0.3\,\mathrm{M}_\odot}\right)^{-5/3}. \tag{4.3}$$

[1] We also specifically tested the monochromatic assumption for the Andromeda population (Sect. 4.3). We find that the monochromatic assumption typically overestimates SNR by 0.4.

[2] Note, that in this study we do not consider AM CVn systems which typically have $\mathcal{M} < 0.1\mathrm{M}_\odot$. when the orbital period $< 20\,\mathrm{min}$.

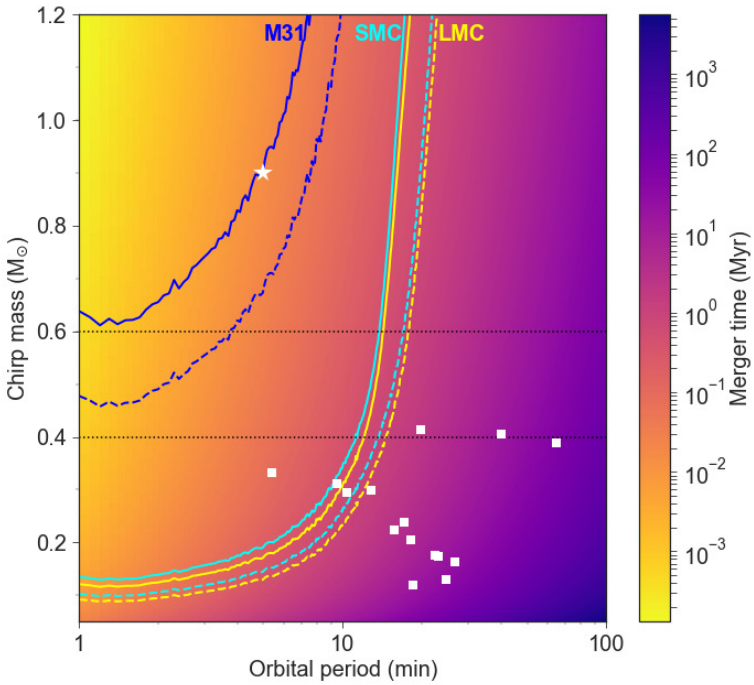

Figure 4.1: Curves of sky- and inclination-averaged SNR=7 in orbital period-chirp mass space evaluated at the distances of the LMC, SMC and M31 for 4 yr (solid) and 10 yr (dashed) mission lifetime. The color represents the merger time. White squares are known Galactic GW sources (DWDs and AM CVns) and the white star is our test binary.

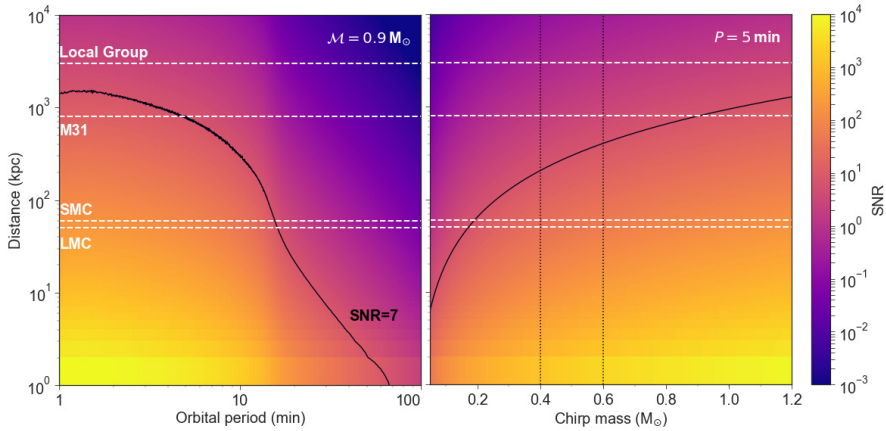

Figure 4.2: SNR for the test DWD in the distance-orbital period for $\mathcal{M} = 0.9\,M_\odot$ (left) and distance-chirp mass for $P = 5$ min (right) space after nominal 4 yr of observations. The black solid line represents the iso-SNR contour of 7. Dashed horizontal lines mark the distance of the LMC, SMC, M31 and the border of the Local Group.

Thus, Figure 4.1 reveals that DWDs accessible to LISA in the three considered galaxies will merge in < 1 Myr. The two horizontal lines at $\mathcal{M} = 0.6, 0.4\,M_\odot$ correspond to binaries with a total mass (M) equal to the Chandrasekhar mass when adopting respectively equal mass and $m_2/m_1 = 0.18$. This value is the minimum mass ratio for binaries with $M > 1.38\,M_\odot$ in the Korol et al. (2017) catalogue. Note that $\mathcal{M} = 0.6, 0.4\,M_\odot$ are the lower bounds of the parameter space corresponding to double degenerate SNIa progenitors. Finally, the white squares are known Galactic GW sources (DWDs and AM CVns) from Kupfer et al. (2018) showing the part of parameter space explored so far at optical wavelengths. In particular, those with the shortest periods (HM Cnc, V407 Vul, ES Cet and SDSS J0651) could be detected by LISA if placed at the distance of LMC and SMC. On the other hand, the parameter space accessible in M31 is currently unprobed.

Next, we consider a test binary (white star in Figure 4.1) to assess the maximal distance detectable by LISA. Figure 4.2 represents the sky- and inclination-averaged SNR in the distance-orbital period parameter space for fixed $\mathcal{M} = 0.9\,M_\odot$ (left panel) and in distance-chirp mass parameter space for fixed $P = 5$ min (right panel). As a reference we indicate the distance of LMC, SMC, M31 and the radius of the Local Group with dashed horizontal lines. The black solid line shows the LISA detection threshold of 7. The area below the curve represents the parameter space detectable by LISA and shows that LISA has the potential to detect DWDs with very short periods and high chirp masses, like our test source, almost up to the border of the Local Group.

4.3 DWD detections in Andromeda

Here we address quantitative estimates for the number of detections in the Andromeda galaxy. Properties of extra-galactic DWDs are not known, since not a single DWD has been observed outside our Galaxy. However, because M31 is a spiral galaxy similar to the Milky Way, we can extrapolate the properties of the Galactic population of DWDs to that of Andromeda. To obtain a mock population we use the binary population synthesis code SeBa (Portegies Zwart & Spreeuw, 1996; Toonen et al., 2012), that has been employed to forecast LISA detections in the Milky Way (Amaro-Seoane et al., 2017; Korol et al., 2017). The initial stellar population is obtained assuming the Kroupa initial mass function, a flat binary mass ratio distribution, a log-flat distribution for the binary semi-major axis, a thermal distribution for the orbit eccentricity, an isotropic distribution for binary inclination angles, and a constant binary fraction of 50% (Duchêne & Kraus, 2013; Kroupa et al., 1993; Raghavan et al., 2010). We use the $\gamma\alpha$ prescription for the common envelope phase, calibrated on observed DWDs in the Milky Way (Nelemans et al., 2001). The sensitivity of our model to these assumptions is addressed in Korol et al. (2017) and Toonen et al. (2017). Finally, we assume the total stellar mass of Andromeda to be twice that of the Milky Way (e.g., Sick et al., 2015). For all binaries we assign galactic coordinates $(l, b) = (121, -21)$, $d = 800\,\mathrm{kpc}$ and an inclination angle randomly drawn from a uniform distribution in $\cos i$. We compute the SNRs as described in Section 4.2.

We find 17 (60) binaries with SNR ≥ 7 in 4 (10) yr of the mission (see Figure 4.3). In particular, the majority are CO+CO and the small fraction are CO+ONe DWDs. These detections will clearly appear in the LISA sky as an over-density located at the position of M31, far from the Galactic disc. Once these sources are identified, a careful modelling of the waveform would yield an independent confirmation of their extra-galactic origin as well a novel determination of Andromeda distance. Specifically, for binaries in M31 the distance can be determined up to 20%, using equation (29) from Takahashi & Seto (2002). All the binaries detectable by LISA (SNR>7) will merge in less than 0.1 Myr. We also find that the LISA sample is complete for $P < 3.5\,\mathrm{min}$ and $\mathcal{M} > 0.7\,\mathrm{M}_\odot$. The completeness is $\sim 50\%$ for DWDs with $P < 4.5\,\mathrm{min}$ and $\mathcal{M} > 0.6\,\mathrm{M}_\odot$, and drops to $\sim 10\%$ for $P < 10\,\mathrm{min}$ and $\mathcal{M} > 0.6\,\mathrm{M}_\odot$. Given the completeness and the merger time across the sample we will be directly able to estimate the DWD merger rate in M31. Note, that here we implicitly assume that all DWDs with chirp mass $> 0.6\,\mathrm{M}_\odot$ merge (e.g., Shen, 2015). However, it is also possible that at orbital periods of $2 - 3\,\mathrm{min}$ a DWD starts mass transfer, but how frequent this is depends on the uncertainties in mass transfer physics (Marsh et al., 2004).

Figure 4.3 shows that there are many more DWDs lying just below the detection threshold. A possible way of increasing the number of detections is to perform a targeted search for signals at the position and distance of M31. Specifically, the results of this study can be used to construct priors for the frequency and chirp mass. We also suggest that using optical measurements for M31 as priors on the coordinates and distance can be advantageous.

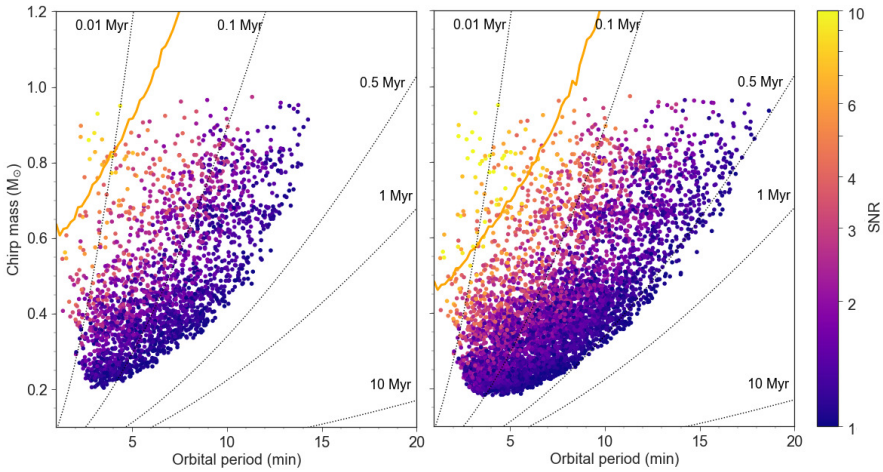

Figure 4.3: DWDs in M31: after 4 yr (left panel) and after 10 yr (right panel) observation time with LISA. The orange solid line represents the sky- and inclination-averaged LISA detection threshold of 7. Black dotted lines are iso-merger contours.

4.4 Conclusions

In this letter we explored the detectability of DWDs outside the Milky Way. We proved that LISA has the potential to detect binaries in neighboring galaxies: LMC, SMC and M31. We find that, in the LMC and SMC, LISA can detect DWDs with $P < 20\,\mathrm{min}$ and $\mathcal{M} > 0.1\,\mathrm{M}_\odot$, while in M31 LISA will be sensitive to those with $P < 10\,\mathrm{min}$ and $\mathcal{M} > 0.6\,\mathrm{M}_\odot$. Using an example DWD with $P = 5\,\mathrm{min}$ and $\mathcal{M} = 0.9\,\mathrm{M}_\odot$, we showed that binaries with such characteristics can be detected up to 1 Mpc distance, i.e. within the large volume of the Local Group. In the Andromeda galaxy we found a dozen, to several tens, of DWDs above the LISA detection threshold for 4 and 10 yr mission. This gives optimistic prospects for detecting other kind of stellar type GW sources like AM CVns and ultra-compact X-ray binaries, which will likely have an electromagnetic counterpart. A large fraction of extra-galactic DWDs detectable by LISA will have total mass exceeding the Chandrasekhar mass limit and will merge in less than 1 Myr, meaning that LISA has the potential to provide SNIa merger rates across the Local Group.

Chapter 5

A multi-messenger study of the Milky Way's stellar disc and bulge with LISA, Gaia and LSST

Korol, V., Rossi, E. M., & Barausse, E. 2019, MNRAS, 483, 5518

The upcoming LISA mission offers the unique opportunity to study the Milky Way through gravitational wave radiation from a large population of Galactic binaries. Among the variety of Galactic gravitational wave sources, LISA is expected to individually resolve signals from $\sim 10^5$ ultra-compact double white dwarf (DWD) binaries. DWDs detected by LISA will be distributed across the Galaxy, including regions that are hardly accessible to electromagnetic observations such as the inner part of the Galactic disc, the bulge and beyond. We quantitatively show that the large number of DWD detections will allow us to use these systems as tracers of the Milky Way potential. We demonstrate that density profiles of DWDs detected by LISA may provide constraints on the scale length parameters of the baryonic components that are both accurate and precise, with statistical errors of a few percent to 10 percent level. Furthermore, the LISA sample is found to be sufficient to disentangle between different (commonly used) disc profiles, by well covering the disc out to sufficiently large radii. Finally, up to $\sim$ 80 DWDs can be detected through both electromagnetic and gravitational wave radiation. This enables multi-messenger astronomy with DWD binaries and allows one to extract their physical properties using both probes. We show that fitting the Galactic rotation curve constructed using distances inferred from gravitational waves *and* proper motions from optical observations yield a unique and competitive estimate of the bulge mass. Instead robust results for the stellar disc mass are contingent upon knowledge of the Dark Matter content.

5.1 Introduction

Because of our vantage observation point, the Milky Way is an outstanding laboratory for understanding galaxies, whose assembly histories bear the imprint of the cosmological evolution of our Universe. As remnants of the oldest stars in the Milky Way, white dwarfs (WDs) are unique tracers of the Milky Way's properties. For example, using the fact that the WD luminosity depends mainly on the stellar age, one can date different Galactic populations by constructing a WD luminosity function (García-Berro & Oswalt, 2016; Kilic et al., 2017; Liebert et al., 1988; Rowell & Hambly, 2011). Moreover, the WD luminosity function contains information about the star formation and death rates over the history of the Galaxy. The most ancient WDs in the Galaxy can make up a sizeable fraction of the dark Galactic stellar halo mass, and, thus, have a direct impact on our quantitative estimates of the total amount of dark matter in the Galaxy (e.g. Alcock et al., 2000; Flynn et al., 2003; Napiwotzki, 2009). In this work we quantitatively show that WDs in close binaries are unique multi-messenger tools to probe the Milky Way's structure.

Double WDs (DWDs) are expected to be detected through gravitational wave (GW) emission by the Laser Interferometer Space Antenna (LISA), an ESA space mission officially approved in 2017 (Amaro-Seoane et al., 2017). LISA is designed to detect GW sources in the mHz frequency range, such as merging massive black hole binaries ($\sim 10^4\,\mathrm{M}_\odot - 10^7\,\mathrm{M}_\odot$) up to $z \sim 15-20$ (e.g. Klein et al., 2016), extreme mass ratio inspirals (e.g. Babak et al., 2017) and Galactic binaries (Breivik et al., 2018; Korol et al., 2017; Kremer et al., 2017). Therefore, besides probing high-redshift cosmology (Caprini et al., 2016; Tamanini et al., 2016) and testing the theory of General Relativity in the strong gravity regime (Barausse et al., 2016; Berti et al., 2016; Brito et al., 2017), LISA will be the only gravitational experiment capable of exploring the Milky Way's structure. Remarkably, the expected number of Galactic binaries that LISA will be able to resolve individually (i.e. measure their individual properties) amounts to $\sim 10^4$, among which DWDs will represent the absolute majority (e.g. Korol et al., 2017; Kremer et al., 2017; Nelemans et al., 2004; Ruiter et al., 2010; Shah et al., 2012). Overlapping signals from unresolved binaries present in the Galaxy will instead form a stochastic background signal (Edlund et al., 2005; Robson & Cornish, 2017; Timpano et al., 2006). Both resolved and unresolved LISA signals will provide information on the Galactic stellar population as a whole, and can thus be used to study the Milky Way's baryonic content and shape. A first quantitative study was carried out by Benacquista & Holley-Bockelmann (2006), where the authors show that the level and shape of the DWD background as well as the distribution of resolved sources will provide constraints on the scale height of the Galactic disc. In this paper we focus on resolved binaries only and we demonstrate their potential for constraining the shape of both the disc and the bulge. Moreover, we show that the power to constrain the overall properties of the Galactic baryonic potential will be significantly enhanced by using GWs in combination with electromagnetic (EM) observations. The success of this synergy is due to LISA's ability to localise binaries through virtually the whole Galactic plane, thus mapping its shape, while optical observations yield the motion of stars, tracing the underlying total enclosed mass.

In this work, we use a synthetic population of detached DWD binaries (Section 5.2) to investigate the precision of LISA distance measurements (Section 5.3) and to test the potential of using the spatial distribution of the LISA detections to reconstruct

the density profiles of the Milky Way stellar population (Section 5.4). We focus on detached binaries because they are "clean" systems where systematics in the system's parameter determination are reduced. We also simulate the performances of *Gaia* and the LSST at providing astrometric measurements for eclipsing binaries, and we simultaneously fit the stellar density shape *and* the Milky Way's rotation curve (Section 5.5). In Section 5.6 we present our conclusions.

5.2 Synthetic population

The detailed description of our population synthesis model was presented in Toonen et al. (2012, 2017) and Korol et al. (2017), to which we refer for further details. In this section we summarise the most important features of the adopted model, focusing on the Milky Way structure and potential. We also outline the method that we have used to simulate detections of DWDs with *Gaia* and the LSST, and the computation of the signal-to-noise ratios for the latest design of the LISA mission (Amaro-Seoane et al., 2017).

5.2.1 Initial distributions

In modelling the synthetic population of DWDs we rely on the population synthesis code SeBa Portegies Zwart & Verbunt (1996, for updates see Nelemans et al. 2001, Toonen et al. 2012). The initial stellar population is obtained with a Monte Carlo approach, assuming a binary fraction of 50% and adopting the following distributions for the binary parameters. First, we draw the mass of the single stars between 0.95 - 10 $M_\odot$ from the Kroupa initial mass function (IMF, Kroupa et al., 1993). Then, we draw the mass of the secondary star from a flat mass ratio distribution between 0 and 1 (Duchêne & Kraus, 2013). We adopt a log-flat distribution for the binary semi-major axis and a thermal distribution for the orbit eccentricity (Abt, 1983; Heggie, 1975; Raghavan et al., 2010). Finally, we draw the binary inclination angle i isotropically (i.e. from a uniform distribution in $\cos i$). The sensitivity of our population model to these assumptions is discussed in Korol et al. (2017) and Toonen et al. (2017).

In the canonical picture of binary evolution, a common envelope (CE) phase is required to form a close system (Paczynski, 1976; Webbink, 1984). This is a short phase in binary evolution in which the more massive star of the pair expands and engulfs the companion. When this happens the binary orbital energy and angular momentum can be transferred to the envelope, due to the dynamical friction that the companion star experiences when moving through the envelope. Typically, this process is implemented in the binary population synthesis by parametrising the conservation equation for either the energy or the angular momentum (see Ivanova et al., 2013, for a review). In our previous work we modelled two populations, one for each CE parametrisation, to study whether optical surveys such as *Gaia* or LSST, as well as LISA in GWs, will be able to discriminate between the two. In this paper we are mainly interested in the spatial distribution of DWDs, which does not depend on the specific CE prescription, and thus we use just one model population. In particular, we choose the parametrisation based on the angular momentum balance (γ-parametrisation), which was introduced to reconstruct the population of observed DWDs and was fine-tuned using them (Nelemans et al., 2000, 2001; Nelemans & Tout, 2005).

Table 5.1: Milky Way model

Parameter	Value
Bulge	
$M_{\rm b}$	$2.6 \times 10^{10}\,{\rm M}_\odot$
$r_{\rm b}$	$0.5\,{\rm kpc}$
$r_{\rm b,max}$	$3\,{\rm kpc}$
Stellar disc	
$M_{\rm d}$	$5 \times 10^{10}\,{\rm M}_\odot$
$R_{\rm d}$	$2.5\,{\rm kpc}$
$R_{\rm d,max}$	$19\,{\rm kpc}$
$Z_{\rm d}$	$0.3\,{\rm kpc}$
DM halo	
ρ_h	$0.5 \times 10^{7}\,{\rm M}_\odot{\rm kpc}^{-3}$
$M_{\rm h}$	$4.8 \times 10^{11}\,{\rm M}_\odot$
$r_{\rm h}$	$20\,{\rm kpc}$
$r_{\rm h,max}$	$100\,{\rm kpc}$

5.2.2 Galaxy model: density distribution, potential and rotation curve

We consider a simple model for the Milky Way, which we assume to be comprised of a bulge, a stellar disc and a dark matter (DM) halo. We distribute DWDs in the bulge and in the disc, while the DM halo is needed to reproduce Galactic kinematics. We do not take into account the stellar halo component because the properties of the WD population in the halo, and those of the stellar halo itself, are not well known (e.g. Cojocaru et al., 2015). Furthermore, the signal arising from the halo population is not expected to contribute significantly to the overall GW signal from the Galaxy (Ruiter et al., 2009).

The density of DWDs in the disc is assumed to fall exponentially in the radial direction, R, and to depend on the distance from the mid-plane, Z, through a sech^2 function (e.g., Robin et al., 2014). For simplicity, we neglect the dependence on the stellar age and mass when distributing DWDs in the Z direction, and we assume that they do not migrate radially. To account for the star formation history of the Milky Way disc we use the plane-projected star formation rate from Boissier & Prantzos (1999), $\rho_{\rm BP}$, and assume the age of the Galaxy to be 13.5 Gyr (e.g. Jurić et al., 2008). Analytically, the density distribution of the disc component for our model can be written as

$$\rho_{\rm disc}(t, R, z) = \rho_{\rm BP}(t)\, e^{-R/R_{\rm d}}\, {\rm sech}^2\left(\frac{z}{Z_{\rm d}}\right)\ {\rm M}_\odot\,{\rm kpc}^{-3}, \tag{5.1}$$

where $0 \leq R \leq 19$ kpc is the cylindrical radius measured from the Galactic centre, $R_{\rm d} = 2.5\,{\rm kpc}$ is the characteristic scale radius, and $Z_{\rm d} = 300$ pc is the characteristic scale height of the disc (Jurić et al., 2008). The total mass of the disc in our model is $5 \times 10^{10}\,{\rm M}\odot$. We assume the distance of the Sun from the Galactic centre to be $R_\odot = 8.5\,{\rm kpc}$ (e.g. Schönrich, 2012).

We model the bulge component by doubling the star formation rate in the inner

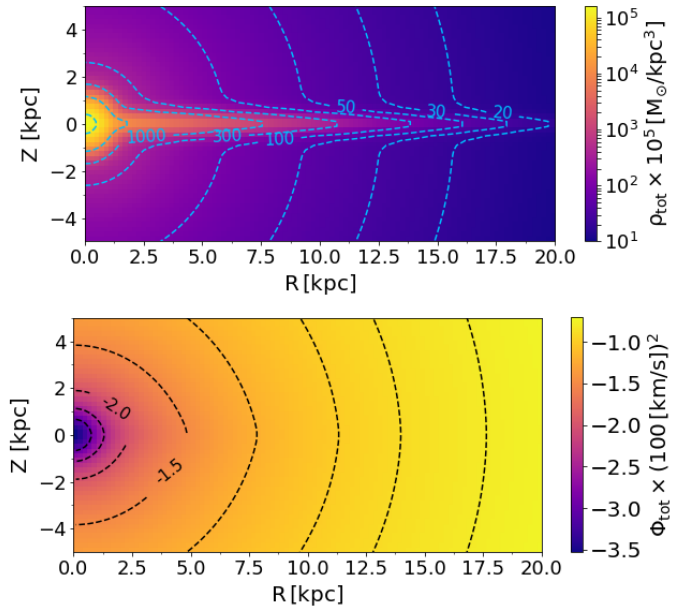

Figure 5.1: Density and potential maps of our Milky Way fiducial model in the $R-Z$ plane, computed numerically with the GALPYNAMICS package. Contour levels in the upper panel are $(20, 30, 50, 100, 300, 10^3, 10^4, 10^5) \times 10^5\,M_\odot/kpc^3$. Contour levels in the lower panel corresponds to $(-3, -2.5, -2, -1.5, -1.2, -1, -0.9, -0.8) \times (100\,km/s)^2$.

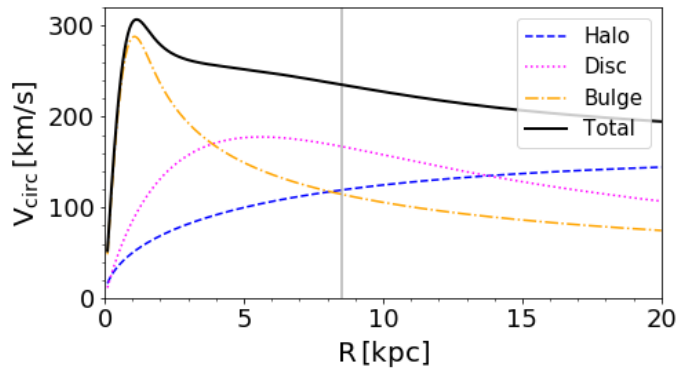

Figure 5.2: Rotation curve of our Milky Way fiducial model. The contributions from the disc, bulge and halo are shown by the dotted magenta, dashed-dotted yellow and dashed blue curves respectively. The total circular speed, given by the sum in quadrature of the circular speeds of the components, is represented by the black solid line. The circular velocity at the position of the Sun (8.5 kpc), marked by the grey vertical line, is 235 km/s.

3 kpc of the Galaxy and distributing DWDs according to

$$\rho_{\rm bulge}(r) = \frac{M_{\rm b}}{(\sqrt{2\pi}r_{\rm b})^3} e^{-r^2/2r_{\rm b}^2}\ {\rm M}_\odot\,{\rm kpc}^{-3}, \tag{5.2}$$

where r is the spherical distance from the Galactic centre, $M_{\rm b} = 2.6 \times 10^{10}\,{\rm M}\odot$ is the total mass at the present time, and $r_{\rm b} = 0.5\,{\rm kpc}$ is the characteristic radius (e.g. Sofue et al., 2009).

To model the density distribution of the DM halo we use the Navarro-Frenk-White profile (Navarro et al., 1996):

$$\rho_{\rm DM}(r) = \frac{\rho_{\rm h}}{(r/r_{\rm s})(1+r/r_{\rm s})^2}\ {\rm M}_\odot\,{\rm kpc}^{-3}, \tag{5.3}$$

where $r_{\rm s} = 20\,{\rm kpc}$ is the scale length of the halo and $\rho_{\rm h} = 0.5\times10^7\,{\rm M}_\odot{\rm kpc}^{-3}$ is the halo scale density. The total mass of the halo can be obtained by integrating equation (5.3) from the centre to the maximum Galactocentric radius of 100 kpc, which for our fiducial parameters yields $4.8 \times 10^{11}\,{\rm M}_\odot$. We summarise the values of the parameters adopted for our Milky Way fiducial model in Table 5.2.1.

The total potential can be computed by solving the Poisson equation

$$\nabla^2\Phi_{\rm tot} = 4\pi G(\rho_{\rm disc} + \rho_{\rm bulge} + \rho_{\rm DM}). \tag{5.4}$$

We solve equation (5.4) numerically using the GALPYNAMICS Python package, which is designed for the computation and fitting of potentials, density distributions and rotation curves[1]. We represent the resulting total density distribution and potential in Fig. 5.1. Both panels show a very prominent and concentrated bulge component reflected by the much closer iso-density (upper panel) and equipotential (lower panel) contour lines near the centre. The contribution of the disc inside the solar Galactocentric radius is clearly seen in the upper panel, and can be inferred from the flattening of the equipotential lines in the vertical direction in the lower panel of Fig. 5.1. At $R > 15\,{\rm kpc}$ the halo component becomes dominant, as reflected by the spherical shape of the iso-density and equipotential contours. We compute the Galactic rotation curve numerically using GALPYNAMICS as

$$V_{\rm circ}^2(R) = R\frac{{\rm d}\Phi_{\rm tot}}{{\rm d}R}. \tag{5.5}$$

The result is illustrated in Fig. 5.2, which shows that in our Milky Way model the bulge component has an important dynamical effect in the central region of the Galaxy up to $\sim 4\,{\rm kpc}$. In the region between 4 and 14 kpc, the disc dominates the dynamics of the Galaxy, while at larger radii the DM halo provides the largest contribution to the rotation curve. In our model the circular velocity at the position of the Sun is $V_0 = 235\,{\rm km/s}$. To compute the random component of DWD motion, we assume that the velocity distribution in the disc is governed by only two constants of motion, the energy and the angular momentum along the Z direction. Consequently, the specific low-order moments of the velocity components can be found as (Binney & Tremaine, 2008)

$$\overline{v_{\rm R}^2} = \overline{v_{\rm Z}^2} = \frac{1}{\rho(R,Z)}\int_Z^\infty dZ'\rho(R,Z')\frac{\partial\Phi_{\rm tot}}{\partial Z'}, \tag{5.6}$$

[1] GALPYNAMICS is a free source Python package developed by G. Iorio and available at https://github.com/iogiul/galpynamics

where $\rho(R, Z)$ is the density distribution of the Galactic component (bulge or disc) in cylindrical coordinates. Assuming that there is no stellar motion in the radial and vertical directions, equation (5.6) provides a direct estimate of the velocity dispersion $\sigma_{\rm R}$ and $\sigma_{\rm Z}$. From equation (5.6) we obtain the velocity moment in the azimuthal direction:

$$\overline{v_\phi^2} = \overline{v_{\rm R}^2} + \frac{R}{\rho}\frac{\partial(\rho\overline{v_{\rm R}^2})}{\partial R} + R\frac{\partial\Phi_{\rm tot}}{\partial R}. \tag{5.7}$$

We evaluate the last two equations numerically using GALPYNAMICS. At the Sun's position we obtain $\sigma_{\rm R}, \sigma_\phi$ and $\sigma_{\rm Z}$ equal to $15, 30$ and $15\,{\rm km/s}$ respectively.

5.2.3 WD magnitudes

The absolute magnitudes of WDs (bolometric and *ugriz*-Sloan bands) in our simulation are calculated from the WD cooling curves of pure hydrogen atmosphere models (Holberg & Bergeron, 2006; Kowalski & Saumon, 2006; Tremblay et al., 2011, and references therein). To convert the absolute magnitudes to observed magnitudes (e.g. for the Sloan r band) we use:

$$r_{\rm obs} = r_{\rm abs} + 10 + 5\log d + 0.84A_{\rm V}, \tag{5.8}$$

where d is the distance to the source in kpc, $0.84A_{\rm V}$ is the extinction in the Sloan r band and $A_{\rm V}$ is the extinction in the V band. To compute the value of $A_{\rm V}$ at the source position, defined by the Galactic coordinates (l, b) and the distance d, we use

$$A_{\rm V}(l, b, d) = A_{\rm V}(l, b)\tanh\left(\frac{d\sin b}{h_{\rm max}}\right), \tag{5.9}$$

where $A_{\rm V}(l, b)$ is the integrated extinction in the direction defined by (l, b) from Schlegel et al. (1998), $h_{\rm max} \equiv \min(h, 23.5 \times \sin b)$ and $h = 120$ pc is the Galactic scale height of the dust (Jonker et al., 2011). To convert *ugriz*-magnitudes into *Gaia* G magnitudes we apply a colour-colour polynomial transformation with coefficients chosen according to Carrasco et al. (2014).

5.2.4 Detection of DWDs with LISA

GWs produced by a binary of compact objects sufficiently far from coalescence at the lowest order can be described by the quadrupole approximation (Landau & Lifshitz, 1971). For a circular binary the quadrupole approximation yields a coalescence time due to GW emission of (Maggiore, 2008):

$$\tau \simeq 1\,{\rm Myr}\,\left(\frac{P}{12\,{\rm min}}\right)^{8/3}\left(\frac{\mathcal{M}}{0.3\,{\rm M}_\odot}\right)^{-5/3}, \tag{5.10}$$

where we use typical values for the binary orbital period P and the chirp mass $\mathcal{M} = (M_1 M_2)^{3/5}/(M_1 + M_2)^{1/5}$ for our population in Chapter 3. Thus, a typical merger time for a DWD in our mock catalogue is of the order of Myr. This is six orders of magnitude larger than the LISA mission lifetime, thus DWDs can be treated as quasi-monochromatic GW sources. The dimensionless GW amplitude can be found as

$$A = \frac{5}{96\pi^2}\frac{\dot{f}}{f^3 d} \tag{5.11}$$

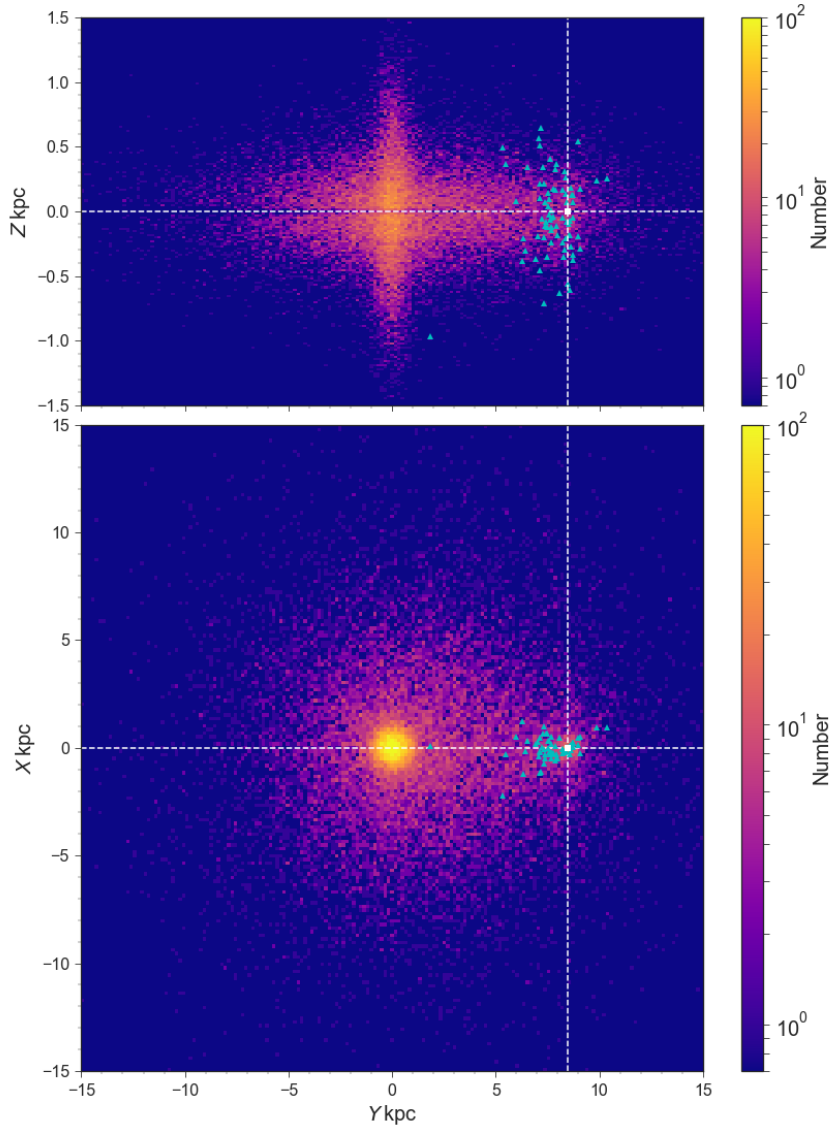

Figure 5.3: Source-count maps of DWDs detected by LISA (SNR>7) in the Galactocentric Cartesian coordinate system defined by equation (5.22): in the $Y-Z$ plane (top panel) and in the $Y-X$ plane (bottom panel). The white square identifies the position of the Sun in the Galaxy, $(0, 8.5\,\mathrm{kpc}, 0)$. Blue triangles represent the position of EM counterparts detected with *Gaia* and/or LSST.

where $f = 2/P$ is the GW frequency,

$$\dot{f} = \frac{96}{5}\pi^{8/3}\left(\frac{G\mathcal{M}}{c^3}\right)^{5/3} f^{11/3} \tag{5.12}$$

is the frequency derivative or chirp (Maggiore, 2008). From equations (5.11)-(5.12), it follows that the distance can be determined directly by measuring the three GW observables $f, \dot{f}$ and A. However, this is possible only for detached binaries whose dynamics is driven only by emission of GWs. In the case of accreting DWDs (so-called AM CVns), the chirp contains components of astrophysical origin such as mass transfer or tides. Consequently, the distance to these sources needs to be determined differently and requires additional EM observations (e.g. Breivik et al., 2018). Since this work deals with the possibility of mapping the Milky Way potential by GW observations, we focus on detached DWDs only. A distinction between the two types of systems in the LISA data is possible based on the sign of $\dot{f}$: detached (AM CVns) systems are expected to have positive (negative) $\dot{f}$. This is due to the fact that the frequency of an AM CVn system decreases with time because of mass transfer, while the frequency of a detached system increases because of GW emission (e.g. Nelemans et al., 2004).

When considering a space mission such as LISA, which is constantly in motion with changing speed and position with respect to a source in the sky, it is more convenient to work in the heliocentric ecliptic reference frame. In this frame the coordinates of the source are fixed and the modulation of the GW signal in time is encoded in the detector response function (e.g. Cutler, 1998). We use the pyGaia[2], a Python tool kit to transform the coordinates of DWDs from the galactic heliocentric frame to the ecliptic heliocentric frame (so that $r_{\rm ecl} = d$), and we define the LISA reference frame as

$$\begin{aligned} r &= r_{\rm ecl} \\ \theta &= \pi/2 - \arccos(z_{\rm ecl}/r_{\rm ecl}) \\ \phi &= \arctan(y_{\rm ecl}/x_{\rm ecl}). \end{aligned} \tag{5.13}$$

To compute signal-to-noise ratios (SNRs) for our mock population of DWDs over the nominal 4 yr mission lifetime, we employ the Mock LISA Data Challenge (MLDC) pipeline, which was designed for the simulation and analysis of GW signals from Galactic binaries (for details see Littenberg, 2011). The MLDC pipeline characterises GW signals in terms of 9 parameters: $A, f, \dot{f}, \ddot{f}$, sky location (θ, and ϕ), orbital inclination i, GW polarisation ψ and the binary initial orbital phase ϕ_0. Given a synthetic instrument noise curve, and setting an observation time and a detection threshold, the MLDC pipeline provides a catalogue of the sources that can be resolved individually (i.e. those with SNR above the detection threshold), computes the background from unresolved sources in the catalogue, and estimates the uncertainties on the source parameters by computing the Fisher Information Matrix (FIM). We adopt the detector's design as approved by ESA, i.e. a three-arm configuration with 2.5×10^6 km arm length and the instrumental noise curve from Amaro-Seoane et al. (2017).

We find 2.6×10^4 DWDs in our catalogue with SNR$>$7. Their distribution in the Milky Way is represented in Fig. 5.3: the source-count map is shown in the $Y - Z$ plane (top panel) and in the $Y - X$ plane (bottom panel). We denote the position of

[2]In this paper we extensively use tools provided by pyGaia, such as transformations between astrometric observables and transformations between sky coordinate systems, not only for simulating *Gaia* data, but also as a general astronomical tool.

the Sun by a white square. Figure 5.3 reveals that LISA will detect DWD binaries to large distances, mapping also the opposite side of the Milky Way. Both maps show a prominent peak in the central part of the Galaxy, due to the bulge, whereas the number of detected sources declines when moving outwards (up to $> 15\,\mathrm{kpc}$) from the centre, tracing the underlying disc stellar population. The $Y - X$ map shows an asymmetry with respect to the $Y = 0$ line due to an observation bias. Indeed, because the amplitude and SNR of GW signals scale as $1/d$, nearby sources have stronger signals, and consequently there are more detected DWDs around the Sun. We derive a correction factor to compensate for this bias in Appendix C.

5.2.5 Detection of optical counterparts with *Gaia* and LSST

Additional information (such as the motion of DWDs) needed to constrain the Milky Way potential cannot be extracted from GW data, but can be recovered from EM observations. The sky localization of a source is typically poorly constrained by GWs, compared to optical observations. A typical position error for LISA is $\sim 10\,\mathrm{deg}$, while a typical position error for *Gaia* is of the order of μas (Gaia Collaboration et al., 2016). This makes it difficult to identify counterparts to GW sources in EM databases. In practice, in order to assemble a sample of optical counterparts, one possibility is to search in optical catalogues for periodically variable sources with a frequency and within an area on the sky matching those provided by LISA. To assess whether this is possible we focus on edge-on binaries, which allow for better parameter estimation with GWs and are easy to identify in optical as eclipsing. In particular, we consider two optical surveys, which by the time LISA is launched will be operational and which are expected to provide large stellar catalogues: *Gaia* and the Large Synoptic Survey Telescope (LSST, LSST Science Collaboration et al., 2009). Our previous study shows that the deep magnitude limit of 21 for *Gaia* and 24 for the LSST enables the detection of a significant fraction of the overall DWD Galactic population (Korol et al., 2017). Here below we summarise our method and results.

We simulate the optical light curves of DWDs detectable with LISA by computing the flux of a binary for a given orbital phase. We consider spherically symmetric stars with uniform surface brightness, neglecting the limb darkening effect. In this purely geometric model, we ignore the gravitational distortion of the stars and their mutual heating, which is justified given the small size of WDs and the roughly equal size of the binary components. To evaluate the relative photometric error of a single observation with *Gaia* in the *Gaia* G-band we use:

$$\sigma_{\mathrm{G}} = 1.2 \times 10^{-3}(0.04895\tilde{z}^2 + 1.8633\tilde{z} + 0.00001985)^{1/2}, \tag{5.14}$$

where $\tilde{z} = \max[10^{0.4(12-15)}, 10^{0.4(G-15)}]$ (Gaia Collaboration et al., 2016). To evaluate the expected photometric error of a single observation (as an example we use *Sloan* r-band) with the LSST we use

$$\sigma_{\mathrm{r}} = (\sigma_{\mathrm{sys}}^2 + \sigma_{\mathrm{rand}}^2)^{1/2}, \tag{5.15}$$

where $\sigma_{\mathrm{sys}} = 0.005$ is the systematic photometric error, $\sigma_{\mathrm{rand}}^2 = (0.04 - \tilde{\gamma})x + \tilde{\gamma}x^2$, $x = 10^{(m-m_5)}$ is the random photometric error, and m_5 and $\tilde{\gamma}$ are respectively the 5σ limiting magnitude for a given filter and the sky brightness in a given band (LSST Science Collaboration et al., 2009). Finally, we apply a Gaussian noise to our synthetic light curves.

Next, we sample the light curves using the predicted *Gaia* observations obtained with the *Gaia Observation Forecast Tool*[3], which provides a list of times (in TCB, Barycentric Coordinate Time) for a given target in the sky. We assign the initial orbital phase and sample the synthetic light curves with *Gaia* observations, which we compute for each source individually. To simulate the LSST sampling we use the anticipated regular cadence of 3 days over the nominal ten-year life span of the mission. In order to establish the detectability of the light curves, we first verify whether the time sequence of simulated observations presents variability, by evaluating the χ^2 for the observation sequence with respect to the average magnitude; and, second, we require a minimum number of observations to sample the eclipse phase ($\sim 3\%$ of the total number of observations). For each binary we compute 100 realisations of the light curve sampling by randomising over the initial orbital phase, and we define the probability of detection as the number of times the light curve was classified as detected out of 100.

We find 25 and 75 EM counterparts of the LISA sources with respectively *Gaia* and LSST, in agreement with our previous work (Korol et al., 2017, where, however, we simulate GW signals differently). Since there is an overlap of 23 binaries between *Gaia* and LSST detections, the total number of unique EM counterparts actually amounts to 78. We represent these sources with blue triangles in Fig. 5.3. It is evident that there is a lack of EM detections in the disc plane and in the central bulge (i.e. at low Galactic latitudes) due to extinction effects. The majority of EM counterparts will be detected at short distances compared to the extension of the stellar disc: within 2 kpc with *Gaia* and within 10 kpc with the LSST. Thus, we anticipate that combined GW and EM catalogues will provide information mainly on the local properties of the Milky Way.

5.3 Distance determinations

The precise determination of distances is a crucial step for studying the spatial distribution of DWDs in the Galaxy. For DWD binaries the distance can in principle be independently measured from GW and optical observations, when both are available. In this section we first forecast the LISA performance at measuring distances when considering a 4-year long observation run, and then we turn to the distance determination from parallax with *Gaia* and the LSST end-of-mission performances. Finally, for the DWDs with optical counterparts, we show that parallaxes can be used to improve the GW distance estimates. In the following we denote the distance estimated from GWs and its error with the subscript "GW", and the distance estimated from parallax measurements and its error with the subscript "EM". As in previous Sections, we refer to d with no subscript as the true distance to the source.

5.3.1 Distances from GW data

The distance can be found directly from the three GW observables A, f and $\dot{f}$ by inverting equation (5.11):

$$d_{\rm GW} = \frac{5c}{96\pi^2}\frac{\dot{f}}{f^3 A}. \tag{5.16}$$

[3] http://gaia.esac.esa.int/gost/

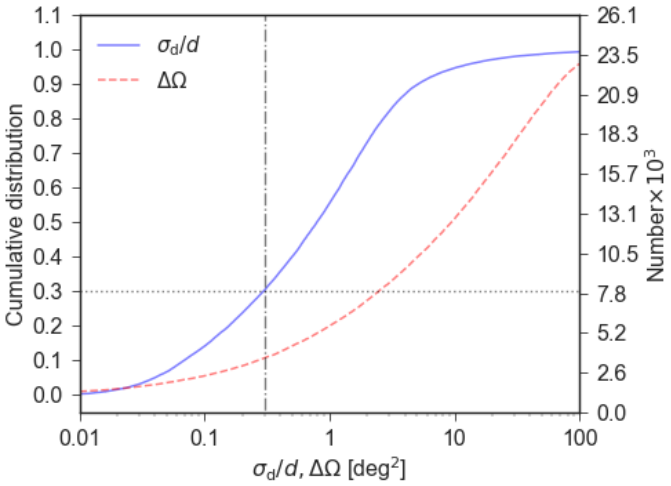

Figure 5.4: Cumulative distribution (left y axis) and total number of detected binaries (right y axis) for the relative error in distance (blue solid line) and for the sky localisation error (red dashed line). The dashed vertical line marks our quality requirement $\sigma_d/d < 0.3$, and the dotted horizontal line shows the fraction (number) of LISA detections that satisfies this requirement.

We compute the respective error as

$$\frac{\sigma_{\rm GW}}{d_{\rm GW}} \simeq \left[\left(\frac{\sigma_A}{A}\right)^2 + \left(\frac{3\sigma_f}{f}\right)^2 + \left(\frac{\sigma_{\dot{f}}}{\dot{f}}\right)^2\right]^{1/2}, \tag{5.17}$$

where $\sigma_A/A, \sigma_f/f$ and $\sigma_{\dot{f}}/\dot{f}$ are the diagonal elements of the covariance matrix provided by the MLDC pipeline (see Appendix B for a more detailed description). We verify that the terms containing correlation coefficients are at most of the order of 1%, and we thus neglect them in equation (5.17).

The cumulative distribution (and total number) of the relative errors of the distance is represented in Fig. 5.4. Out of 2.6×10^4 binaries individually resolved by LISA only 30% of the catalogue has relative distance errors of less than 30%, which nevertheless provides a sample of 7.8×10^3 DWDs. In particular, a subsample of ~ 100 DWDs (0.4% of all resolved binaries) has relative errors on the distance of less than 1%. These sources have high frequencies (> 3 mHz) and high SNR (> 100), and are located between 1 and 13 kpc from the Sun. This remarkable precision is due to the fact that GW SNRs decrease much more slowly with distance compared to EM observations, and it is at the heart of the unique ability of the LISA mission to study the Milky Way's structure. The red solid line in Fig. 5.4 represents the sky localisation error, $\Delta\Omega = 2\pi\sigma_\theta\sigma_\phi\sqrt{1-\rho^2_{\theta\phi}}$ where $\rho_{\theta\phi}$ is the correlation coefficient between θ and ϕ (e.g Lang & Hughes, 2008), and shows that about half of all DWDs can be located to within better than 10 deg^2 on the sky, with a maximum error in the whole sample of ~ 100 deg^2.

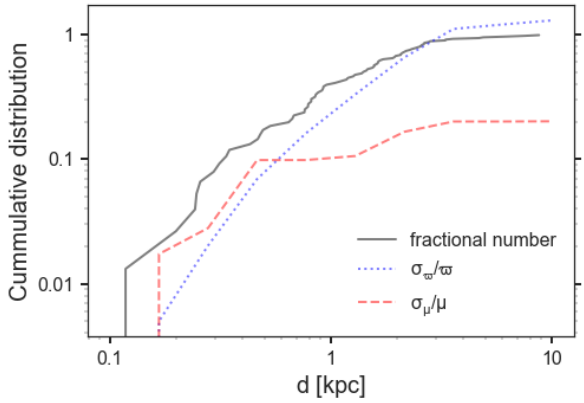

Figure 5.5: Cumulative distribution of the LISA EM counterparts detected either by *Gaia* or the LSST (grey solid line), and their median relative error in parallax (blue dotted line) and proper motion (red dashed line) as a function on the distance from us. For those DWDs that are detected by both *Gaia* and the LSST we select the measurement with smaller uncertainty.

5.3.2 Distances from parallaxes

To simulate the measurement of the parallax ϖ for each optically detected DWD in our catalogue, we draw ϖ from a Gaussian distribution centred on $1/d$ and with standard deviation σ_ϖ. The *Gaia* end-of-mission parallax error σ_ϖ is given by (Gaia Collaboration et al., 2016)

$$\sigma_\varpi = \Pi(-1.631 + 680.766z + 32.732z^2)^{1/2} \times \\ [0.986 + (1 - 0.986)\Delta(V - I)]\,, \tag{5.18}$$

where $z = \max[100.4(12.09 - 15), 100.4(G - 15)]$, $V - I$ is the colour of the object in the Johnson-Cousins system, and Π is a numerical factor that takes into account the Ecliptic latitude of the source and the number of transits of the satellite at that latitude[4]. To transform the colours of DWDs in our mock catalogue from the Sloan *ugriz* to the Johnson-Cousins UBVRI system, we use the empirical colour transformations from Jordi et al. (2006). We also calculate the end-of-mission errors on the proper motion (σ_μ), which can be obtained by re-scaling σ_ϖ by a factor 0.526 (Gaia Collaboration et al., 2018). Note that we use the end-of-mission errors. To re-scale the errors for a different observation time one needs to multiply σ_ϖ by $(T_{\rm tot}/T_{\rm obs})^{0.5}$, where $T_{\rm tot}$ is the total *Gaia* mission mission life time and $T_{\rm obs}$ is the effective observation time, both expressed in month (Gaia Collaboration et al., 2018). For example, for the second *Gaia* data release this factor is $\sim (60/21)^{0.5}$. For proper motion errors the scaling factor is $(T_{\rm tot}/T_{\rm obs})^{1.5}$.

We estimate the accuracy of the LSST astrometric measurements by interpolating Table 3.3 of LSST Science Collaboration et al. (2009). In the following, for the EM counterparts that can be detected by both *Gaia* and LSST, we utilise the measurement of the parallax and proper motion with the smaller error.

[4]Tabulated values for Π can be found at:
https://www.cosmos.esa.int/web/Gaia/table-2-with-ascii

In Fig. 5.5, we represent the cumulative distribution of the LISA EM counterparts (in grey), and that of their median relative error in parallax (in blue) and proper motion (in red) as a function of distance. For binaries at $d < 1\,\mathrm{kpc}$ the expected relative error in parallax is $< 20\%$. These binaries constitute 30% of the EM catalogue and consists mainly of *Gaia* measurements (see Fig. 5.6). Beyond $1 - 2\,\mathrm{kpc}$ all measurements are provided by the LSST. Although the median relative errors in parallax are larger, the LSST data is crucial in providing EM measurements out to 10 kpc. Forecasting the proper motion measurements, we show that the relative errors will be $< 20\%$ at all distances.

Different authors have stressed that to correctly estimate distances from parallaxes a probability-based inference approach is necessary (e.g. Astraatmadja & Bailer-Jones, 2016; Bailer-Jones, 2015; Bailer-Jones et al., 2018; Luri et al., 2018, for *Gaia* measurements). Essentially, because the measurement of ϖ is affected by uncertainties, one can only infer the distance in a probabilistic sense by making an assumption on the true distribution of DWDs in space (the prior distribution). Using Bayes' theorem, the posterior probability density of the possible values of d_{EM} can be expressed as

$$P(d_{\mathrm{EM}}|\varpi, \sigma_\varpi) = \frac{1}{Z} P(\varpi|d_{\mathrm{EM}}, \sigma_\varpi) P(d_{\mathrm{EM}}), \tag{5.19}$$

where Z is a normalisation constant, $P(\varpi|d_{\mathrm{EM}}, \sigma_\varpi)$ is the likelihood that describes the noise model of the instrument and $P(d_{\mathrm{EM}})$ is the prior. We assume that the likelihood is Gaussian (e.g. Luri et al., 2018). For measurements with relative errors on parallax $\sigma_\varpi/\varpi < 0.2$, the distance estimates are mainly independent of the choice of the prior. However, for larger relative errors the quality of the estimates depends on how well the prior describes the true distribution of distances of the observed sources. In our sample we expect the choice of the prior to become crucial at $d > 1\,\mathrm{kpc}$. For this work we adopt a simple exponentially decreasing volume density prior, described by only one parameter L, the scale length. In this paper we assume $L = 400\,\mathrm{pc}$ as in Kupfer et al. (2018), and we fine-tuned this value by using our mock population to derive distances for LISA verification binaries using parallax measurements from the *Gaia* Data release 2. We associate the most probable value of d_{EM} with the mode of the posterior distribution, because we expect this distribution to be highly asymmetric (e.g. Bailer-Jones, 2015). Finally, we compute the errors as $\sigma_{\mathrm{EM}} = (d_{95} - d_5)/2s$, where d_{95} and d_5 are the boundaries of the 90% credible interval of the posterior distribution and $s = 1.645$[5] (Bailer-Jones, 2015). The result is represented in blue in the top panel of Fig. 5.6. It is evident that distances inferred from parallaxes follow the dashed line $d_{\mathrm{obs}} = d$ up to $\sim 1 - 2\,\mathrm{kpc}$, while beyond that the estimated distances systematically start to underestimate the true values. This is due to the large parallax errors combined with our choice for the prior. However, for these binaries more precise distances can be derived using additional information from GWs.

5.3.3 Combining GW and EM measurements

For DWDs with EM counterparts, we can use the additional information from EM observations to improve GW estimates. Again, this can be done by using Bayes' theorem. We model the GW posterior distribution for the distance as a Gaussian centred on the distance inferred from GWs, d_{GW}, with a standard deviation equal to

[5] s is the ratio of the 90% to 68.3% credible intervals for a Gaussian distribution.

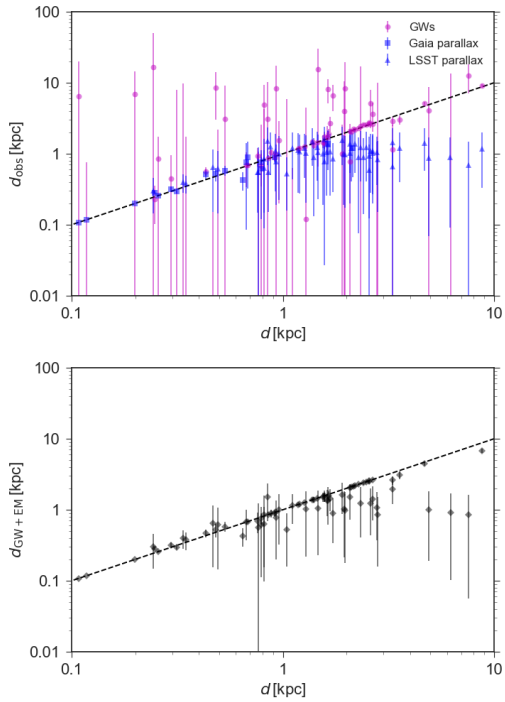

Figure 5.6: In the left panel: observed distance as a function of the true distance to the DWD, d. We indicate with $d_{\rm obs}$ the distance estimated either from GWs (in magenta) or from parallax (in blue). We denote distances estimated respectively from *Gaia* and LSST measurements with triangles and squares. The dashed line shows where $d_{\rm obs} = d$. In the right panel: distance estimates obtained by combining GW and EM measurements through Bayes theorem.

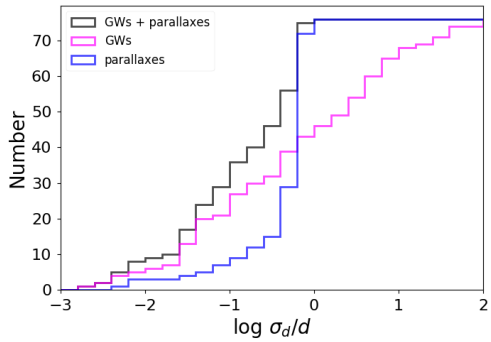

Figure 5.7: The distribution of relative errors on the distance, estimated from GW observations (magenta), from optical observations (blue) and from the combination of the two measurements (hatched).

$\sigma_{\rm GW}$ (computed from the FIM, Γ, as described in Sect. 5.3.1). Likewise, we model the EM posteriors as a Gaussian centred on the distance inferred from the parallax, $d_{\rm EM}$, with a standard deviation equal to the corresponding error $\sigma_{\rm EM}$. The joint posterior distribution is given by the product of these two Gaussian distributions. This can be understood from Bayes' theorem, by noting that the GW and EM observations are independent, and by using the GW posteriors as priors for the EM inference (or vice versa). The resulting distribution is again Gaussian with mean equal to the sum of the individual means weighted by their standard deviations,

$$d_{\rm GW+EM} = \frac{d_{\rm GW}\sigma^2_{\rm EM} + d_{\rm EM}\sigma^2_{\rm GW}}{\sigma^2_{\rm EM} + \sigma^2_{\rm GW}}, \tag{5.20}$$

and a standard deviation equal to twice the harmonic mean of the individual standard deviations,

$$\sigma_{\rm GW+EM} = \sqrt{\frac{\sigma^2_{\rm EM}\sigma^2_{\rm GW}}{\sigma^2_{\rm EM} + \sigma^2_{\rm GW}}}. \tag{5.21}$$

The result is represented in the right panel of Fig. 5.6. Comparing the top and bottom panels, it is evident that with this procedure we essentially select the best of the two measurements. Moreover, we also reduce the uncertainties compared to just selecting the more precise of the EM or GW measurements individually. Indeed, in Fig. 5.7 we show that by combining EM and GW data one can significantly improve the fractional errors on the distance, thus making it possible to use joint GW and EM detections to study Galactic kinematics, as we show in Section 5.5.

5.4 Radial and vertical density profiles of LISA detections

The distance and the sky localisation from LISA measurements allow one to construct density maps of DWDs in the Galaxy. Figure 5.3 suggests that LISA has the potential to reconstruct the density profiles of both the disc and bulge components and derive their scale lengths. In this section we quantify how well we can recover the scale parameters of the Milky Way using DWDs.

We define a Cartesian Galactocentric reference frame (X, Y, Z) such that the Galactic disc lies on the (X, Y) plane, and the Sun lies on the positive Y-axis in the Galactic plane (see also Fig. 5.10). In this reference frame, the position of an object with Galactic coordinates (l, b) at a distance d from the Sun is defined by the set of coordinates:

$$\begin{aligned} X &= d\sin l\cos b, \\ Y &= R_0 - d\cos l\cos b, \\ Z &= d\sin b. \end{aligned} \tag{5.22}$$

In addition, we define a cylindrical coordinate system about the Galactic centre as

$$\begin{aligned} R &= \sqrt{X^2 + Y^2}, \\ \theta &= \arctan\frac{Y}{X}, \\ Z &= d\sin b. \end{aligned} \tag{5.23}$$

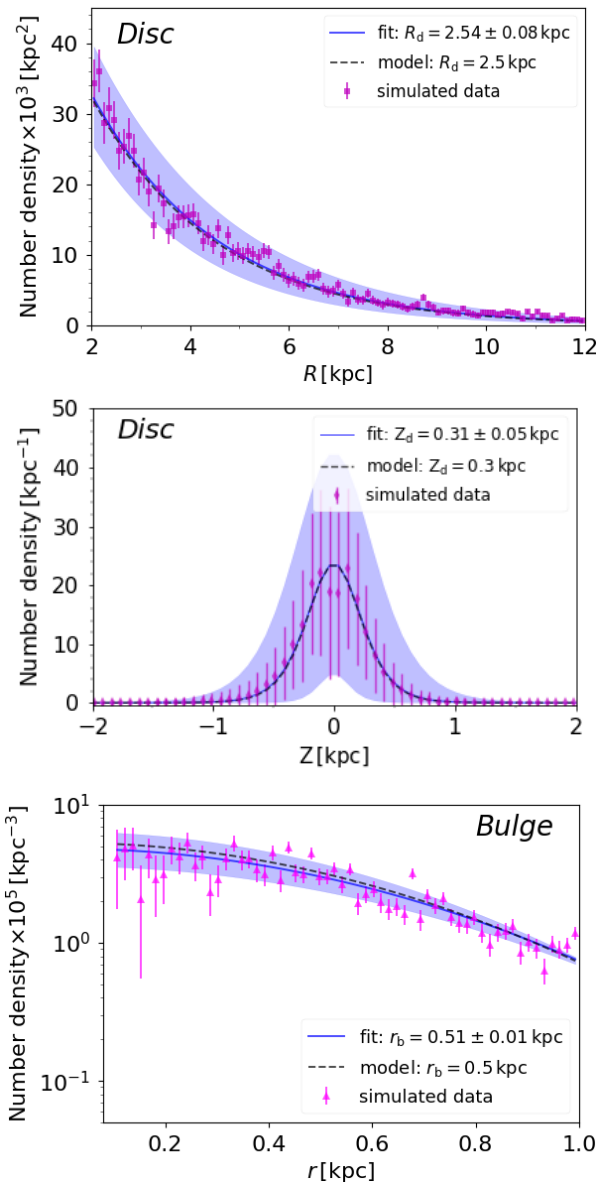

Figure 5.8: Number density profiles for the DWDs detected by LISA as a function of cylindrical radius R (top panel), height above the Galactic plane Z (middle panel), and spherical radius r from the Galactic centre (bottom panel). Magenta points represent one of 10^5 realisation of the LISA observations that we performed to compute the error bars. The blue solid line shows the best fit model and the blue shaded area shows its 3σ uncertainty region. The dashed grey line shows the true number density.

We select the subsample of LISA detections with relative error in distance $< 30\%$. This leaves us with $\sim 8 \times 10^3$ DWDs (30% of all the binaries detected by LISA). To compute the radial density profile, we first derive 10^5 realisations of the 3D binary positions in the Galaxy by randomly drawing l, b and d from Gaussian distributions[6] centred on their true values and with standard deviations computed in Sect. 5.3. For each realisation we compute the cylindrical Galactocentric distance, R, and we select sources with $2 \leq R \leq 12\,\mathrm{kpc}$. The lower limit of the interval in R is motivated by the number density maps represented in Fig. 5.3, which show a spherical central population in the inner $\sim 2\,\mathrm{kpc}$, which we identify with the bulge. The upper limit is motivated by the poor statistics at $R > 12\,\mathrm{kpc}$, as can be seen in Fig. 5.3. Next, we count the number of DWDs in cylindrical shells of width $dR = 0.125\,\mathrm{kpc}$, dividing by the shell volume and accounting for the bias (Appendix C). We compute the error on the number density in each bin as the standard deviation over different realisations. We represent one of the data realisations by the square symbols in the upper panel of Fig. 5.8 (upper panel). We fit the scale radius R_d and the normalisation with PyMC3[7], using an exponential profile (equation (5.1)). The blue solid curve in the top panel of Fig. 5.8 shows the best fit model, and the coloured area shows its 3σ interval. Our best fit value for the disc scale radius is $R_\mathrm{d} = 2.54 \pm 0.08\,\mathrm{kpc}$, in agreement with the fiducial value of 2.5 kpc that we use to generate the Galaxy. Thus, LISA can recover the disc scale radius with $\sim 3\%$ precision.

To study the vertical distribution of DWDs in the disc, we select binaries with $2 \leq R \leq 12\,\mathrm{kpc}$. First, we bin them in concentric cylindrical rings with a step of 0.125 kpc in the radial direction and 0.05 kpc in the vertical direction. Next, we divide the bin counts by the bin volume $2\pi R dR dZ$. In each radial bin, we model the number density with a $\mathrm{sech}^2(Z/Z_\mathrm{d})$ function and fit Z_d to test whether the scale height is constant with R or the vertical distribution of DWDs has a more complex structure. We find a constant behaviour and therefore we decide to increase the statistics by computing the average value of Z_d and its error on a stacked radial profile. In this way, we find $Z_\mathrm{d} = 0.31 \pm 0.05\,\mathrm{kpc}$, which is consistent with the fiducial value of 0.3 kpc.

Finally, to estimate the scale radius of the bulge we select DWDs in the inner 1.2 kpc to avoid disc contamination. Again, we compute 10^5 realisation of the binary positions in the Galaxy by randomly drawing l, b and d for each source. For each realisation, we estimate the number density profile by counting DWDs in spherical shells with radius $r = \sqrt{X^2 + Y^2 + Z^2}$ and $dr = 15\,\mathrm{pc}$, dividing this number by the shell volume and correcting for the bias (Appendix C). Finally, we estimate the error in each bin as the standard deviation over all the realisations. The result is given by the magenta triangles in the bottom panel of Fig. 5.8. To fit the scale radius of the bulge, we use equation (5.2) as the model distribution, and we obtain $r_\mathrm{b} = 0.51 \pm 0.013\,\mathrm{kpc}$. Again, this result is in excellent agreement with the fiducial value of 0.5 kpc.

[6] We consider the three Gaussian distributions independent because the correlation coefficients between d, θ and ϕ are negligible: $\rho_{\mathrm{d}\theta}, \rho_{\mathrm{d}\phi} \leq 0.1$ and $\rho_{\theta\phi} < 0.3$ in our catalogue.

[7] PyMC3 is an open source python package for Bayesian statistical modelling and probabilistic machine learning (Coyle, 2016).

5.4.1 Model comparison for the disc radial density profile

Heretofore, we have tested how well the simulated GW data trace the underlying density distribution (i.e. the true model). In this Section we assess whether the simulated data allow us to discriminate between the true disc surface density distribution and a model with a different functional form.

We consider a Kuzmin disc (Kuzmin 1956, Toomre, 1963), whose surface density distribution scales as a power law:

$$\Sigma_{\rm K}(R) = \frac{M_{\rm d}}{2\pi(R^2 + R_{\rm K}^2)^{3/2}} \ \ {\rm M}_\odot\,{\rm kpc}^{-2}, \tag{5.24}$$

where $M_{\rm d}$ is the mass of the disc and $R_{\rm K}$ is the model's radial scale parameter. Unlike our "true" disc model, whose surface density profile decays exponentially with R, equation (5.24) yields $\Sigma_{\rm K}(R) \propto R^{-3}$ at large R. Thus, we expect the two models to differ significantly at least at large R.

We fit the simulated data with equation (5.24), and obtain $R_{\rm K} = 3.86 \pm 0.09\,{\rm kpc}$. We show in Fig. 5.9 a comparison between the best fit to the Kuzmin model (in red) and the best fit to the exponential disc model (in blue). This figure reveals that the two models are indistinguishable inside the Solar Galactocentric radius, and start differing beyond that radius. Therefore, to distinguish between these two models data far out in the disc are needed, which GW detections can provide (magenta circles in Fig. 5.9)

We therefore compare the two models using the Widely-applicable Information Criterion (WAIC), which provides a fit measure for Bayesian models and which can be applied when the parameter estimation is done using numerical techniques (Watanabe 2010). The WAIC is defined as

$$WAIC = -2\ (LPPD - \bar{P}), \tag{5.25}$$

where $LPPD$ is the log posterior predictive density, and $\bar{P}$ is an estimate of the effective number of free parameters in the model, which can be interpreted as a penalty term adjusting for over-fitting[8]. By definition, lower values of the WAIC indicate a better fit, i.e the WAIC measures the "poorness" of the fit. We compute the WAIC ($\bar{P}$) with PyMC3, obtaining 895 (2.12) and 1017 (4.6) for the exponential and Kuzmin disc models respectively (see bottom panel of Fig. 5.9). There is no set threshold for the difference in WAIC, but typically a difference of 10 or more suggests that the model with higher WAIC is likely to perform worse. Thus, in our case, the Kuzmin disc model is more "flexible" with respect to the data, but its predictive power is worse than the exponential disc model. Furthermore, the error on the WAIC (the expected predictive error) is also larger for the Kuzmin disc (Fig. 5.9). These factors reveal a preference for the correct exponential disc model.

[8] A higher value of $\bar{P}$ indicates that the model is the more "flexible" of the two at fitting the data.

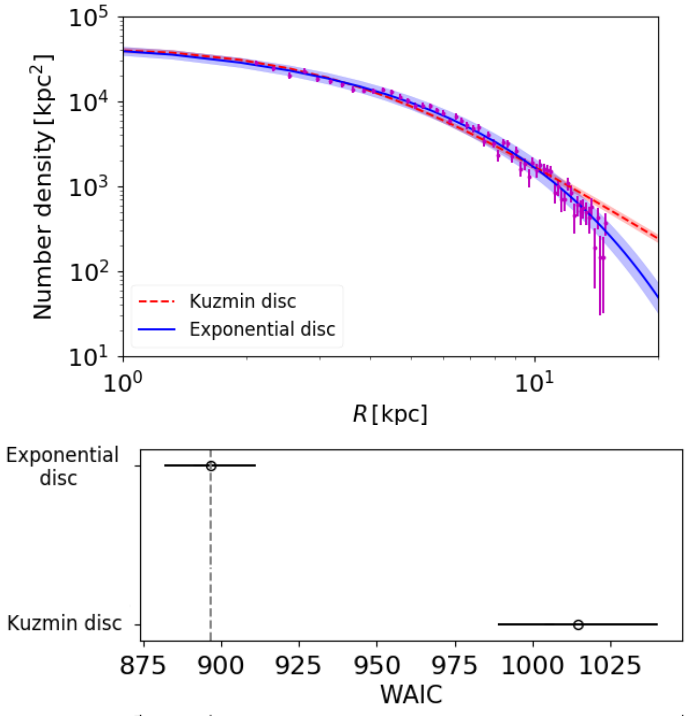

Figure 5.9: The top panel shows number density profiles for the exponential and Kuzmin disc models as a function of R: magenta points represent simulated data like in Fig. 5.8, blue solid and red dashed lines show the best fits for the exponential disc and Kuzmin disc models respectively, and the shaded areas define 3σ uncertainties. The bottom panel shows a comparison between the two models in terms of the WAIC criterion: empty circles represent the WAIC value, and the black error bars are the associated errors computed using PyMC3; the vertical dashed line marks the preferred model.

5.5 Kinematics of DWDs

In the previous Section we have shown that one can recover the shape of the baryonic components of the Galaxy from GW observations alone, but EM counterparts are required to study the dynamics of the Galaxy. Around 80 DWD EM counterparts to LISA detections can be observed with *Gaia* and the LSST through their eclipses (Sect. 5.2.5). We estimate that both *Gaia* and the LSST will deliver proper motions with relative precision $< 20\%$ for these binaries. However, it will be hard to have 3D velocities without a spectroscopic follow-up of these sources. DWDs are too faint to measure their radial velocities with the Radial Velocity Spectrometer (RVS) on board of the *Gaia* satellite and, moreover, they are typically featureless in the RVS wavelength range (Carrasco et al., 2014). Nonetheless, the rotation speed of DWD EM counterparts around the Galaxy can be computed from proper motions alone (e.g., Sofue, 2017). In this section we describe how we model DWD velocities, and we derive the rotation curve for our mock Galaxy using distances estimated from GW observations as well as proper motions simulating *Gaia* and the LSST observations.

5.5.1 Kinematic model

Figure 5.10 sketches the geometry of the problem: a DWD at a distance d from the Sun and at Galactic latitude l is moving along a circular orbit in the Galactic plane, with Galactocentric radius R. In the Cartesian coordinate system defined by the coordinate transformation of equation (5.22), the position vector of the binary can be expressed as

$$\mathbf{R} = \begin{pmatrix} R\sin\theta \\ R\cos\theta \end{pmatrix} = \begin{pmatrix} d\sin l \\ R_0 - d\cos l \end{pmatrix}, \tag{5.26}$$

where θ is the angle between the Sun and the DWD as seen from the Galactic centre. By equating the two expressions for the components of $\mathbf{R}$, one obtains $\sin\theta = d\sin l/R$ and $\cos\theta = (R_0 - d\cos l)/R$. Thus, we can write the azimuthal velocity as

$$\mathbf{V} = V(R)\begin{pmatrix} \cos\theta \\ -\sin\theta \end{pmatrix} = V(R)\begin{pmatrix} \frac{R_0}{R} - \frac{d}{R}\cos l \\ -\frac{d}{R}\sin l \end{pmatrix}, \tag{5.27}$$

In practice, we assign a value of $V(R)$ to a source by randomly drawing from a Gaussian centred on the value given by the rotation curve at that R and dispersion given by equation (5.7). If we neglect the peculiar motion of the Sun and assume that its velocity in the Galactic plane is $\mathbf{V}_\odot = (V_0, 0)$, we can write the relative velocity between the DWD and the Sun as

$$\Delta\mathbf{V} = \mathbf{V} - \mathbf{V}_0 = \begin{pmatrix} R_0(\Omega(R) - \Omega_0) - \Omega(R)d\cos l - \Omega(R)d \\ -\Omega(R)d\sin l \end{pmatrix}, \tag{5.28}$$

where $\Omega(R) = V(R)/R$ and $\Omega_0 = V_0/R_0$ are the angular velocities of the DWD and of the Sun, respectively. Then, the tangential component can be found by projecting $\Delta\mathbf{V}$ along the line of sight and along the direction perpendicular to it:

$$V_\mathrm{t} = \Delta\mathbf{V}\begin{pmatrix} \cos l \\ \sin l \end{pmatrix} = [\Omega(R) - \Omega_0]\, R_0\cos l - \Omega(R)d. \tag{5.29}$$

The proper motions of DWDs can be estimated as

$$\mu = \frac{V_\mathrm{t}}{4.74\ d} \qquad \text{arcsec yr}^{-1}, \tag{5.30}$$

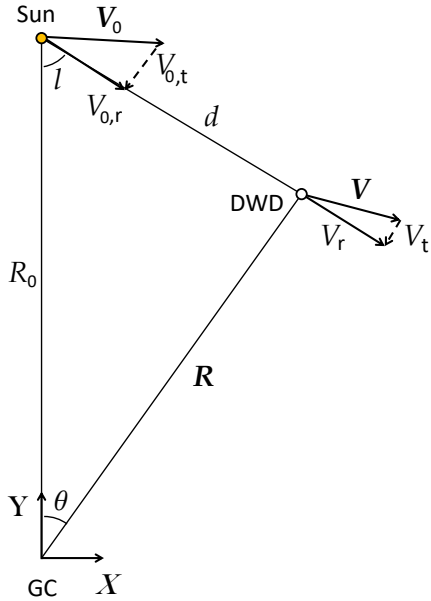

Figure 5.10: Kinematic model for DWDs. GC stands for Galactic centre.

where d is in pc and V_t is in km/s.

To simulate *Gaia* and LSST measurements of DWD proper motions, we assign an observed proper motion μ_{obs} to a source by sampling from a Gaussian centred on μ with an error σ_μ given by the instrument response (see Sect. 5.2.5). Similarly we sample the observed distances from a Gaussian centred on d_{GW+EM} with an error σ_{GW+EM} (see Sect. 5.3.3). To compute the observed rotation speed we combine the simulated measurements according to

$$V_{obs}(R) = -\frac{R}{d_{obs} - R_0 \cos l}\,(4.74\mu_{obs}d_{obs} + V_0 \cos l) \qquad \text{km s}^{-1}. \tag{5.31}$$

For each DWD, we calculate $V_{obs}(R)$ for 10^5 independent realisations of μ_{obs} and d_{obs}, and we assign an observed velocity and measurement error equal respectively to the mean and the standard deviation of the resulting distribution of $V_{obs}(R)$. The result is represented in Fig. 5.11. Because *Gaia* and LSST can probe only relatively close distances, the rotation curve derived here can provide information only on the local Galactic properties. However, the one observation point that we have close to the Galactic centre provides good constraints on the parameters describing the bulge component, as we show in the following.

5.5.2 Doppler effect due to motion in the Galaxy

In this Section, we calculate the line of sight projection of the velocity, V_r, which for DWDs will not be observed by *Gaia* and/or LSST, but which will directly influence the GW observables, as we explain below.

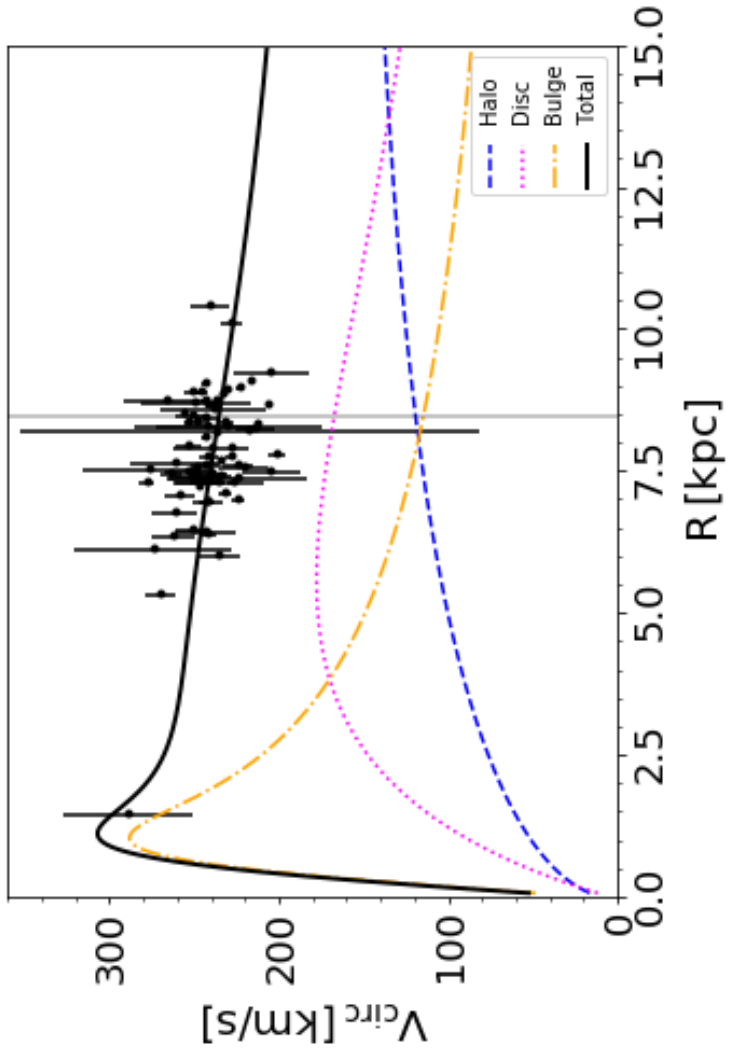

Figure 5.11: Rotation speed of DWDs with EM counterpart computed according to equation (5.31). The black solid curve shows the model's rotation curve. Coloured lines represent the contributions of different Galactic components to the total rotation curve: the colour coding is the same as in Fig. 5.2. The vertical line marks the position of the Sun.

The motion of the stars in the Galaxy introduces a Doppler shift in the GW frequency, so that the observed frequency is

$$f_{\rm obs} \approx \frac{f}{1+\frac{V_{\rm r}}{c}}, \tag{5.32}$$

where $V_{\rm r}$ can be computed by projecting $\mathbf{V}$ along the line of sight, i.e.

$$V_{\rm r} = \Delta\mathbf{V}\begin{pmatrix}\sin l\\ -\cos l\end{pmatrix} = [\Omega(R)-\Omega_0]\,R_0\sin l. \tag{5.33}$$

The relation between time intervals at the detector and at the source is

$$dt_{\rm obs} \approx \left(1+\frac{V_{\rm r}}{c}\right)dt. \tag{5.34}$$

By deriving equation (5.32) with respect of time and using equation (5.34) to express the result in terms of the observed frequency we obtain

$$\dot{f}_{\rm obs} = \frac{96}{5}\pi^{8/3}\left[\frac{G\mathcal{M}(1+V_{\rm r}/c)}{c^3}\right]^{5/3} f_{\rm obs}^{11/3} + \frac{\dot{V}_r}{c} f_{\rm obs} \tag{5.35}$$

and the GW amplitude as

$$A = \frac{5}{96\pi^2}\frac{\dot{f}_{\rm obs}}{f_{\rm obs}^3 d(1+V_{\rm r}/c)}. \tag{5.36}$$

There are two additional terms in equation (5.35) compared to the original equation (5.12): the Doppler term containing $V_{\rm r}/c$ and the acceleration term $\dot{f}_{\rm acc} = f_{\rm obs}\dot{V}_r/c$.

First, we focus on the Doppler term. In the first term of equation. (5.35) we can replace the chirp mass with the Doppler-shifted chirp mass $\mathcal{M}(1+V_{\rm r}/c)$. Similarly, the Euclidean distance d in equation (5.36) can be replaced with the luminosity distance $d(1+V_{\rm r}/c)$[9]. This is similar to what happens for cosmological sources, for which the chirp mass gets "redshifted" (i.e. multiplied by a factor $1+z$, z being the redshift), the frequency at the source gets replaced by the detector-frame one, and the co-moving distance is replaced by the luminosity distance. The radial velocities of DWDs as seen from the Sun are expected to be from a few to a few tenths km/s, meaning that $V_{\rm r}/c \sim 10^{-5} - 10^{-4}$.

Next, we estimate the acceleration term $\dot{f}_{\rm acc}$. Assuming that the total velocity of a DWD (relative to the observer) is constant, we can express $\dot{V}_r$ in terms of $V_{\rm t}$ as $\dot{V}_{\rm r} = V_{\rm t}^2/d$. For a DWD with a typical frequency of 1 mHz, tangential velocity of 10 km/s and distance of 1 kpc, we obtain $\dot{f}_{\rm acc} \sim 10^{-23}\,{\rm s}^{-2}$, meaning that the contribution of the acceleration term is $\dot{f}_{\rm acc}/\dot{f}_{\rm obs} \sim 10^{-5} - 10^{-4}$, thus comparable to the Doppler term. The same applies to all periodic phenomena, and has long been known in classical astronomy as "secular acceleration" or "Shklovsky effect" in pulsar timing (e.g., Pajdosz, 1995; Shklovskii, 1970).

[9]Note that in the presence of a Doppler shift, the luminosity distance – i.e. the ratio $L/(4\pi F)$, L being the intrinsic source luminosity and F being the energy flux at the detector – differs from the Euclidean distance d, because energies are red-(blue-) shifted and times are dilated (contracted).

In general, both the acceleration and the Doppler terms are too small to influence LISA's measurements. However, Shah & Nelemans (2014) have shown that for DWDs with high frequencies and high SNRs, $\sigma_{\dot{f}}/\dot{f}$ can be determined with accuracy up to $10^{-4} - 10^{-5}$, i.e. of the same order of magnitude as the two effects discussed here. Consequently, for these high frequency binaries the systematic errors on $\dot{f}$ (and thus on the distance) due to the motion in the Galaxy can be $\sim 10\%$. We do not take this into account in the present work, but we suggest that when estimating parameters for high frequency binaries, the Doppler effect and the acceleration term due to the motion in the Galaxy can introduce non-negligible systematic errors.

5.5.3 Rotation curve fitting

Although our model is simpler than more realistic representations of the Milky Way (we do not account e.g. for the spiral arms and the bar), as many as seven parameters are required to fully characterise its rotation curve: $M_\mathrm{b}, r_\mathrm{b}, M_\mathrm{d}, R_\mathrm{d}, Z_\mathrm{d}, \rho_\mathrm{h}$ and r_h. In general, the measurement of the rotation speed alone is not sufficient to derive all the parameters and to break the degeneracies between them. A well known degeneracy is that between disc and halo parameters, i.e. a smooth flat rotation curve, such as the one of the Milky Way, makes the transition from the disc dominated to the DM halo dominated regime very gentle. The measurement of the rotation speed of stars in the Galaxy provides the total enclosed mass at a given radius, but in general that is not enough to break the degeneracy between the mass and the scale radius of the DM halo and disc components. Thus, a global rotation curve fitting requires strong prior assumptions on the scale lengths of the Galactic components.

To obtain the best set of parameters that reproduce our simulated rotation curve (Fig. 5.11), we fix $r_\mathrm{b}, R_\mathrm{d}$ and Z_d to the values obtained by fitting the number density profiles of DWDs, and we fit the remaining parameters using PyMC3. We use as proposal fitting model the rotation curve computed numerically with GALPYNAMICS according to equation(5.5), and we leave $\rho_\mathrm{h}, r_\mathrm{h}, M_\mathrm{d}$ and M_b as free parameters of the model. For all four free parameters, we set flat uninformative priors in the following ranges: M_d and M_b are searched between $(1-10)\times10^{10}\mathrm{M}_\odot$; ρ_0 and r_h between $(0.1-10)\times10^7\,\mathrm{M}_\odot/\mathrm{kpc}^3$ and $10-30\,\mathrm{kpc}$, respectively. At each MCMC step we evaluate the value of the likelihood times the priors by computing the difference between our model and the simulated observations. The final posterior probability distribution of the free parameters is represented in (Fig. 5.11). It shows that DWDs can recover the mass of the disc and bulge components, but not that of the DM halo. This is because there is no data at $R > 11\,\mathrm{kpc}$, where the halo dominates the dynamics in our Milky Way model. We estimate the mass of the disc to be $M_\mathrm{d} = 5.3^{+1.29}_{-1.71} \times 10^{10}\,\mathrm{M}_\odot$ and the mass of the bulge to be $M_\mathrm{b} = 2.49^{+0.44}_{-0.42} \times 10^{10}\,\mathrm{M}_\odot$, in good agreement with our fiducial values. Remarkably, our constraints on the bulge mass are extremely competitive with those derived from EM tracers (see e.g. Bland-Hawthorn & Gerhard, 2016). The larger errors on the disc mass stem from our choice to leave the halo parameters unconstrained.

To test whether our method can provide better constraints on the DM halo component, we performed an additional simulation with a heavier DM halo, which gives a larger contribution to the total rotation speed at the Sun position (where most of the data points lie). Specifically, we performed an additional simulation of DWDs kinematics (as described in Sect. 5.5), in which we assign velocities to LISA optical coun-

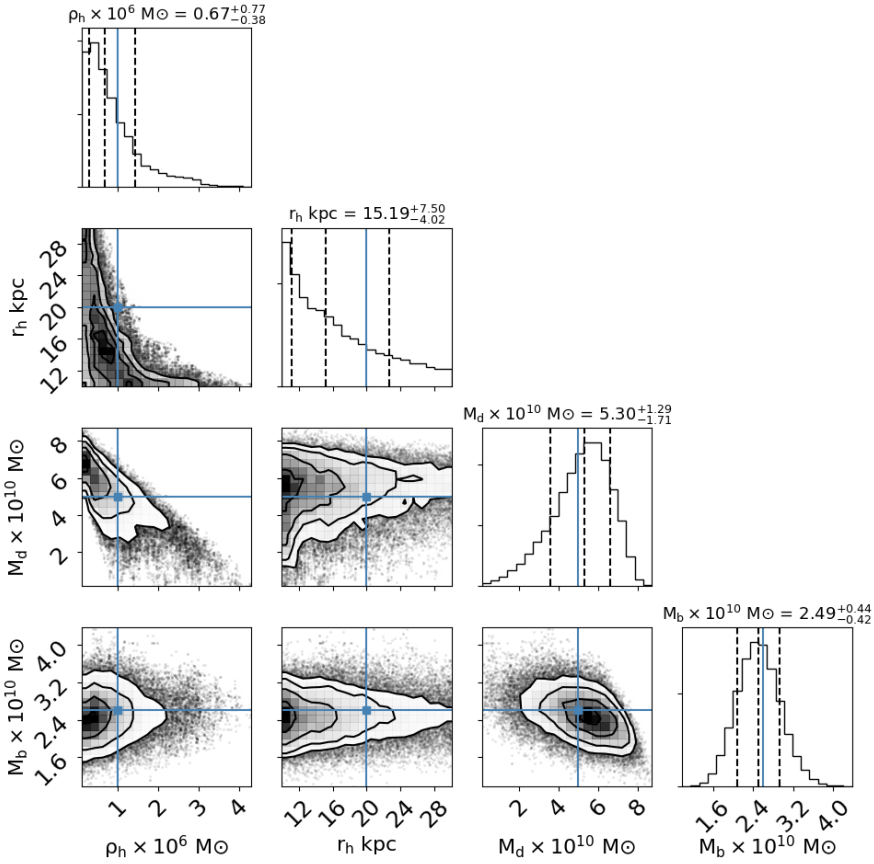

Figure 5.12: The posterior probability distribution of the four free parameters of our rotation curve fitting model, $M_{\rm b}, M_{\rm d}, \rho_h$ and $r_{\rm h}$. Blue lines mark the true values listed in Tab. 5.2.1

terparts using our fiducial Milky Way potential (with scale radius $r_{\rm h} = 20\,{\rm kpc}$), but with $\rho_{\rm h} = 10^7\,{\rm M}_\odot{\rm kpc}^{-3}$. This way the total mass of the DM halo is $M_{\rm h} \simeq 10^{12}\,{\rm M}_\odot$, as found e.g. by Rossi et al. (2017). By performing the same fitting procedure as above, we obtain the posterior probability density distributions for $\rho_{\rm h}, r_{\rm h}, M_{\rm d}$ and $M_{\rm b}$, represented in Fig. 5.13. Again, we obtain $M_{\rm b} = 2.77^{+045}_{-0.43} \times 10^{10}\,{\rm M}_\odot$, which within a 1σ uncertainty recovers the true value of $2.5 \times 10^{10}\,{\rm M}_\odot$. Although with large uncertainties, we can now recover also the true values of the DM halo parameters, $\rho_{\rm h}$ and $r_{\rm h}$. However, by comparing Fig. 5.12 and 5.13, it is evident that this degrades the uncertainty on the disc mass by a factor of ~ 1.5, highlighting the degeneracy between the disc and the halo components. Thus, an improvement of this analysis should involve including additional information from DM halo tracers.

5.6 Conclusions

In this study, we quantitatively investigate for the first time the prospects for tracing the baryonic mass of the Galaxy with a multi-messenger (GW+EM) data analysis using DWD binaries. The advantages over traditional tracers include the possibility of looking through the bulge, and beyond, thus allowing one to map both sides of the Galaxy using the same tracer. We show that this unique property allows one to recover the scale radii of the baryonic components accurately and with percent precision. The abundance of GW detections at large distances will also enable one to disentangle different disc stellar density profiles. Finally, in synergy with optical data, GW measurements will provide competitive mass estimates for the bulge and stellar disc.

Our encouraging analysis, however, needs to be further tested against more realistic Milky Way potentials including, for example, spiral arms and other density asymmetries. One possible way to perform such a test is to use the matter distributions resulting from cosmological simulations of Milky Way like galaxies such as the Eris, APOSTLE and FIRE simulations (Guedes et al., 2011; Hopkins et al., 2018; Sawala et al., 2016). Furthermore, we should also assess the impact of adding observations of AM CVn stars (ultra-compact accreting WDs), which although likely less numerous, may be seen at larger distances in the optical band due to their accretion luminosity.

Finally, our choice to use GW sources and their EM counterparts limits our ability to constrain the DM halo component of Galaxy. This highlights the importance of a more precise knowledge of the DM halo to improve baryonic mass measurements. We therefore envisage that the full potential of our method can be unleashed when more stringent priors on the halo mass from DM tracers will be available after the full exploitation of *Gaia* data (e.g. Contigiani et al., 2018; Posti & Helmi, 2019).

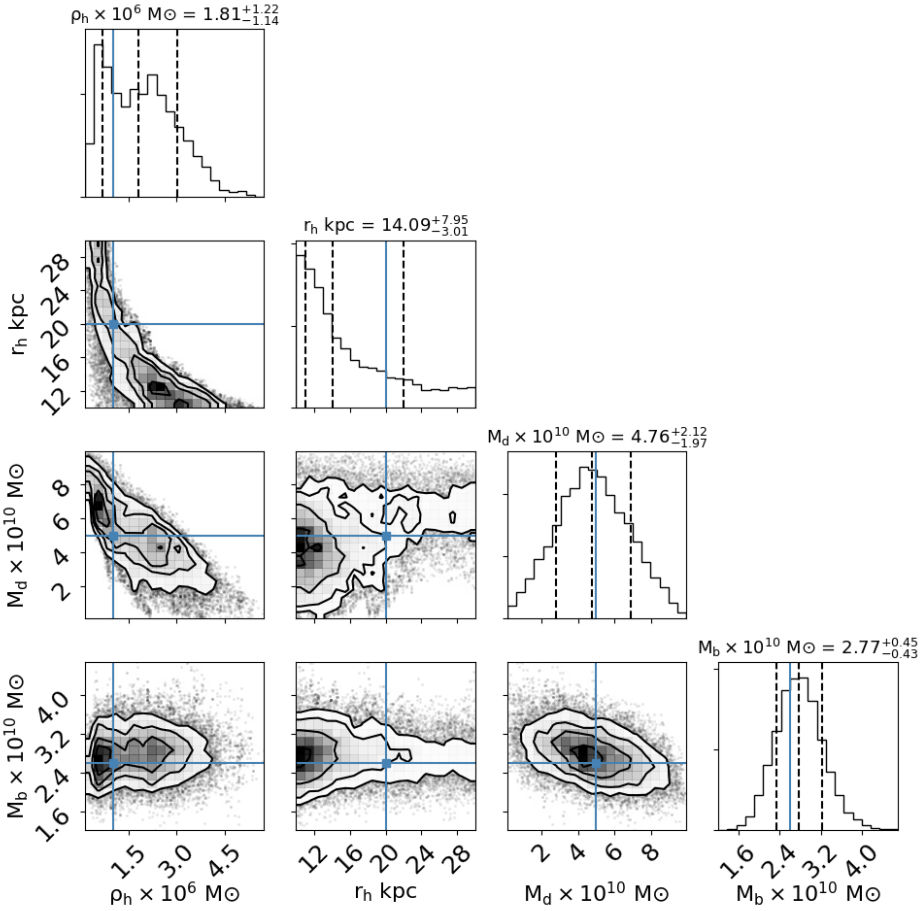

Figure 5.13: The same as in Fig. 5.12, but considering a Galaxy with a heavier DM halo ($M_{\rm h} = 10^{12} {\rm M}_\odot$), so that at the Sun position the disc and the DM halo give comparable contributions to the total rotation curve. This ensures that our simulated observations sample the region of the Galaxy where DM is significant.

Appendix A

How to compute signal-to-noise of GW events

There are important differences between GW and standard astronomy. In electromagnetic observations, in every waveband there are sources so strong that they can be detected even if you know nothing about the source. For example, one does not need to understand nuclear fusion in order to see the Sun. In contrast, most of the expected sources of GW radiation are so weak that we expect that usually sophisticated statistical techniques will be required to detect them. A standard technique involves matching templates of expected waveforms against the observed data stream. Maximum sensitivity therefore requires a certain understanding of what the sources look like, and thus of the characteristics of those sources. To optimise the SNR, which determines the significance of the measurement, we need to apply the theory of signals and systems.

GW radiation has two independent polarisation states + and ×. A general signal can be described as a linear combination of the two polarisation states:

$$h(t) = h_+(t)F_+ + h_\times F_\times. \tag{A.1}$$

The sensitivity of the detector to these depends upon the relative orientation of the source and the detector encoded in the response functions F_+ and $F_\times$. The output of a detector $s(t)$ contains a superposition of noise $n(t)$ and (if present) a signal $h(t)$:

$$s(t) = h(t) + n(t) \tag{A.2}$$

Typically, one expects $h(t) \ll n(t)$, meaning we need advanced methods to filter out the noise. There is a well known procedure in signal processing theory that can be applied to solve this problem called matched filtering (Weiner 1949). Analytically in can be expressed as:

$$\hat{s}(t) = \int_{-\infty}^{+\infty} s(t)K(t)dt, \tag{A.3}$$

where $K(t)$ is a real filter function describing the signal that we are looking for. For simplicity, it is assumed that the noise in the GW detector is stationary and Gaussian (with zero mean), so that the noise is fully characterised by one-sided noise power

spectral density (PDS) $S_n(f)$,

$$\langle \tilde{n}(f)\tilde{n}^*(f')\rangle = \frac{1}{2}\delta(f-f')S_n(f), \tag{A.4}$$

where $\langle ...\rangle$ denote an ensemble average over many noise realisations (Cutler and Flanagan 1994). In reality, one has only one realisation of the event, but for the case of the stationary stochastic noise the ensemble average can be substituted with the time average. The signal-to-noise ration (SNR) can be now defined as S/N, where S is the expected value of $\hat{s}$ when a signal is present, and N the root mean squared value of $\hat{s}$ when signal is absent. Since $\langle n(t)\rangle = 0$, the signal can be evaluated as

$$S = \int_{-\infty}^{+\infty} \langle s(t)\rangle K(K)dt = \int_{-\infty}^{+\infty} h(t)K(t)dt = \int_{-\infty}^{+\infty} \tilde{h}(f)\tilde{K}^*(f)df. \tag{A.5}$$

The last equality was obtained by applying the definition of the Fourier transform

$$\begin{aligned} \tilde{h}(f) &= \int_{-\infty}^{+\infty} h(t)e^{2\pi i f t}dt; \\ h(t) &= \int_{-\infty}^{+\infty} (h)(f)e^{-2\pi i f t}df, \end{aligned} \tag{A.6}$$

and the definition of the convolution of the two functions (for $\tau = 0$)

$$\begin{aligned} (h*K)(\tau) &= \int_{-\infty}^{+\infty} h(t)K(t-\tau)dt = \int_{-\infty}^{+\infty} h(t)\int_{-\infty}^{+\infty} \tilde{K}(f)e^{2\pi i f(t-\tau)}df dt \\ &= \int_{-\infty}^{+\infty} \tilde{K}^*(f)\int_{-\infty}^{+\infty} h(t)e^{2\pi i f t}dt\ e^{-2\pi i f\tau}df = \int_{-\infty}^{+\infty} \tilde{K}^*(f)\tilde{h}(f)e^{-2\pi i f\tau}df. \end{aligned} \tag{A.7}$$

The squared contribution from the noise N^2 is defined as the mean square of the operation defined in equation (A.3) when no signal is present

$$N^2 = \int_{-\infty}^{+\infty} \frac{1}{2}S_{\rm n}(f)|\tilde{K}(f)|^2 df. \tag{A.8}$$

Finally, the ratio between equations (A.5) and (A.8)

$$\mathrm{SNR} = \frac{S}{N} = \frac{\int_{-\infty}^{+\infty} \tilde{h}(f)\tilde{K}^*(f)df}{\left[\int_{-\infty}^{+\infty} \frac{1}{2}S_{\rm n}(f)|\tilde{K}(f)|^2 df\right]^{1/2}} \tag{A.9}$$

To determine the filter K that maximises the above expression, one needs to define the scalar product between two real functions

$$(A|B) = \mathcal{R}\left[\int_{-\infty}^{+\infty} \frac{\tilde{A}^*(f)\tilde{B}(f)}{1/2w(f)}\right] = 4\mathcal{R}\left[\int_0^{+\infty} \frac{\tilde{A}^*(f)\tilde{B}(f)}{w(f)}\right], \tag{A.10}$$

where the second equality holds because both functions $A(t)$ and $B(t)$ are real, and $w(f)$ is a weighting function. By adopting for a weighing function the noise spectral density, S_n, equation (A.9) can be written in the following form

$$\frac{S}{N} = \frac{(u|h)}{(u|u)^{1/2}}, \tag{A.11}$$

where u is a function whose Fourier transform is

$$\tilde{u}(f) = \frac{1}{2} S_{\rm n}(f) K(f). \tag{A.12}$$

Since $S_{\rm n}(f) > 0$, the scalar product is also positive definite, so it can be seen as "inner product" on a "vector space" and we are thus searching for the "vector" $u/(u|u)^{1/2}$ such that its scalar product with h is maximum, meaning we want h and $u/(u|u)^{1/2}$ to be parallel, so:

$$\tilde{K}(f) = C \frac{\tilde{h}(f)}{S_{\rm n}(f)}, \tag{A.13}$$

where C is a constant, which can be left out of the calculation because re-scaling $\hat{s}$ does not change the SNR. Using this filter, we get that:

$$\left(\frac{S}{N}\right)^2 = 4 \int_0^\infty \frac{|\tilde{h}(f)|^2}{S_{\rm n}(f)} df. \tag{A.14}$$

Thus, in order to construct the optimal filter, it is necessary to know a priori the form of the signal $\tilde{h}(f)$.

Appendix B

Fisher Information Matrix

The measurement precision of the parameters describing the waveform can be forecast by computing the FIM, commonly denoted by Γ (e.g. Cutler, 1998; Shah et al., 2012). The GW waveform produced by a DWD can be characterised by 9 parameters: $A, f, \dot{f}, \ddot{f}, \theta, \phi, i, \psi$ and ϕ_0, thus Γ is a 9×9 matrix. The components of Γ can be computed as

$$\Gamma_{ij} = \frac{2}{S_n(f)} \sum_{\alpha=I,II} \int_0^{T_{\rm obs}} dt\ \partial_i h(t) \partial_j h(t), \tag{B.1}$$

where we assume that for a quasi-monochromatic source the noise power spectral density at the binary GW frequency, $S_n(f)$, is constant over the lifetime of the LISA mission and $\alpha = I, II$ are the two independent two-arm detectors of the LISA current design (e.g. Cutler, 1998; Seto, 2002; Takahashi & Seto, 2002). We adopt the noise power spectral density $S_n(f)$ from Amaro-Seoane et al. (2017). The inverse of the FIM is the covariance matrix, C. The diagonal elements of the covariance matrix represent squared σ parameter uncertainties, while the off-diagonal elements give the covariances between parameters. To compute the uncertainty on the distance ($\sigma_{\rm GW}$) we first marginalise over the parameters that do not enter the distance determination ($\ddot{f}, \theta, \phi, \psi$ and ϕ_0) by removing the corresponding rows and columns from the covariance matrix. Next, we invert the resulting covariance matrix to obtain a 4×4 FIM in terms of $p = (f, A, i, \dot{f})$ only, and we compute the new FIM in terms of new parameters $p' = (f, d, i, \dot{f})$:

$$\Gamma'_{mn} = \sum_{ij} \frac{\partial p_i}{\partial p'_m} \frac{\partial p_j}{\partial p'_n} \Gamma_{ij}. \tag{B.2}$$

Finally, the second diagonal element of the inverse of Γ' represents $\sigma^2_{\rm GW}$. We verify that the results obtained in this manner are equivalent, within 0.001%, to the approximate expression in equation (5.17). Since equation (5.17) does not account for the correlations between A, f and $\dot{f}$, this excellent agreement must imply that these correlation terms are negligible. We have indeed verified that this is the case. Note that in general $\sigma_{\rm GW}/d_{\rm GW}$ is small for binaries with small $\sigma_{\dot{f}}/\dot{f}$, i.e. whose chirp is larger than the instrument resolution in frequency ($\dot{f}T_{\rm obs} > 1/T_{\rm obs}$). Thus, a precise distance measurement is typically more challenging for DWDs than for e.g. massive black holes, because the former evolve gravitationally more slowly (equation (5.10)) in the observation window and because they have much smaller masses. However, within

the Galaxy, the abundance of DWD binaries is such that we can collect a sizeable sample with good distance determinations.

Appendix C

LISA observation bias

To derive a simplified analytic expression for the LISA observational bias, we assume that all DWD binaries have roughly the same chirp mass. Indeed, the observed distribution of chirp masses is expected to range between 0.2 and $1\,\mathrm{M}_\odot$ (see Korol et al., 2017, fig.12). Under this assumption, the SNR is only a function of distance d and frequency f, and can thus be written as (e.g., Maggiore, 2008):

$$\mathrm{SNR} = K\frac{f^{2/3}\sqrt{T_{\mathrm{obs}}/S_{\mathrm{n}}(f)}}{d} \equiv \frac{\mathcal{R}}{d}, \tag{C.1}$$

where K is a constant that depends on the detector geometry, the sky location of the source, its orientation and chirp mass, and S_{n} is the noise spectral density of the detector. At low frequencies ($10^{-4} - 10^{-2}\,\mathrm{Hz}$) the noise spectral density scales as $S_{\mathrm{n}} \propto 1/f^{\alpha}$ where $\alpha \simeq 4.7$, as obtained by fitting the LISA noise curve from Amaro-Seoane et al. (2017). Therefore, $\mathcal{R} \sim f^{2/3+\alpha/2}$ and

$$\frac{dN}{d\mathcal{R}} = \frac{dN}{df}\frac{df}{d\mathcal{R}} = \mathcal{R}^{-(20+3\alpha)/(4+3\alpha)}, \tag{C.2}$$

where we have used the fact that the number of sources N per frequency interval scales as $dN/df \propto f^{-11/3}$. This follows from assuming that the population is in a steady state, i.e. that DWDs have a uniform distribution in time to merger (e.g. Sesana et al., 2008). By definition, a binary will be detected if observed with $\mathrm{SNR} = \mathcal{R}/d > 7$, so we can compute the LISA detection fraction as[1]

$$w \propto \int_{7d}^{+\infty} \frac{dN}{d\mathcal{R}} d\mathcal{R} \approx F\, d^{-0.9}\,, \tag{C.3}$$

with $F = \mathrm{const}$.

We test this analytic expression using our mock population. We selected binaries with $\mathrm{SNR} > 7$ and bin them in the $R - \theta$ space, and we compare this to the same histogram without the cut in SNR. The ratio between the two histograms represents the LISA detection fraction. Next, we average the detection fractions over θ to express

[1] Note that this expression is valid only at large distances d, because the steady-state distribution $dN/df \propto f^{-11/3}$ and the approximation $S_{\mathrm{n}} \propto 1/f^{\alpha}$ only hold in a limited range of frequencies. This is also obvious from the fact that the detection fraction, w, diverges as $d \to 0$. In practice, however, equation (C.3) reproduces well the results of our simulations.

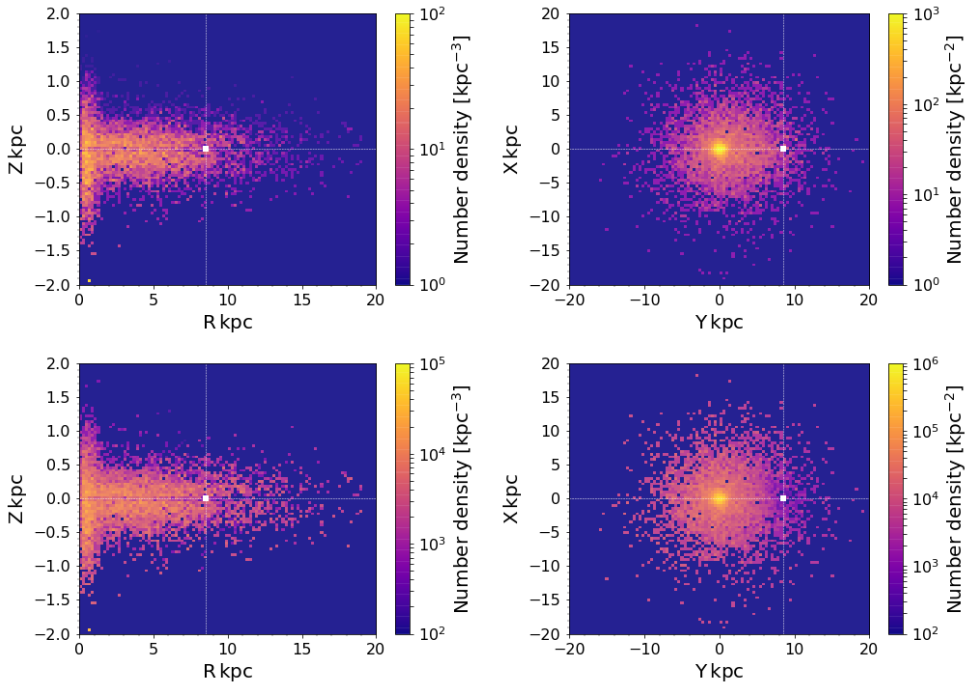

Figure C.1: Top panels: Number density distribution of the DWDs detected by LISA in the Galactic $R-Z$ plane and in the Galactic equatorial plane $X-Y$. Bottom panels: same number density distributions corrected for the observation bias as described in Sect. C. A white square marks the position of the Sun.

them as a function of R only. We then fit the obtained detection fractions with $w = F\, d^{\beta}$, and obtain $F = 0.016 \pm 0.04$ and $\beta = 0.93 \pm 0.04$, consistent with the value in equation (C.3). To show the effect of the correction we compute the surface number density maps of DWDs in the Galactic $X - Y$ and Z_R planes. In the top panels of Fig. C.1 we show DWD density maps not corrected for the bias. In the bottom panels we show the same maps corrected for the bias by assigning a weight w (evaluated using $F = 0.016$ and $\beta = 0.93$) to each bin. The effect of the correction is clearly visible in the bottom right panel of Fig. C.1, where there are fewer sources around the Sun with respect to the upper right panel.

Bibliography

Abbott, B. P., Abbott, R., Abbott, T. D., et al. 2016, Physical Review Letters, 116, 061102

Abbott, B. P., Abbott, R., Abbott, T. D., et al. 2017, Physical Review Letters, 119, 161101

Abbott, B. P., Abbott, R., Abbott, T. D., et al. 2017, Nature, 551, 85

Abt, H. A. 1983, A&A, 21, 343

Adams, M. R., Cornish, N. J., & Littenberg, T. B. 2012, PRD, 86, 124032

Event Horizon Telescope Collaboration, Akiyama, K., Alberdi, A., et al. 2019, ApJL, 875, L1

Alcock, C., Allsman, R. A., Alves, D. R., et al. 2000, ApJ, 542, 281

Althaus, L. G., Miller Bertolami, M. M., & Córsico, A. H. 2013, A&A, 557, A19

Amaro-Seoane, P., Aoudia, S., Babak, S., et al. 2012, Classical and Quantum Gravity, 29, 124016

Amaro-Seoane, P., Audley, H., Babak, S., et al. 2017, arXiv:1702.00786

Armano, M., Audley, H., Auger, G., et al. 2016, Physical Review Letters, 116, 231101

Armano, M., Audley, H., Baird, J., et al. 2018, Physical Review Letters, 120, 061101

Astraatmadja, T. L., & Bailer-Jones, C. A. L. 2016, ApJ, 832, 137

Astropy Collaboration, Robitaille, T. P., Tollerud, E. J., et al. 2013, AAP, 558, A33

Babak, S., Gair, J., Sesana, A., et al. 2017, PhR, 95, 103012

Badenes, C., Mullally, F., Thompson, S. E., & Lupton, R. H. 2009, ApJ, 707, 971

Bailer-Jones, C. A. L. 2015, PASP, 127, 994

Bailer-Jones, C. A. L., Rybizki, J., Fouesneau, M., Mantelet, G., & Andrae, R. 2018, AJ, 156, 58

Barack, L., & Cutler, C. 2007, PRD, 75, 042003

Barausse, E., Yunes, N., & Chamberlain, K. 2016, Physical Review Letters, 116, 241104

Bellm, E. 2014, The Third Hot-wiring the Transient Universe Workshop, 27

Bellm, E. C., Kulkarni, S. R., Graham, M. J., et al. 2019, PASP, 131, 018002

Benacquista, M. J., Portegies Zwart, S., & Rasio, F. A. 2001, Classical and Quantum Gravity, 18, 4025

Belczynski, K., Kalogera, V., Rasio, F. A., et al. 2008, ApJS, 174, 223

Benacquista, M., & Holley-Bockelmann, K. 2006, ApJ, 645, 589

Berti, E., Sesana, A., Barausse, E., Cardoso, V., & Belczynski, K. 2016, Physical Review Letters, 117, 101102

Bildsten, L., Shen, K. J., Weinberg, N. N., & Nelemans, G. 2007, ApJL, 662, L95

Binney, J., & Tremaine, S. 2008, Galactic Dynamics: Second Edition, by James Binney and Scott Tremaine. ISBN 978-0-691-13026-2 (HB). Published by Princeton University Press, Princeton, NJ USA, 2008.,

Binney, J., & McMillan, P. 2011, MNRAS, 413, 1889

Bland-Hawthorn, J., & Gerhard, O. 2016, A&A, 54, 529

Bloemen, S., Groot, P., Nelemans, G., & Klein-Wolt, M. 2015, Living Together: Planets, Host Stars and Binaries, 496, 254

Boissier, S., & Prantzos, N. 1999, MNRAS, 307, 857

Bours, M. C. P., Marsh, T. R., Parsons, S. G., et al. 2014, MNRAS, 438, 3399

Breivik, K., Kremer, K., Bueno, M., et al. 2018, ApJL, 854, L1

Brito, R., Ghosh, S., Barausse, E., et al. 2017, Physical Review Letters, 119, 131101

Brown, W. R., Kilic, M., Allende Prieto, C., & Kenyon, S. J. 2010, ApJ, 723, 1072

Brown, W. R., Kilic, M., Hermes, J. J., et al. 2011, ApJL, 737, L23

Brown, W. R., Gianninas, A., Kilic, M., Kenyon, S. J., & Allende Prieto, C. 2016, ApJ, 818, 155

Brown, W. R., Kilic, M., Kenyon, S. J., & Gianninas, A. 2016, ApJ, 824, 46

Brown, W. R., Gianninas, A., Kilic, M., Kenyon, S. J., & Allende Prieto, C. 2016, VizieR Online Data Catalog, 181,

Caprini, C., Hindmarsh, M., Huber, S., et al. 2016, JCAP, 4, 001

Carrasco, J. M., Catalán, S., Jordi, C., et al. 2014, A&A, 565, A11

Carter, P. J., Marsh, T. R., Steeghs, D., et al. 2013, MNRAS, 429, 2143

Coe, D. 2009, arXiv:0906.4123

Cojocaru, R., Torres, S., Althaus, L. G., Isern, J., & García-Berro, E. 2015, A&A, 581, A108

Contigiani, O., Rossi, E. M., & Marchetti, T. 2018, arXiv:1807.04468

Cooray, A., Farmer, A. J., & Seto, N. 2004, ApJL, 601, L47

Copperwheat, C. M., Marsh, T. R., Dhillon, V. S., et al. 2010, MNRAS, 402, 1824

Cornish, N. J., & Larson, S. L. 2003, PRD, 67, 103001

Cornish, N. J., & Rubbo, L. J. 2003, PRD, 67, 022001

Cutler, C. 1998, PRD, 57, 7089

Coyle, P. 2016, arXiv:1607.00379

Dall'Osso, S., & Rossi, E. M. 2014, MNRAS, 443, 1057

Dayal, P., Rossi, E. M., Shiralilou, B., et al. 2018, arXiv:1810.11033

Debes, J. H., Kilic, M., Tremblay, P.-E., et al. 2015, AJ, 149, 176

de Kool, M. 1990, ApJ, 358, 189

De Rosa, R. J., Patience, J., Wilson, P. A., et al. 2014, MNRAS, 437, 1216

Dewey, R. J., & Cordes, J. M. 1987, ApJ, 321, 780

Duchêne, G., & Kraus, A. 2013, ARA&A, 51, 269

Edlund, J. A., Tinto, M., Królak, A., & Nelemans, G. 2005, PRD, 71, 122003

Einstein, A. 1916, Sitzungsberichte der Königlich Preußischen Akademie der Wissenschaften (Berlin), Seite 688-696.,

Einstein, A. 1918, Sitzungsberichte der Königlich Preußischen Akademie der Wissenschaften (Berlin), Seite 154-167

Espaillat, C., Patterson, J., Warner, B., & Woudt, P. 2005, PASP, 117, 189

Estabrook, F. B., & Wahlquist, H. D. 1975, General Relativity and Gravitation, 6, 439

Evans, C. R., Iben, I., Jr., & Smarr, L. 1987, ApJ, 323, 129

Eyer, L., & Mignard, F. 2005, MNRAS, 361, 1136

Eyer, L., Dubath, P., Mowlavi, N., et al. 2012, From Interacting Binaries to Exoplanets: Essential Modeling Tools, 282, 33

Eyer, L., Evans, D. W., Mowlavi, N., et al. 2014, EAS Publications Series, 67, 75

Farmer, A. J., & Phinney, E. S. 2003, MNRAS, 346, 1197

Flynn, C., Holopainen, J., & Holmberg, J. 2003, MNRAS, 339, 817

Fontaine, G., Brassard, P., Green, E. M., et al. 2011, ApJ, 726, 92

Foreman-Mackey, D. 2016, The Journal of Open Source Software, 1,

Fuller, J., & Lai, D. 2012, ApJL, 756, L17

Gaensicke, B., Tremblay, P.-E., Barstow, M., et al. 2015, arXiv:1506.02653

Gaia Collaboration, Prusti, T., de Bruijne, J. H. J., et al. 2016, A&A, 595, A1

Gaia Collaboration, Brown, A. G. A., Vallenari, A., et al. 2018, A&A, 616, A1

García-Berro, E., & Oswalt, T. D. 2016, New Astronomy Reviews, 72, 1

García-Berro, E., Badenes, C., Aznar-Siguán, G., & Lorén-Aguilar, P. 2017, MNRAS, 468, 4815

Geier, S., Marsh, T. R., Wang, B., et al. 2013, A&A, 554, A54

Gianninas, A., Kilic, M., Brown, W. R., Canton, P., & Kenyon, S. J. 2015, ApJ, 812, 167

González-Martín, O., Hernández-García, L., Masegosa, J., et al. 2016, A&A, 587, A1

Green, M. J., Hermes, J. J., Marsh, T. R., et al. 2018, MNRAS, 477, 5646

Green, M. J., Marsh, T. R., Steeghs, D. T. H., et al. 2018, MNRAS, 476, 1663

Guedes, J., Callegari, S., Madau, P., & Mayer, L. 2011, ApJ, 742, 76

Hallakoun, N., Maoz, D., Kilic, M., et al. 2016, MNRAS, 458, 845

Han, Z. 1998, MNRAS, 296, 1019

Heggie, D. C. 1975, MNRAS, 173, 729

Hansen, B. M. S., Brewer, J., Fahlman, G. G., et al. 2002, ApJL, 574, L155

Hermes, J. J., Kilic, M., Brown, W. R., et al. 2012, ApJL, 757, L21

Hermes, J. J., Kilic, M., Brown, W. R., Montgomery, M. H., & Winget, D. E. 2012, ApJ, 749, 42

Hils, D., Bender, P. L., & Webbink, R. F. 1990, ApJ, 360, 75

Holberg, J. B., & Bergeron, P. 2006, AJ, 132, 1221

Hopkins, P. F., Wetzel, A., Kereš, D., et al. 2018, MNRAS, 480, 800

Hulse, R. A., & Taylor, J. H. 1975, ApJL, 195, L51

Hunter, J. D. 2007, Computing in Science and Engineering, 9, 90

Hurley, J. R., Pols, O. R., & Tout, C. A. 2000, MNRAS, 315, 543

Hurley, J. R., Tout, C. A., & Pols, O. R. 2002, MNRAS, 329, 897

Iben, I., Jr., & Tutukov, A. V. 1984, ApJ, 284, 719

Iben, I., Jr., & Tutukov, A. V. 1984, ApJS, 54, 335

Iben, I., Jr., Tutukov, A. V., & Yungelson, L. R. 1997, ApJ, 475, 291

Iben, I., Jr., Tutukov, A. V., & Fedorova, A. V. 1998, ApJ, 503, 344

Igoshev, A., Verbunt, F., & Cator, E. 2016, A&A, 591, A123

Israel, G. L., Hummel, W., Covino, S., et al. 2002, A&A, 386, L13

Israel, G. L., Panzera, M. R., Campana, S., et al. 1999, A&A, 349, L1

Istrate, A. G., Tauris, T. M., Langer, N., & Antoniadis, J. 2014, A&A, 571, L3

Ivanova, N., Justham, S., Chen, X., et al. 2013, A&AR, 21, 59

Jonker, P. G., Bassa, C. G., Nelemans, G., et al. 2011,ApJS, 194, 18

Jordi, K., Grebel, E. K., & Ammon, K. 2006, A&A, 460, 339

Jurić, M., Ivezić, Ž., Brooks, A., et al. 2008, ApJ, 673, 864

Kilic, M., Brown, W. R., Gianninas, A., et al. 2014, MNRAS, 444, L1

Kilic, M., Brown, W. R., Hermes, J. J., et al. 2011, MNRAS, 418, L157

Kilic, M., Munn, J. A., Harris, H. C., et al. 2017, ApJ, 837, 162

Knigge, C. 2006, MNRAS, 373, 484

Klein, A., Barausse, E., Sesana, A., et al. 2016, PhRD, 93, 024003

Kolb, U., Davies, M. B., King, A., & Ritter, H. 2000, MNRAS, 317, 438

Korol, V., Rossi, E. M., Groot, P. J., et al. 2017, MNRAS, 470, 1894

Korol, V., Koop, O., & Rossi, E. M. 2018, ApJL, 866, L20

Korol, V., Rossi, E. M., & Barausse, E. 2018, arXiv:1810.03938

Korol, V., Rossi, E. M., & Barausse, E. 2019, MNRAS, 483, 5518

Kosenko, D. I., & Postnov, K. A. 1998, A&A, 336, 786

Kowalski, P. M., & Saumon, D. 2006, ApJL, 651, L137

Kremer, K., Breivik, K., Larson, S. L., & Kalogera, V. 2017, ApJ, 846, 95

Kremer, K., Chatterjee, S., Breivik, K., et al. 2018, Physical Review Letters, 120, 191103

Kroupa, P., Tout, C. A., & Gilmore, G. 1993, MNRAS, 262, 545

Kupfer, T., Groot, P. J., Bloemen, S., et al. 2015, MNRAS, 453, 483

Kupfer, T., Korol, V., Shah, S., et al. 2018, MNRAS, 480, 302

Lamberts, A., Garrison-Kimmel, S., Hopkins, P. F., et al. 2018, MNRAS, 480, 2704

Landau, L. D., & Lifshitz, E. M. 1971, Course of theoretical physics - Pergamon International Library of Science, Technology, Engineering and Social Studies, Oxford: Pergamon Press, 1971

Lang, R. N., & Hughes, S. A. 2008, ApJ, 677, 1184

Levitan, D., Kupfer, T., Groot, P. J., et al. 2014, ApJ, 785, 114

Liebert, J., Dahn, C. C., & Monet, D. G. 1988, ApJ, 332, 891

Lindegren, L., Hernández, J., Bombrun, A., et al. 2018, A&A, 616, A2

Lipunov, V. M., Nazin, S. N., Panchenko, I. E., Postnov, K. A., & Prokhorov, M. E. 1995, A&A, 298, 677

Lipunov, V. M., & Postnov, K. A. 1987, Sovast, 31, 228

Littenberg, T. B. 2011, PRD, 84, 063009

Littenberg, T. B., Larson, S. L., Nelemans, G., & Cornish, N. J. 2013, MNRAS, 429, 2361

Littenberg, T. B. 2018, arXiv:1805.03589

Liu, J., Zhang, Y., Han, Z., & Zhang, F. 2010, APSS, 329, 297

Livio, M., & Soker, N. 1988, ApJ, 329, 764

Longland, R., Lorén-Aguilar, P., José, J., et al. 2011, ApJL, 737, L34

Lorén-Aguilar, P., Guerrero, J., Isern, J., Lobo, J. A., & García-Berro, E. 2005, MNRAS, 356, 627

LSST Science Collaboration, Abell, P. A., Allison, J., et al. 2009, arXiv:0912.0201

Luri, X., Brown, A. G. A., Sarro, L. M., et al. 2018, A&A, 616, A9

Lyne, A. G., Burgay, M., Kramer, M., et al. 2004, Science, 303, 1153

Macfarlane, S. A., Toma, R., Ramsay, G., et al. 2015, MNRAS, 454, 507

McKernan, B., & Ford, K. E. S. 2016, MNRAS, 463, 2039

Marchetti, T., Rossi, E. M., & Brown, A. G. A. 2018, MNRAS

Marsh, T. R. 1995, MNRAS, 275, L1

Marsh, T. R., Dhillon, V. S., & Duck, S. R. 1995, MNRAS, 275, 828

Marsh, T. R., Nelemans, G., & Steeghs, D. 2004, MNRAS, 350, 113

Marsh, T. R. 2011, Classical and Quantum Gravity, 28, 094019

Maggiore, M. 2008, Gravitational Waves: Theory and Experiments, Oxford Univ. Press

Maoz, D., Hallakoun, N., & Badenes, C. 2018, MNRAS, 476, 2584

Maxted, P. F. L., & Marsh, T. R. 1999, MNRAS, 307, 122

Marsh, T. R. 2011, Classical and Quantum Gravity, 28, 094019

Miller, G. E., & Scalo, J. M. 1979, ApJS, 41, 513

Moore, C. J., Cole, R. H., & Berry, C. P. L. 2015, Classical and Quantum Gravity, 32, 015014

Morris, S. L., & Naftilan, S. A. 1993, ApJ, 419, 344

Motch, C., Haberl, F., Guillout, P., et al. 1996, A&A, 307, 459

Navarro, J. F., Frenk, C. S., & White, S. D. M. 1996, ApJ, 462, 563

Napiwotzki, R., Christlieb, N., Drechsel, H., et al. 2003, The Messenger, 112, 25

Napiwotzki, R. 2009, Journal of Physics Conference Series, 172, 012004

Nelemans, G., Verbunt, F., Yungelson, L. R., & Portegies Zwart, S. F. 2000, A&A, 360, 1011

Nelemans, G., Yungelson, L. R., Portegies Zwart, S. F., & Verbunt, F. 2001, A&A, 365, 491

Nelemans, G., Portegies Zwart, S. F., Verbunt, F., & Yungelson, L. R. 2001, A&A, 368, 939

Nelemans, G., Yungelson, L. R., & Portegies Zwart, S. F. 2001, A&A, 375, 890

Nelemans, G., Steeghs, D., & Groot, P. J. 2001, MNRAS, 326, 621

Nelemans, G., Yungelson, L. R., & Portegies Zwart, S. F. 2004, MNRAS, 349, 181

Nelemans, G., & Tout, C. A. 2005, MNRAS, 356, 753

Nelemans, G., & Jonker, P. G. 2010, NAR, 54, 87

Nelemans, G. 2013, 9th LISA Symposium, 467, 27

Nissanke, S., Vallisneri, M., Nelemans, G., & Prince, T. A. 2012, ApJ, 758, 131

Nissanke, S., Holz, D. E., Dalal, N., et al. 2013, arXiv:1307.2638

Oswalt, T. D., Smith, J. A., Wood, M. A., & Hintzen, P. 1996, Nat, 382, 692

Paczynski, B. 1976, Structure and Evolution of Close Binary Systems, 73, 75

Pajdosz, G. 1995, A&A, 295, L17

Patterson, J., Fried, R. E., Rea, R., et al. 2002, PASP, 114, 65

Patterson, J., Kemp, J., Harvey, D. A., et al. 2005, PASP, 117, 1204

Paxton, B., Bildsten, L., Dotter, A., et al. 2011, ApJS, 192, 3

Peters, P. C., & Mathews, J. 1963, Physical Review, 131, 435

Perets, H. B., Gal-Yam, A., Mazzali, P. A., et al. 2010, Nature, 465, 322

Perlmutter, S., Aldering, G., Goldhaber, G., et al. 1999, ApJ, 517, 565

Piro, A. L. 2011, ApJL, 740, L53

Politano, M. J. 1988, Ph.D. Thesis,

Portegies Zwart, S. F., & Spreeuw, H. N. 1996, A&A, 312, 670

Portegies Zwart, S. F., & Verbunt, F. 1996, A&A, 309, 179

Portegies Zwart, S. F., & Yungelson, L. R. 1998, A&A, 332, 173

Posti, L., & Helmi, A. 2019, A&A, 621, A56

Poveda, A., Allen, C., & Hernández-Alcántara, A. 2007, Binary Stars as Critical Tools & Tests in Contemporary Astrophysics, 240, 417

Prince, T. A., Binetruy, P., Centrella, J., et al. 2007, Bulletin of the American Astronomical Society, 39, 140.01

Provencal, J. L., Winget, D. E., Nather, R. E., et al. 1997, ApJ, 480, 383

Prša, A., Pepper, J., & Stassun, K. G. 2011, AJ, 142, 52

Raghavan, D., McAlister, H. A., Henry, T. J., et al. 2010, ApJS, 190, 1

Ramsay, G., Cropper, M., Wu, K., Mason, K. O., & Hakala, P. 2000, MNRAS, 311, 75

Ramsay, G., Hakala, P., & Cropper, M. 2002, MNRAS, 332, L7

Ramsay, G., Hakala, P., Wu, K., et al. 2005, MNRAS, 357, 49

Rebassa-Mansergas, A., Toonen, S., Korol, V., & Torres, S. 2018, arXiv:1809.07158

Riess, A. G., Filippenko, A. V., Challis, P., et al. 1998, AJ, 116, 1009

Robin, A. C., Reylé, C., Fliri, J., et al. 2014, A&A, 569, A13

Robson, T., & Cornish, N. 2017, Classical and Quantum Gravity, 34, 244002

Robson, T., Cornish, N. J., Tamanini, N., & Toonen, S. 2018, PRD, 98, 064012

Roelofs, G. H. A., Groot, P. J., Marsh, T. R., Steeghs, D., & Nelemans, G. 2006, MNRAS, 365, 1109

Roelofs, G. H. A., Groot, P. J., Nelemans, G., Marsh, T. R., & Steeghs, D. 2007a, MNRAS, 379, 176

Roelofs, G. H. A., Nelemans, G., & Groot, P. J. 2007, MNRAS, 382, 685

Roelofs, G. H. A., Groot, P. J., Benedict, G. F., et al. 2007c, ApJ, 666, 1174

Roelofs, G. H. A., Rau, A., Marsh, T. R., et al. 2010, ApJL, 711, L138

Rossi, E. M., Marchetti, T., Cacciato, M., Kuiack, M., & Sari, R. 2017, MNRAS, 467, 1844

Rowell, N., & Hambly, N. C. 2011, MNRAS, 417, 93

Ruiter, A. J., Belczynski, K., Benacquista, M., & Holley-Bockelmann, K. 2009, ApJ, 693, 383

Ruiter, A. J., Belczynski, K., Benacquista, M., Larson, S. L., & Williams, G. 2010, ApJ, 717, 1006

Saffer, R. A., Liebert, J., & Olszewski, E. W. 1988, ApJ, 334, 947

Sawala, T., Frenk, C. S., Fattahi, A., et al. 2016, MNRAS, 457, 1931

Scalo, J. M. 1986, FCP, 11, 1

Schlegel, D. J., Finkbeiner, D. P., & Davis, M. 1998, ApJ, 500, 525

Shklovskii, I. S. 1970, Sovlast, 13, 562

Schönrich, R. 2012, MNRAS, 427, 274

Schutz, B. F. 1986, Nature, 323, 310

Sesana, A., Vecchio, A., & Colacino, C. N. 2008, MNRAS, 390, 192

Seto, N. 2002, MNRAS, 333, 469

Sick, J., Courteau, S., Cuillandre, J.-C., et al. 2015, Galaxy Masses as Constraints of Formation Models, 311, 82

Shah, S., van der Sluys, M., & Nelemans, G. 2012, A&A, 544, A153

Shah, S., Nelemans, G., & van der Sluys, M. 2013, A&A, 553, A82

Shah, S., & Nelemans, G. 2014, ApJ, 790, 161

Shah, S., & Nelemans, G. 2014, ApJ, 791, 76

Shen, K. J. 2015, ApJL, 805, L6

Skillman, D. R., Patterson, J., Kemp, J., et al. 1999, PASP, 111, 1281

Sofue, Y., Honma, M., & Omodaka, T. 2009, PASJ, 61, 227

Sofue, Y. 2017, PASJ, 69, R1

Solheim, J.-E. 2010, PASP, 122, 1133

Steeghs, D., Marsh, T. R., Barros, S. C. C., et al. 2006, ApJ, 649, 382

Steeghs, D. 2017, Nature Astronomy, 1, 741

Steffen, J. H., Wu, D.-H., & Larson, S. L. 2018, arXiv:1812.03438

Strohmayer, T. E. 2004, ApJL, 608, L53

Strohmayer, T. E. 2005, ApJ, 627, 920

Stroeer, A., & Vecchio, A. 2006, Classical and Quantum Gravity, 23, S809

Tamanini, N., Caprini, C., Barausse, E., et al. 2016, JCAP, 4, 002

Tamanini, N., & Danielski, C. 2018, arXiv:1812.0433

Takahashi, R., & Seto, N. 2002, ApJ, 575, 1030

Timpano, S. E., Rubbo, L. J., & Cornish, N. J. 2006, PRD, 73, 122001

Thorstensen, J. R. 2003, AJ, 126, 3017

Thorstensen, J. R., Lépine, S., & Shara, M. 2008, AJ, 136, 2107

Tokovinin, A., Mason, B. D., & Hartkopf, W. I. 2014, AJ, 147, 123

Toma, R., Ramsay, G., Macfarlane, S., et al. 2016, MNRAS, 463, 1099

Toomre, A., 1963, ApJ, 138, 385

Toonen, S., Nelemans, G., & Portegies Zwart, S. 2012, A&A, 546, A70

Toonen, S., & Nelemans, G. 2013, A&A, 557, A87

Toonen, S., Claeys, J. S. W., Mennekens, N., & Ruiter, A. J. 2014, A&A, 562, A14

Toonen, S., Hollands, M., Gänsicke, B. T., & Boekholt, T. 2017, A&A, 602, A16

Tremblay, P.-E., Bergeron, P., & Gianninas, A. 2011, ApJ, 730, 128

Tremblay, P.-E., Kalirai, J. S., Soderblom, D. R., Cignoni, M., & Cummings, J. 2014, ApJ, 791, 92

Tutukov, A. V., & Yungelson, L. R. 1981, Nauchnye Informatsii, 49, 3

Tutukov, A. V., & Yungelson, L. R. 1988, Soviet Astronomy Letters, 14, 265

Vallisneri, M. 2005, PRD, 72, 042003

van den Broek, D., Nelemans, G., Dan, M., & Rosswog, S. 2012, MNRAS, 425, L24

van der Walt, S., Colbert, S. C., & Varoquaux, G. 2011, Computing in Science and Engineering, 13, 22

van Haaften, L. M., Nelemans, G., Voss, R., et al. 2013, A&A, 552, A69

Vigna-Gómez, A., Neijssel, C. J., Stevenson, S., et al. 2018, MNRAS, 481, 4009

Volonteri, M. 2010, A&A, 18, 279

Webbink, R. F. 1984, ApJ, 277, 355

Wevers, T., Torres, M. A. P., Jonker, P. G., et al. 2016, MNRAS, 462, L106

Willems, B., Kalogera, V., Vecchio, A., et al. 2007, ApJL, 665, L59

Yu, S., & Jeffery, C. S. 2010, A&A, 521, A85

English Summary

For centuries astronomers studied the Universe by collecting light, i.e. electromagnetic wave radiation. Indeed, the human eye is designed to receive part of the electromagnetic spectrum enabling us to see, explore and investigate our world. Nowadays, we are living in times of great technological advancements, which allow us to explore our Universe in a new way - though gravitational wave radiation. Gravitational radiation or gravitational waves are disturbances in the curvature (fabric) of spacetime, generated by accelerated masses (see an artistic rapresentation of gravitational waves in Fig. C.2). Gravitational waves have some similar properties to light. They move at the same speed in a vacuum, and have a certain frequency and amplitude. Where they differ from light is that they are not scattered or absorbed by matter. Albert Einstein predicted the existence of gravitational waves in his general theory of relativity dated 1916. However, their detection became possible only 100 years later, on September 14th 2015, when LIGO (Laser Interferometer Gravitational-Wave Observatory) physically sensed the distortions in spacetime caused by passing gravitational waves generated by two colliding black holes nearly 1.3 billion light years away! Gravitational waves are generated by astronomical objects that either do not emit light (such as black holes in binary systems) or are very faint and are practically undetectable, even with state-of-the-art telescopes (such as neutron star and white dwarf binaries). Therefore, we can use them as a new tool for exploring the "invisible" Universe.

There are many gravitational wave sources also in our own Galaxy, the Milky Way. For example, white dwarf stars in tight binary systems, that spin around each other in less than 1 hour, are prolific gravitational wave emitters. White dwarfs are the end point in evolution for most of the stars in our Galaxy, even our Sun will end its life as a white dwarf. Thus, binary systems composed of two white dwarfs (double white dwarfs) should be ubiquitous in the Milky Way. The Laser Interferometer Space Antenna (see Fig. 1.1), in short LISA, is an ESA mission currently in the development phase, that will detect a large variety of gravitational wave sources, but crucially will also be sensitive to signals from Galactic double white dwarfs. Although quite faint, double white dwarfs can also be seen by optical telescopes, and therefore astronomers call them "multi-messenger" sources. This literally means that we can collect information from them using more than one messenger: electromagnetic waves, messengers of the electromagnetic field, and gravitational waves, messengers of the gravitational field. These two messengers carry very different information. From the light we can find out the chemical composition and the temperature of an astronomical object, while from gravitational waves we can learn about its mass and the distance from us. By combining these two messengers emitted from the same source we can learn much more about it than from either gravitational wave or optical observations alone.

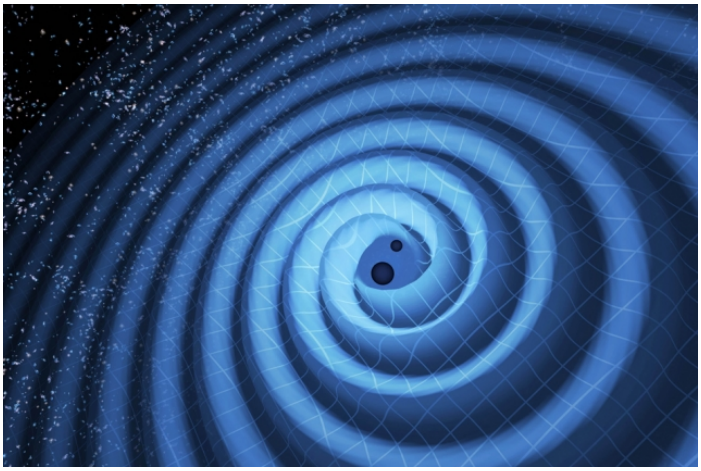

Figure C.2: This illustration shows a binary producing gravitational waves that ripple outward as the binary components spiral toward each other. Image credits: T. Pyle/LIGO

This work

This thesis proposes to use gravitational wave signals from Galactic double white dwarfs to study the Milky Way and its neighbourhood. In particular, it explores how by collecting many electromagnetic and gravitational wave signals from thousands to millions of binary double white dwarfs spread all across our Galaxy, we can perform multi-messenger Galactic Astronomy. This overall goal is addressed in the following independent but complementary questions corresponding to four chapters of the thesis:

- **Chapter 2**: What is the current census of multi-messenger Galactic binaries?
- **Chapter 3**: How many multi-messenger double white dwarfs we will have in the LISA era?
- **Chapter 4**: How far beyond our Galaxy can LISA detect double white dwarfs; and what are their properties?
- **Chapter 5**: What can we learn about Milky Way by combining electromagnetic and gravitational wave observations?

To answer to the first question, a sample of double white dwarfs previously discovered with optical telescopes is considered. Because one can measure a number of the key proprieties of binaries from optical observations, it is possible to predict the gravitational wave signals ahead of the start of the LISA mission, and use these binaries as a reference (verification) when analysing LISA data. This is why the sample of known sources are also called "LISA verification binaries". Of course, a requirement is the knowledge of a verification source's properties, such as the orbital period, binary components masses and the distance, to a great precision. In particular, distances to verification binaries became recently available with the *Gaia* mission. *Gaia* is an ESA space mission designed to map the whole sky and register positions, brightness, distances and motions for billions of stars in our Galaxy. In **Chapter 2** the distances

to verification binaries are derived from *Gaia* observations. This helped to establish that out of about 50 candidate verification binaries observed by *Gaia*, 13 will be also detectable by LISA. By using a sophisticated LISA data simulator it was also possible to predict how well LISA can characterise them.

To perform a global multi-messenger study of the Galaxy, a large number of multi-messenger sources are required. Therefore, in **Chapter 3** quantitative estimates of the number, and the properties, of the future observations of detached double white dwarfs detectable by the currently ongoing and future large astronomical surveys were performed. Such estimates can be realised by combining a number of numerical techniques. The first is to predict the intrinsic properties of double white dwarfs with a technique called 'binary population synthesis'. It represents a collection of numerical recipes for all physical processes involved in binary evolution. These prescriptions are combined in a code that evolves binary stars from the birth of component stars, to white dwarf formation and beyond. Secondly, a detailed galactic model is used to representatively distribute the population of binaries in a synthetic Galaxy. Lastly, knowing the position and properties of these binaries, one can compute their synthetic optical and gravitational wave signals. In particular, for optical observations *Gaia* and LSST (two future big Galactic stellar surveys) and for gravitational wave observations LISA are considered. This thesis shows that *Gaia*, LSST and LISA will soon discover respectively hundreds, thousands and tens of thousands double white dwarfs, out of which at least a hundred binaries will be multi-messenger. Thus, it will be possible to perform muti-messenger Astronomy with them.

Having shown that many new double white dwarfs will be detected with LISA through GW radiation in our Galaxy, **Chapter 4** explores whether LISA can also detect them in nearby galaxies, those forming the so-called Local Group. **Chapter 4** illustrates what properties (specifically mass and gravitational wave frequency) a binary should have to be detected at a certain distance from the Milky Way. Because the strength of the gravitational wave signal increases with increasing mass and frequency and decreases with increasing distance, high frequency massive double white dwarfs can be seen almost up to the edge of the Local Group. Binaries with such properties are difficult targets for optical telescopes because more massive white dwarfs are fainter and smaller. Such high mass and frequency double white dwarfs are very important: they are thought to generate luminous supernova explosions, used in Astronomy as distance indicators in the nearby Universe. However, it is still unclear what generates these explosions. For, example, the merger of two white dwarfs is one possible way of producing these supernovae. Thus, future observations of double white dwarfs in our Galaxy and in the nearby galaxies through GWs can confirm or rule out this possibility.

Finally, **Chapter 5** proposes joint EM and GW observations of DWDs for studying our Galaxy. It is possible to virtually divide the structure of our Galaxy in different components. The main components are: the bulge - the central dense region, the stellar disc - an extended flat component, and the halo - a large diffuse component that encompass the previous two. **Chapter 5** shows that using GW detections provided by LISA one can map the disc and the bulge, providing a tomography of the Galaxy. There are a number of advantages in using GWs instead of EM radiation for this study. Firstly, GWs are not obscured by interstellar dust that heavily affects optical observation in the inner and central regions of the Galaxy. Secondly, the strength of GW signals decrease much more slowly with increasing distance allowing the detection

of optically faint sources such as DWD very far away. The ability to study the overall properties of the Galaxy with DWDs will also be significantly enhanced by using GWs in combination with EM observations. The success of this synergy is due to LISA's ability to localise binaries through virtually the whole Galaxy, thus mapping its shape, while optical observations yield the motion of stars, tracing the underlying total mass of matter in our Galaxy.

Main conclusions

This thesis illustrates the potential of future gravitational wave observation with LISA for Galactic Astronomy. It shows that LISA can discover tens of thousands of new double white dwarf binaries all across the Galaxy, providing a new way of mapping Milky Way's structure. More importantly, one can combine optical and gravitational wave observations of these binaries as they emit both detectable gravitational waves and light. This will allow one to perform multi-messenger Galactic studies. This thesis shows an example of a multi-messenger study leading to precise quantitative estimates of the mass of the main stellar components of the Galaxy (the bulge and disc). In addition, gravitational waves signals can reach us from nearby galaxies: for example, the Magellanic Clouds and the Andromeda galaxy. To be detected by LISA, these extra-galactic double white dwarfs need to be more massive and orbit around each other faster than sourecs in our Galaxy. Such double white dwarfs are believed to be the progenitors of luminous supernova explosions. This thesis highlights that LISA may be our best tool for understanding the nature of these supernova events.

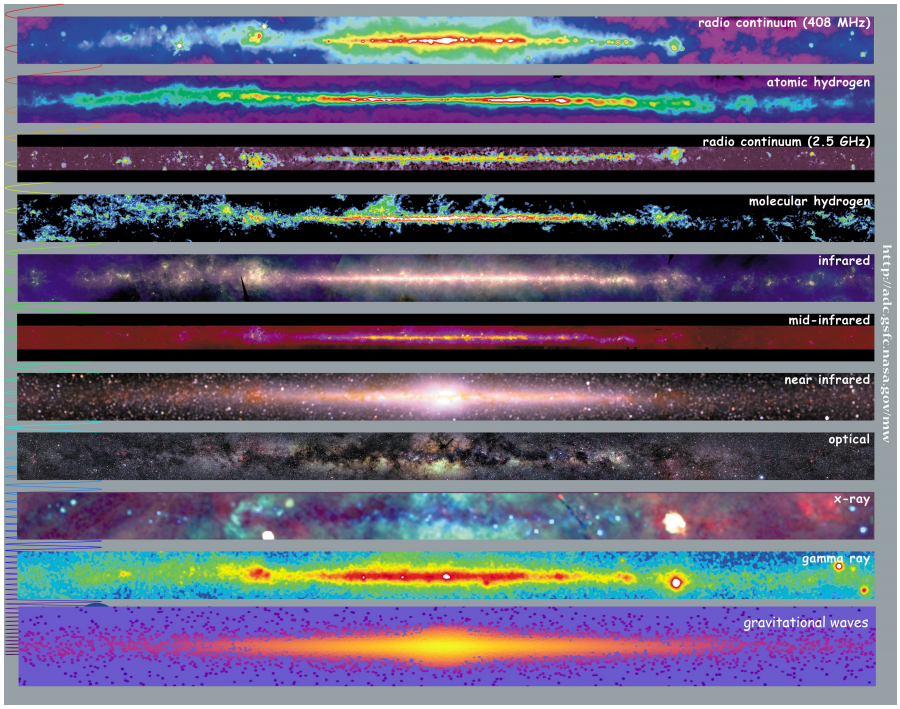

Figure C.3: Milky Way at different frequencies from radio to gamma rays (image credits: NASA) The bottom panel show the Milky Way as seen by LISA through gravitational wave radiation from Galactic double white dwarf binaries (this thesis).

Nederlandse Samenvatting

Eeuwenlang hebben sterrenkundigen het heelal bestudeerd door licht, oftewel elektromagnetische straling, op te vangen. Het menselijk oog is ontworpen om een deel van het elektromagnetische spectrum op te vangen, waardoor we onze wereld kunnen zien, verkennen en onderzoeken. Tegenwoordig leven we in tijden van grote technologische vooruitgang, waardoor we ons heelal op een nieuwe manier kunnen verkennen, namelijk door middel van zwaartekrachtgolfstraling. Zwaartekrachtstraling, of zwaartekrachtgolven, zijn verstoringen in de kromming (de structuur) van de ruimtetijd, gegenereerd door versnelde massa's (zie een artistieke weergave van zwaartekrachtgolven in Fig. C.4). Zwaartekrachtgolven en licht hebben een aantal eigenschappen gemeen. Ze bewegen met dezelfde snelheid in een vacuüm en hebben een bepaalde frequentie en amplitude. Maar in tegenstelling tot licht, worden zwaartekrachtgolven niet verstrooid of geabsorbeerd door materie. Albert Einstein voorspelde het bestaan van zwaartekrachtgolven in zijn algemene relativiteitstheorie uit 1916. Hun detectie werd echter pas 100 jaar later mogelijk, op 14 september 2015. De LIGO (Laser Interferometer Gravitational-Wave Observatory)-detector nam toen de vervormingen in de ruimtetijd waar die werden veroorzaakt door passerende zwaartekrachtgolven, gegenereerd door twee botsende zwarte gaten op een afstand van bijna 1,3 miljard lichtjaren! Zwaartekrachtgolven worden veroorzaakt door astronomische objecten die ofwel geen licht uitstralen (zoals zwarte gaten in dubbelsystemen) of die erg zwak zijn en praktisch niet waarneembaar zijn, zelfs niet met geavanceerde telescopen (zoals neutronensterren en dubbele witte dwergen). Daarom kunnen we ze gebruiken als een nieuw hulpmiddel om het "onzichtbare" heelal te verkennen.

Ook in ons eigen sterrenstelsel, de Melkweg, zijn veel zwaartekrachtgolfbronnen. Witte dwergsterren in nauwe dubbelsystemen die in minder dan een uur om elkaar heen draaien, zijn bijvoorbeeld sterke bronnen van zwaartekrachtgolven. Witte dwergen vormen het eindpunt van de evolutie voor de meeste sterren in onze Melkweg. Zelfs onze zon zal haar leven beëindigen als een witte dwerg. Daarom zouden dubbelsterren die uit twee witte dwergen bestaan (dubbele witte dwergen), alomtegenwoordig moeten zijn in de Melkweg. De Laser Interferometer Space Antenna (Fig. 1.1), kortweg LISA, is een ESA-missie die zich momenteel in de ontwikkelingsfase bevindt en een grote verscheidenheid aan zwaartekrachtgolfbronnen zal detecteren. Maar een cruciaal aspect van LISA is dat het gevoelig genoeg is om signalen van dubbele witte dwergen op te vangen. Hoewel vrij zwak, kunnen dubbele witte dwergen ook worden gezien door optische telescopen. Daarom noemen sterrenkundigen ze *multi-messenger*-bronnen. Dit betekent letterlijk dat we informatie van hen kunnen verzamelen met behulp van meer dan één boodschapper: elektromagnetische golven, de boodschappers van het elektromagnetische veld en zwaartekrachtgolven, de boodschappers van

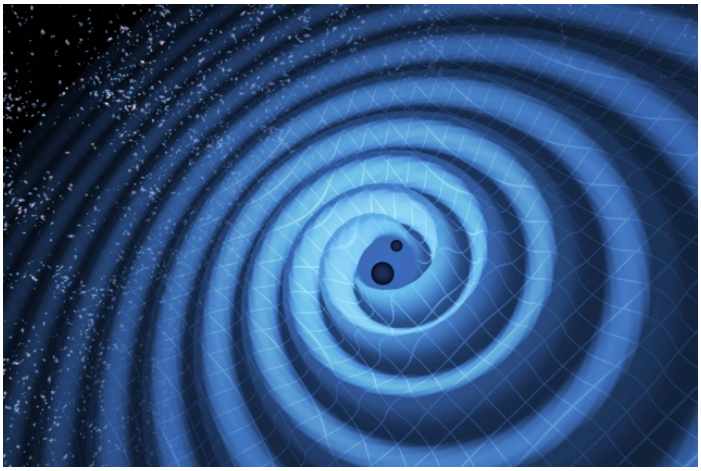

Figuur C.4: Deze illustratie toont een dubbelster die zwaartekrachtgolven genereert die naar buiten rimpelen terwijl de componenten van dubbelster spiraalsgewijs naar elkaar toe bewegen. Bron: T. Pyle / LIGO

het zwaartekrachtveld. Deze twee boodschappers bevatten zeer verschillende informatie. Vanuit het licht kunnen we de chemische samenstelling en de temperatuur van een astronomisch object achterhalen, terwijl we van zwaartekrachtgolven kunnen leren over zijn massa en de afstand tot ons. Door deze twee boodschappers die van dezelfde bron afkomstig zijn te combineren, kunnen we veel meer over die bron leren dan door zwaartekrachtgolven of door optische waarnemingen alleen.

Dit proefschrift

Dit proefschrift stelt voor om zwaartekrachtgolven van galactische dubbele witte dwergen (in ons eigen sterrenstelsel) te gebruiken om de Melkweg en zijn omgeving te bestuderen. Het onderzoekt in het bijzonder hoe we galactische *multi-messenger*-sterrenkunde kunnen doen door het verzamelen van veel elektromagnetische en zwaartekrachtgolfsignalen van duizenden tot miljoenen dubbele witte dwergen verspreid in onze Melkweg. Dit algemene doel wordt behandeld in de volgende onafhankelijke maar aanvullende vragen die overeenkomen met vier hoofdstukken van het proefschrift:

- **Hoofdstuk 2**: Wat is de huidige telling van multi-messenger galactische dubbelsterren?
- **Hoofdstuk 3**: Hoeveel multi-messenger dubbele witte dwergen zullen we in het LISA-tijdperk hebben?
- **Hoofdstuk 4**: Hoe ver buiten ons sterrenstelsel kan LISA dubbele witte dwergen detecteren; en wat zijn hun eigenschappen?
- **Hoofdstuk 5**: Wat kunnen we over de Melkweg leren door elektromagnetische en zwaartekrachtgolfobservaties te combineren?

Om de eerste vraag te beantwoorden, wordt een verzameling van dubbele witte dwergen bestudeerd die eerder met optische telescopen zijn ontdekt. Omdat men

een aantal van de belangrijkste eigenschappen van dubbelsterren uit optische waarnemingen kan meten, is het mogelijk om de zwaartekrachtgolfsignalen voorafgaand aan de LISA-missie te voorspellen en deze dubbelsterren te gebruiken als een referentie (verificatie) bij het analyseren van LISA-gegevens. Dit is de reden waarom verzameling van bekende bronnen ook de *LISA verfication binaries*, oftewel LISA-verificatie-dubbelsterren wordt genoemd. Uiteraard is het hiervoor noodzakelijk om kennis te hebben van de eigenschappen van een verificatiebron, zoals de baanperiode, de dubbelstercomponentenmassa's en de afstand, tot grote precisie. Met name de afstanden tot verificatie-dubbelsterren zijn onlangs beschikbaar gekomen met de *Gaia*-missie. *Gaia* is een ESA-ruimtemissie die is ontworpen om de volledige hemel in kaart te brengen en de posities, helderheid, afstanden en bewegingen te registreren voor miljarden sterren in onze Melkweg. In **Hoofdstuk 2** zijn de afstanden tot verificatie-dubbelsterren afgeleid van *Gaia*-waarnemingen. Dit hielp om vast te stellen dat van de ongeveer 50 kandidaat-verificatie-dubbelsterren die door *Gaia* zijn waargenomen, 13 ook door LISA kunnen worden gedetecteerd. Door een geavanceerde LISA-datasimulator te gebruiken, was het ook mogelijk om te voorspellen hoe goed LISA ze kan karakteriseren.

Om een *multi-messenger*-studie te doen van de Melkweg, is een groot aantal multi-messenger-bronnen vereist. Daarom werden in **Hoofdstuk 3** kwantitatieve schattingen gemaakt van het aantal en de eigenschappen van de toekomstige waarnemingen van vrijstaande dubbele witte dwergen die door de huidige lopende en toekomstige grote astronomische waarneemprogramma's kunnen worden gedetecteerd. Dergelijke schattingen kunnen worden gerealiseerd door een aantal numerieke technieken te combineren. De eerste voorspelt de intrinsieke eigenschappen van dubbele witte dwergen met een techniek die "dubbelsterpopulatiesynthese" wordt genoemd. Deze techniek vertegenwoordigt een verzameling numerieke recepten voor alle fysische processen die betrokken zijn bij dubbelsterevolutie. Deze voorschriften worden gecombineerd in een code die dubbelsterren evolueert vanaf de geboorte van componentsterren tot de vorming van een witte dwerg en verder. De tweede techniek gebruikt een gedetailleerd galactisch model om de populatie van dubbelsterren in een synthetisch sterrenstelsel representatief te verdelen. Als de positie en eigenschappen van deze dubbelsterren bekend is, kan men als laatste hun synthetische optische en zwaartekrachtgolfsignalen berekenen. In het bijzonder worden voor optische waarnemingen *Gaia* en LSST (twee toekomstige grote waarneemprogramma's aan de sterren in onze Melkweg) en voor zwaartekrachtsgolf waarnemingen LISA beschouwd. Dit proefschrift laat zien dat *Gaia*, LSST en LISA binnenkort respectievelijk honderden, duizenden en tienduizenden dubbele witte dwergen zullen ontdekken, waarvan minstens honderd *multi-messenger*-dubbelsterren zullen zijn. Het is dus mogelijk om *muti-messenger*-sterrenkunde met ze uit te voeren.

Nadat we hebben aangetoond dat veel nieuwe dubbele witte dwergen zullen worden gedetecteerd met LISA door middel van zwaartekrachtgolfstraling in ons sterrenstelsel, onderzoekt **Hoofdstuk 4** of LISA ze ook kan detecteren in sterrenstelsels in de buurt, die de zogenaamde "Lokale Groep" vormen. Het illustreert welke eigenschappen (specifiek massa en zwaartekrachtgolffrequentie) een dubbelster op een bepaalde afstand van de Melkweg moet hebben, om te kunnen worden gedetecteerd. Omdat de sterkte van het zwaartekrachtgolfsignaal toeneemt met toenemende massa en frequentie en afneemt met toenemende afstand, zijn hoogfrequente massieve dubbele witte dwergen bijna tot aan de rand van de Lokale Groep te zien. Dubbelsterren met dergelijke

eigenschappen zijn moeilijke doelen voor optische telescopen, omdat massieve witte dwergen zwakker en kleiner zijn. Zulke dubbele witte dwergen met een hoge massa en frequentie zijn erg belangrijk: ze zijn kandidatend om heldere supernova-explosies te genereren, die in de sterrenkunde worden gebruikt als afstandsindicatoren in het nabije heelal. Het is echter nog steeds onduidelijk wat deze explosies genereert. De samenvoeging van twee witte dwergen is e'e'n manier om deze supernovae te produceren. Toekomstige waarnemingen van dubbele witte dwergen in onze Melkweg en in de nabije sterrenstelsels via zwaartekrachtgolven zullen deze mogelijkheid bevestigen of uitsluiten.

Tot slot stelt **Hoofdstuk 5** voor om elektromagnetische en zwaartekrachtgolfwaarnemingen van dubbele witte dwergen samen te voegen om onze Melkweg te bestuderen. Het is mogelijk om de structuur van onze Melkweg te verdelen in verschillende componenten. De belangrijkste componenten zijn: de *bulge* (centrale verdikking) - het centrale dichte gebied, de galactische schijf - een verlengde platte component, en de halo - een groot een grote diffuse component die de vorige twee omvat. **Hoofdstuk 5** laat zien dat met zwaartekrachtgolfdetecties van LISA de schijf en de verdikking in kaart kunnen worden gebracht, waardoor een tomogram van de Melkweg ontstaat. Het gebruik van zwaartekrachtgolven in plaats van elektromagnetische straling heeft een aantal voordelen voor deze studie. Ten eerste worden zwaartekrachtgolven niet verdoezeld door interstellair stof dat de optische waarneming in de binnenste en centrale gebieden van de Melkweg sterk beïnvloedt. Ten tweede neemt de sterkte van zwaartekrachtgolfsignalen veel langzamer af met toenemende afstand, waardoor de detectie van optisch zwakke bronnen zoals dubbele witte dwergen op grote afstand mogelijk is. Het vermogen om de algehele eigenschappen van de Melkweg door middel van dubbele witte dwergen te bestuderen, zal ook aanzienlijk worden verbeterd door zwaartekrachtgolven te gebruiken in combinatie met elektromagnetische waarnemingen. Het succes van deze synergie is te danken aan het vermogen van LISA om dubbelsterren te lokaliseren in vrijwel de hele Melkweg en daarmee de vorm ervan in kaart te brengen, terwijl optische waarnemingen de beweging van sterren blootleggen, waardoor de totale materiemassa in onze Melkweg wordt blootgelegd.

Conclusies

Dit proefschrift illustreert het potentieel van toekomstige zwaartekrachtgolfobservaties met LISA voor sterrenkundige studies van onze Melkweg. Het laat zien dat LISA tienduizenden nieuwe dubbele witte dwergen in de hele Melkweg kan ontdekken, wat een nieuwe manier is om de structuur van de Melkweg in kaart te brengen. Nog belangrijker is dat men optische en zwaartekrachtgolfwaarnemingen van deze dubbelsterren kan combineren, omdat ze zowel waarneembare zwaartekrachtgolven als licht uitstralen. Hierdoor is het mogelijk om *multi-messenger* galactisch onderzoek uit te voeren. Dit proefschrift laat een voorbeeld zien van een *multi-messenger*-onderzoek dat leidt tot precieze kwantitatieve schattingen van de massa van de belangrijkste stellaire componenten van de Melkweg (de verdikking en de schijf). Daarnaast kunnen zwaartekrachtgolfsignalen ons bereiken vanuit nabije sterrenstelsels: bijvoorbeeld de Magelhaense wolken en het Andromedastelsel. Om door LISA te worden gedetecteerd, moeten deze extragalactische dubbele witte dwergen (buiten de Melkweg) massiever zijn en sneller om elkaar heen draaien dan bronnen die tot nu toe bekend zijn in onze Melkweg. Zulke dubbele witte dwergen worden verondersteld de voorlopers te zijn van heldere supernova-explosies. Dit proefschrift benadrukt dat LISA misschien wel ons

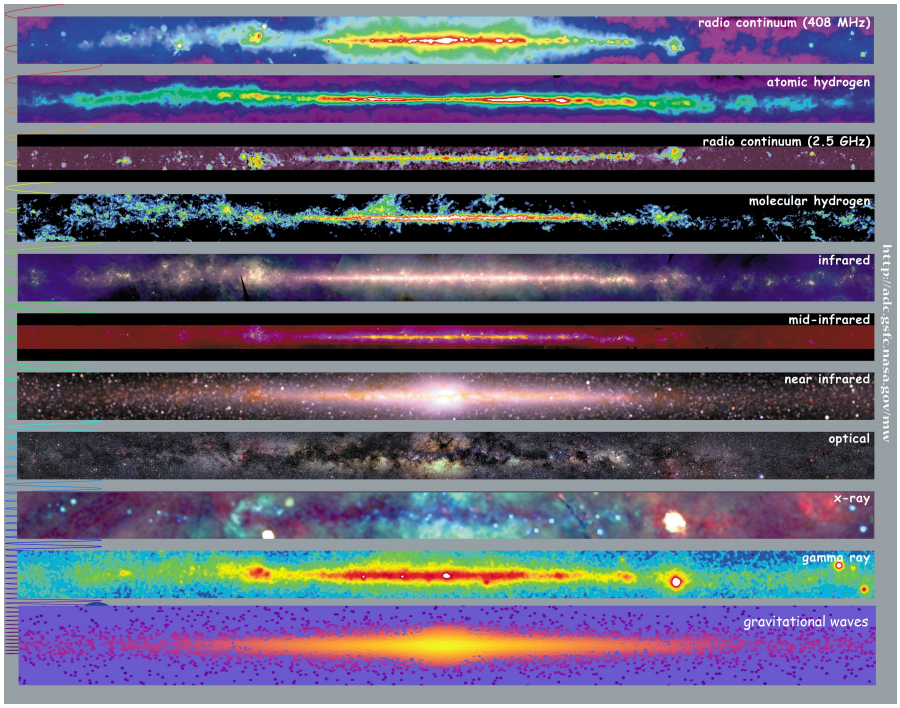

Figuur C.5: De Melkweg op verschillende frequenties van radio tot gammastraling (bron: NASA). Het onderste paneel toont de Melkweg in zwaartekrachtgolfstraling van galactische dubbele witte dwergen, zoals gezien door LISA (dit proefschrift).

beste instrument is om de aard van deze supernovae te begrijpen.

Українське резюме

Протягом століть астрономи вивчали Всесвіт за допомогою світла, а саме електромагнітного хвильового випромінення. І справді, людське око здатне сприймати частину спектру електромагнітного випромінювання, що дає нам змогу вивчати та досліджувати наш світ. У наш час нам доступні неймовірні технологічні досягнення, що роблять можливим дослідження всесвіту через призму випромінення гравітаційних хвиль. Гравітаційне випромінювання або ж гравітаційні хвилі є збуренням у викривленні простору-часу, створене прискореними масами (див. художнє представлення гравітаційних хвиль на рис. B.6). Гравітаційні хвилі має декі спільні риси з світлом. У вакуумі їхня швидкість однакова, а також мають певну частоту та амплітуду коливання. А відрізняє їх від світла те, що вони не розсіюються чи поглинаються матерією. Альберт Ейнштейн передбачив існування гравітаційних хвиль у своїй загальній теорії відносності у 1916 році. Однак, їх реєстрація стала можливою лише тільки через століття, 14 вересня 2015 року, коли ЛІГО (Лазерна інтерферометрична гравітаційно-хвильова обсерваторія) (англ. Laser Interferometer Gravitational-Wave Observatory, LIGO) фізично зареєстрував збурення простору-часу спричиненні гравітаційними хвилями згенерованими злиттям двох чорних дір на відстані 1.3 млрд. світлових років від нас. Гравітаційні хвилі утворюються астрономічним тілами, що не випромінюють світло, як от чорні діри у бінарних системах, або ж ледь випромінюють, що навіть найдосконаліші телескопи не в змозі його зареєструвати, як от бінарні системи білих карликів або ж нейтронних зірок. Таким чином, ми можемо використовувати їх як новий інструмент дослідження "невидимого" всесвіту.

У нашій Галактиці, Чумацький Шлях, існує велика кількість джерел гравітаційних хвиль. Наприклад, білі карлики у тісних бінарних системах, що обертаються навколо один одного менш ніж за 1 годину, є багатим джерелом гравітаційних хвиль. Білі карлики є кінцевою віхою еволюції більшості зірок у нашій Галактиці, ба навіть наше Сонце у кінці свого існування перетвориться на білого карлика. Таким чином бінарні системи білих карликів повинні бути широко розповсюдженні у Чумацькому Шляху. Космічна антена лазерного інтерферометра (LISA, рис. 1.1) це місія Європейського космічного агентства, ЄКА (European Space Agency, ESA), що знаходиться у розробці та матиме змогу реєструвати різноманітну кількість джерел гравітаційних хвиль ба а більше буде чутливим до сигналів від бінарних систем білих карликів. Також вони можуть бути ледь помітні для оптичних телескопів, а отже науковці можуть вважати їх "багатоканальними" джерелами. А це означає, що ми можемо отримувати від них інформацію у різних площинах: електромагнітні хвилі від електромагнітного поля, а гравітаційні хвилі від гравітаційного поля. Вони несуть у собі дуже різну інформацію. Світло нам дає змогу

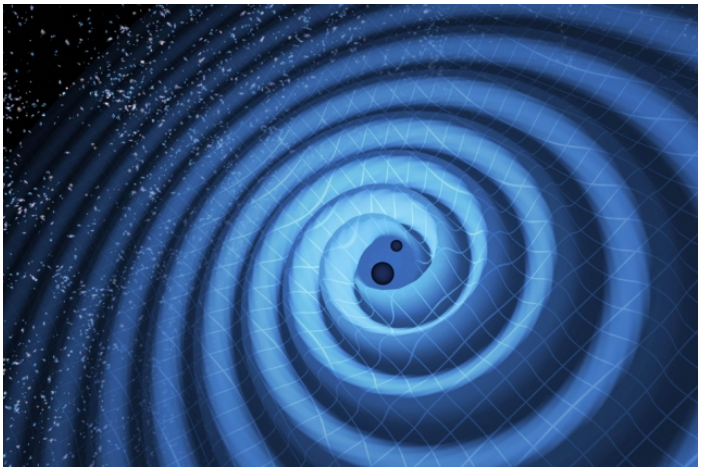

Рис. В.6: Ілюстрація демонструє створення гравітаційних хвиль бінарною системою, що розходяться від центру у той час як компоненти системи рухаються один до одного по спіралі. Image credits: T. Pyle/LIGO

дізнатися більше про хімічний склад та температуру астрономічного об'єкту, у той самий час гравітаційні хвилі повідомляють нам про його масу та відстань від нас. Поєднуючи цю інформацію з одного джерела ми можемо дізнатися про нього більше, ніж від гравітаційних хвиль чи оптичних спостережень окремо.

Дисертація

Ця дисертація пропонує використання сигналів гравітаційних хвиль від бінарних білих карликів для вивчення нашої Галактики та її околиць. Зокрема, вона вивчає те як збір сигналів гравітаційних та електромагнітних хвиль з тисяч та мільйонів бінарних систем білих карликів розкиданих по всій нашій Галактиці уможливлює багатоджерельну Галактичну Астрономію. Ця мета висвітлюється у наступних незалежних, але доповнюючих один одного питаннях висвітлених у чотирьох розділах цієї дисертації:

- **Розділ 2**: Яка кількість багатоджерельних бінарних систем у Галактиці нам выдома?
- **Розділ 3**: Скільки багатоджерельних подвійних білих карликів буде нам доступно протягом місії LISA?
- **Розділ 4**: Як далеко за межами нашої Галактики LISA зможе реєструвати подвійних білих карликів; та які в них властивості?
- **Розділ 5**: Що ми можемо дізнатися про на Чумацький Шлях поєднавши наші дослідження електромагнітних та гравітаційних хвиль?

Для відповіді на перше запитання розглядається зразок подвійних білих карликів, раніше виявлених з оптичними телескопами. Оскільки можна виміряти ряд ключових властивостей бінарних елементів за допомоги оптичних спостережень, стає можливим прогнозувати сигнали гравітаційних хвиль перед початком місії

LISA, і використовувати ці бінарні системи як приклад (верифікація) при аналізі даних LISA. Ось чому вибірка відомих джерел також називається "верифікаційні бінарні системи LISA". Звичайно, для більшої точності важливим є наявність даних щодо властивостей джерела верифікації, таких як орбітальний період, маси компонентів бінарних систем та відстань між ними. Зокрема, відстань до верифікаційних бінарних систем стала доступною завдяки місії *Gaia*. *Gaia* це космічна місія ESA, призначена створення мапи усього небосхилу і реєстрації позицій, яскравості, відстаней і рухів для мільярдів зірок нашої Галактики. У **Розділі 2** відстані до верифікаційних бінарних систем отриманні завдяки спостереженням місії *Gaia*. Вони допомогли встановити, що приблизно з 50 існуючих верифікаційних бінарних систем, виявлених *Gaia*, 13 також можна буде виявити LISA. За допомогою складного симулятора даних LISA також можна було передбачити, наскільки добре LISA може їх охарактеризувати.

Щоб виконати глобальне багатогалузеве дослідження Галактики, потрібна велика кількість джерел мульти-месенджерів. Тому в **Розділі 3** були проведені кількісні оцінки чисельності та властивостей майбутніх спостережень окремих бінарних систем білих карликів, які можна було виявити в поточних і майбутніх великих астрономічних дослідженнях. Такі оцінки можуть бути реалізовані шляхом об'єднання ряду чисельних методів. Перший полягає в прогнозуванні властивостей бінарних систем білих карликів методом, який називається "бінарний популяційний синтез". Він являє собою набір чисельних рецептів для всіх фізичних процесів, що беруть участь у бінарній еволюції. Ці приписи поєднуються в коді, який еволюціонує у бінарних зірках від народження компонентних зірок, до формування білих карликів та потім. Другий метод використовує детальну Галактичну модель для репрезентативного розподілу популяції бінарних систем у синтетичній Галактиці. Нарешті, знаючи положення і властивості цих бінарних елементів, можна обчислити їх синтетичні оптичні сигнали і сигнали гравітаційних хвиль. Зокрема, для оптичних спостережень *Gaia* і LSST (два майбутніх масштабних Галактичних зоряних обстеження) і для спостережень гравітаційних хвиль LISA. Ця дисертація показує, що *Gaia*, LSST і LISA незабаром знайдуть, відповідно, сотні, тисячі і десятки тисяч білих карликів, з яких, принаймні, сто бінарних систем будуть мульти-месенджерами. Таким чином, з ними можна буде виконувати багатоджерельну астрономію.

Показавши, що багато нових подвійних білих карликів будуть виявлятися LISA за допомогою випромінювання гравітаційних хвиль в нашій Галактиці, **Розділ 4** досліджує, чи може LISA також виявляти їх у сусідніх галактиках, що утворюють так звану місцеву галактичну групу. Вона ілюструє, які властивості (зокрема, частота маси і гравітаційної хвилі) бінарної системи повинні бути виявлені на певній відстані від Чумацького Шляху. Оскільки сила гравітаційного хвильового сигналу зростає зі збільшенням маси і частоти і зменшується зі збільшенням відстані, високочастотні масивні подвійні білі карлики можна побачити майже на краю Місцевої групи. Бінарні системи з такими властивостями є складними мішенями для оптичних телескопів, тому що більш масивні білі карлики є менш помітними і меншими за розміром. Такі високочастотні подвійні білі карлики є дуже важливими: вони, як вважають, генерують світлові вибухи наднових, що використовуються в астрономії як індикатори відстані в сусідньому Всесвіті. Проте досі незрозуміло, що породжує ці вибухи. Наприклад, злиття двох білих карликів є одним з можливих способів отримання цих наднових. Таким чином,

майбутні спостереження подвійних білих карликів в нашій Галактиці і в сусідніх галактиках через гравітаційні хвилі можуть підтвердити або виключити цю можливість.

І на сам кінець, у **Розділі 5** пропонується приєднатися до спостережень електромагнітних та гравітаційних хвиль подвійних білих карликів для дослідження нашої Галактики. Можна практично розділити структуру нашої Галактики на різні компоненти. Основними складовими є: випуклість (або балдж) – центральна щільна область, зоряний диск – розширена плоска складова та сфероїдне гало – великий дифузний компонент, що охоплює попередні два. У **Розділі 5** видно, що використовування реєстрації гравітаційних хвиль, які надає LISA, дозволяє зіставити диск та балдж, забезпечуючи томографію Галактики. Існує ряд переваг використання гравітаційні хвиль замість електромагнітного випромінювання для даного дослідження. По-перше, гравітаційні хвилі не затьмарюються міжзоряним пилом, що сильно впливає на оптичне спостереження у внутрішніх і центральних областях Галактики. По-друге, міцність сигналів гравітаційних хвиль зменшується набагато повільніше зі збільшенням відстані, що дозволяє виявити оптично слабкі джерела, такі як подвійні білі карлики, на великій відстані. Можливість вивчення загальних властивостей Галактики за допомоги подвійних білих карликів також буде значно підвищена за рахунок використання гравітаційних хвиль у поєднанні з спостереженнями електромагнітного хвиль. Успіх цієї синергії зумовлений здатністю LISA локалізувати бінарні системи через практично всю Галактику, таким чином відображаючи її форму, тоді як оптичні спостереження дають інформацію про рух зірок, простежуючи загальну масу матерії в нашій Галактиці.

Висновок

Ця дисертація ілюструє потенціал майбутнього спостереження гравітаційних хвиль з LISA для Галактичної астрономії. Це показує, що LISA може виявити десятки тисяч нових бінарних систем білих карликів по всій Галактиці, забезпечуючи новий спосіб відображення структури Чумацького Шляху. Що більш важливо, можна поєднати оптичні спостереження та дані від спостережень за гравітаційними хвилями бінарних систем, оскільки вони випромінюють як гравітаційні хвилі, так і світло. Це дозволить виконувати багатогалузеві Галактичні дослідження. У дисертації наведено приклад багатоджерельне дослідження, що веде до точних кількісних оцінок маси основних зоряних компонентів Галактики (балдж і диск). Крім того, сигнали гравітаційних хвиль можуть дійти до нас з сусідніх галактик: наприклад, Магелланові хмари та Андромеди. Щоб бути виявленими LISA, ці позаГалактичні подвійні білі карлики повинні бути більш масивними і обертатися навколо один одного швидше, ніж джерела в нашій Галактиці. Такі подвійні білі карлики вважаються прабатьками світлових вибухів наднових. Ця дисертація підкреслює, що LISA може бути нашим найкращим інструментом для розуміння природи цих подій наднових.

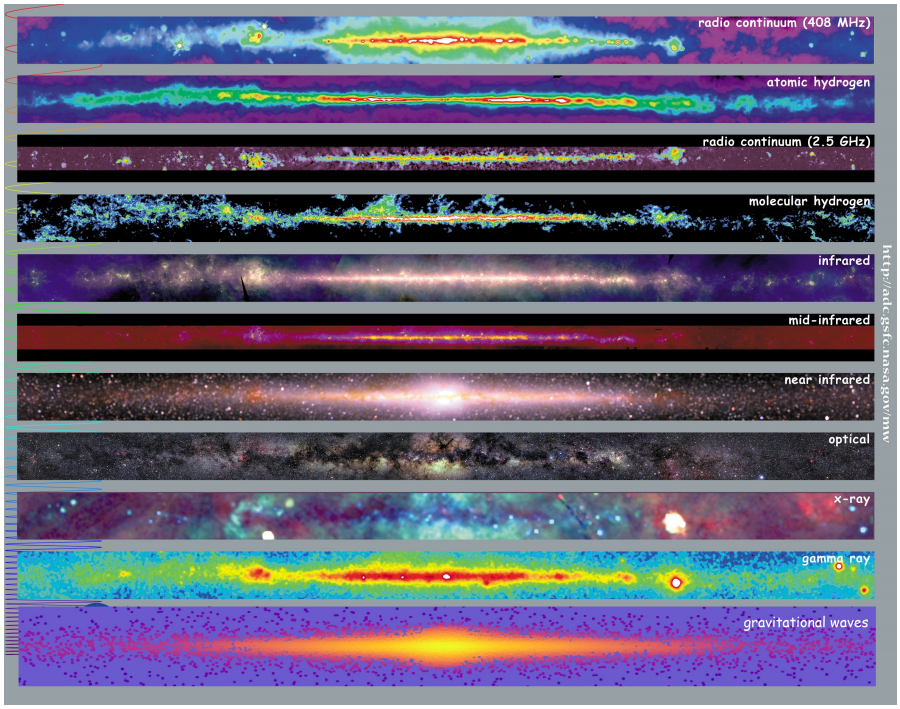

Рис. B.7: Чумацький Шлях у різних частотах від радіо до гама випромінювання (image credits: NASA). У нижній частині зображений Чумацький Шлях так як його бачить LISA через випромінювання гравітаційних хвиль від бінарних систем білих карликів у нашій Галактиці.

List of publications

FIRST AUTHOR PAPERS

A multi-messenger study of the Milky Way's stellar disc and bulge with LISA, Gaia and LSST
Korol, V., Rossi, E.M., Barausse, E., 2019
MNRAS 483 5518

Detectability of double white dwarfs in the Local Group with LISA
Korol, V., Koop, O., Rossi, E.M., 2018
ApJL 866 L20

Prospects for detection of detached double white dwarf binaries with Gaia, LSST and LISA
Korol, V., Rossi, E.M., Groot, P.J, Nelemans, G., Toonen, S., Brown, A.G., 2017
MNRAS 470 1894

Bondi accretion in early-type galaxies
Korol, V., Ciotti, L., Pellegrini, S., 2016
MNRAS 460 1188

CO-AUTHORED PAPERS

Where are the double-degenerate progenitors of type Ia supernovae?
Rebassa-Mansergas, A., Toonen, S., **Korol, V.**,Torres, S., 2019
MNRAS 482 3656

The physical properties of AM CVn stars: new insights from Gaia DR2
Ramsey, G., Green, M. J., Marsh, T. R., Kupfer, T., Breedt, E., **Korol**, V., Groot, P. J., Knigge, C., Nelemans, G., Steeghs, D., Woudt., P., Aungwerojwit., A., 2018
A&A 620 A141

LISA verification binaries with updated distances from Gaia Data Release 2
Kupfer, T., **Korol, V.**, Shah, S., Nelemans, G., Marsh, T.R., Ramsay, G., Groot, P.J., Steeghs, D.T.H, Rossi, E.M., 2018
MNRAS 480 302

CONFERENCE PROCEEDINGS

Synergies between Gaia and LISA missions for Galactic multi-messenger studies
Korol, V., Rossi, E. M., 2019
53rd ESLAB symposium: the Gaia universe

Constraining the Milky Way potential with Double White Dwarfs
Korol, V., Rossi, E. M., Barausse, E., 2018
21th European White Dwarf Workshop, arXiv:1810.03938

The difficulty of finding double-degenerate progenitors of type Ia super-novae
Rebassa-Mansergas, A., Toonen, S., **Korol, V.**, Torres, S., 2018
21th European White Dwarf Workshop

Detection of Double White Dwarf Binaries with Gaia, LSST and eLISA
Korol, V., Rossi, E. M., Groot, P.J., 2017
20th European White Dwarf Workshop, ASPC, 509, 529

Curriculum Vitae

I was born 17th of June 1988 in Sumy, Ukraine to Alla Nikolaevna and Yuri Ivanovich Korol. During my childhood I spent many summers with my grandparents, Olga Ivanovna and Ivan Mihailovich, in our countryside house near Sumy. There every night I could enjoy a clear starry sky. I believe that the journey that led me to write this manuscript started there.

I went to school number 15, in Sumy. At school I particularly enjoyed subjects like physics, algebra and geometry, but also chemistry, geography and biology. However, the idea of becoming a scientist never came to my mind. In the 1990s the political and economical state of my country was disastrous. During such difficult times, the concept of studying science, for the sake of science, did not exist among young people. The vast majority of my peers were aiming to become economists, lawyers or engineers. Thus, instead of continuing my studies at the ordinary high school, I decided to study Economics at the *Machine-building Industrial College* with the goal to continue my studies at the Polytechnic University of Sumy. This choice did give me access to advance mathematics, linear algebra and basics of programming. However, I did not finish my studies at college, as in 2005 I moved to Genoa, Italy to join my Mom.

With a new country comes new possibilities. I learnt a new language and a new culture. I continued my high school education at *Liceo scientifico G. L. Bernini*, where I built a background in humanitarian subjects, complementary to the more science focused Ukrainian education program. In particular, with my teacher of natural sciences, Romina Canepa, I made my first visit to an actual observatory. Since then I visited all astronomy related events and observatories in Genoa. Even then, I did not imagine that one day I would become an astronomer. Instead, the constant exposure to art in Italy made me consider becoming an architect. I thought that this would be an ideal way to combine my two biggest interests: art and science. However, when the admission day for the University of Genoa came, I found myself enrolled on the bachelor program in Physics. How this happened is a mystery to my entire family, and even myself.

Since my first day at the Physics faculty my final goal was to study Astronomy. However, because there was not even one astronomy course, I knew that soon I would change my focus. Through a lot of hard work during my bachelor years I built a basis in theoretical physics, which I found I had an aptitude for. For my master I moved to Bologna, where I was finally able to study Astronomy full time. It is very hard to say what courses I did not enjoy during my master. However, the courses that influenced me most were *Galactic Dynamics* by Prof. Luca Ciotti, *Extragalactic Astrophysics* by Prof. Andrea Cimatti, *Gas Dynamics* by Prof. Filippo Fraternali, and *Spectral evolution of galaxies* by Prof. Alberto Buzzoni. I should also highlight

the *Astrophysics Laboratory* course. Firstly, because we were taught how to conduct research projects and analyse data across basically the entire electromagnetic band: radio/millimetre, optical and X-/gamma-rays. Second, and more importantly, because during our lessons on the X-ray part of the course at INAF (Istituto Nazionale di Astrofisica), the *Athena* mission was accepted by ESA. This is where and when, for the first time, I heard about the LISA mission that was planned to be launched in the same time window as *Athena*. This turned out to be pivotal for my future choices, as for me, LISA was (and it still is) the coolest project ever conceived. The best part of my master was my personal (purely theoretical) research project on the accetion of gas onto super massive black holes, which I developed under the supervision of Prof. Luca Ciotti and Prof. Silvia Pellegrini. I am very proud that this work turned into my first scientific publication!

In August 2015 I moved to the Netherlands for my PhD under the supervision of Elena Rossi at Leiden Observatory and co-supervision of Paul Groot at Radbould University, Nijmegen. For my PhD I changed subject from my favourite (huge) super massive black holes to ultra-compact binary systems composed of white dwarfs. The main reason for this change was the fact that I would be able to develop a theoretical model for the tidal interactions between white dwarfs, that would allow me to establish myself as a theoretician. However, the true underlying reasons were the three key words in the project: "gravitational waves" and "LISA". Shortly after I started, there was the first detection of a gravitational wave signal produced by two colliding black holes by the LIGO collaboration. I consider this a very lucky coincidence that helped me to progress through my PhD with interest and excitement from the scientific and non-scientific community alike. But what I consider to be one of my biggest accomplishments is my involvement and contribution to the LISA mission proposal submitted (and now approved) in response to the ESA call for L3 missions. Since then I became a member of the LISA consortium and the exploration of LISA's possibilities became one of my driving interests. During my PhD I have published three first-author papers in high-profile astronomical journals that have broadened the LISA science case. But I also had an active co-author role, and have been involved with more observational papers focused on LISA sources.

During my PhD I have already developed collaborations across the Netherlands, Europe and the US. Together with my LISA colleagues, Natalia Korsakova and Nicola Tamanini, I initiated the creation of the *LISA early career group* meant to facilitate networking between young researchers and promote values of the young generation in the LISA consortium. I thoroughly enjoyed the active and enthusiastic scientific life at Leiden Observatory, to which I contibuted by organising the Compact Objects and High Energy Astrophysics group meetings, and, more recently, by initiating the Gravitational Wave group meetings. As a part of my PhD program at Leiden University I dedicated considerable time to teaching duties. I have been a teaching assistant for both bachelor and master courses and I have also supervised individual students. I have directly supported 6 students through their research projects to date. Two of these projects have also lead to published articles in peer reviewed journals. After getting some experience with job applications, I helped with the organisation of a series of workshops that aimed to guide 3rd- and 4th-year PhD students through the daunting job application process during the first PhD day of the faculty of Science. In addition, I was actively involved in the organisation of fun after work activities within the *Extravaganza* committee.

Finally, I was awarded the prestigious Rubicon grant by Netherlands Organisation for Scientific Research (NWO) to pursue my own research project shared between the Institute of Astronomy in Cambridge and the Institute for Gravitational Wave Astronomy in Birmingham. I am looking forward to starting this new journey in the fall.

Acknowledgements

To ...

... my supervisor, **Elena M. Rossi**, for pushing me to cross my boundaries beyond the limits of my comfort zone, but more importantly for truly being a role model for me, a respected lead female scientist, a caring person, and a modern mother. In difficult moments I always reflect and think about what you have achieved as a mother of two kids, plus four PhD kids.

... my co-supervisor, **Paul J. Groot**, for providing this thesis with an observational twist. Without your contribution I would only be half a multi-messenger astronomer.

... my main collaborators: **Silvia Toonen, Gijs Nelemans, Enrico Barausse, Thomas Kupfer, Anthony A.G.A. Brown** and **Orlin Koop**. Without your important contributions this thesis would have only been half a success.

... my supervisors at the University of Bologna, **Luca Ciotti** and **Silvia Pelligrini**, for your direction and mentorship, you helped to shape me into the scientist that I am today. I truly admire you and I can only aspire to become theoreticians as you are.

... my school and college Physics teachers, **Tatiana Ilyinichna Moskalenko** and **Yuri Dmitrievich Mihailik**, for teaching with passion. I would not be writing this thesis without you reaching me during my school years.

... **all staff members at Leiden Observatory**, and in general Leiden University, where I could work with freedom, in a creative, international and welcoming environment.

... my fellow PhDs at Leiden Observatory: **Alex, Andrej, Andrew, Ann-Sofie, Chris, Christian, Christos, Clément, Dilovan, Eleonora, Eva, Gabi, Gabriella, Fraser, Jit, Kimberly, Maria Cristina, Mike, Nico, Pedro, Santiago, Stella, Tommaso** and many others. You made some difficult days tolerable and many happy days memorable.

... my friends and fellow students at the University of Bologna: **Bobore, Davide, Elena, Giuliano, Mario, Matteo, Raffaella** and **Sara**. Thank you for sharing some of the happiest years of my life and our favourite city, Bologna.

... my friends and fellow students at the University of Genoa: **Alessia, Andrea, Federica, Ilaria** and **Lorenzo**. Thank you for (by now) many years of friendship, for always visiting me and for keeping in touch.

... the **LIGO collaboration** for making the first gravitational wave detection right after I started my PhD. Thank you for transforming this purely theoretical and sometimes frustrating branch of Astrophysics into an new exiting field.

... the **Kavli Summer Programm 2017** organised by **Enrico Ramirez-Ruiz** and **Ilya Mandel** for six, of the most-inspiring, weeks of gravitational wave science, and for providing the platform to meet new friends and (hopefully) future collaborators **Alejandro, Floor, Platon** and **Stefano**. A special thanks to my supervisors of the Kavli programm, **Cole Miller, Ilya Mandel, Melvyn Devies** and **Ross Chirch** for teaching me the basis of stellar dynamics and discussing your creative ideas.

... all the developers of open source Python software for Astronomy and to all contributors of the Stack Overflow forum. You saved me from minutes, hours and (probably) days of irritation, anger and frustration!

Finally, to the closest people to me ...

... my grandparents, **Maria Egorovna** and **Ivan Matveevich Korol** and **Olga Ivanovna** and **Ivan Mihailovich Sergienko**, for bringing me up, nurturing me and helping me grow, for letting me be myself and for always believing in me. A special thanks to my grandpas, who are regularly watching the Discovery channel waiting to see their granddaughter appear there.

... my (little) cousin, **Artur Pavlovich Korol**, for being interested in my work, helping me in editing and translating parts of this thesis and enthusiastically embracing the role of my paranymph.

... **Alessandro Bologna** for often acting as a father to me and for helping me reach my goals and realise my dreams.

... my mom, **Alla Nikolaevna Korol**, for giving me a chance to become who I am now, at great expense and personal sacrifice. Thank you for taking me with you, and then for letting me go. Thank you for giving me freedom and for your unwavering trust in me. There are just too many reasons to thank you, I would need another thesis to be able to write them all.

... my furry four-legged (doggy) sister, **Kimi**, for fulfilling my childhood dream and for giving me fourteen intense years of truly priceless, irreplaceable friendship. Thank you for always giving me your lucky paw before every single exam, evaluation and talk.

And, to conclude, **Luke T. Maud**, my personal manager, editor, therapist, software assistant, chauffeur, flatmate, chef, physician, financial advisor, coach, mechanic, paranymph, and my partner. Thank you for being all these for me.